AD-A271 706

(2)

NAVAL POSTGRADUATE SCHOOL
MONTEREY, CALIFORNIA

THESIS

A THEORY FOR OPTICAL WAVELENGTH CONTROL
IN SHORT PULSE
FREE ELECTRON LASER OSCILLATORS

by

Wade F. Wilkenson

June 1993

Thesis Advisor: William B. Colson

Approved for public release; distribution is unlimited

93-26278

93 1 0 0 1 0

REPORT DOCUMENTATION PAGE

Form Approved
OMB No 0704-0188

Public reporting burden for this collection of information is estimated to average 1 hour per response, including the time for reviewing instructions, searching existing data sources, gathering and maintaining the data needed, and completing and reviewing the collection of information. Send comments regarding this burden estimate or any other aspect of this collection of information, including suggestions for reducing this burden, to Washington Headquarters Services, Directorate for Information Operations and Reports, 1215 Jefferson Davis Highway, Suite 1204, Arlington, VA 22202-4302, and to the Office of Management and Budget, Paperwork Reduction Project (0704-0188), Washington, DC 20503.

1. AGENCY USE ONLY (Leave blank)	2. REPORT DATE	3. REPORT TYPE AND DATES COVERED
	June 1993	Master's Thesis

4. TITLE AND SUBTITLE
A THEORY FOR OPTICAL WAVELENTH CONTROL IN SHORT PULSE FREE ELECTRON LASER OSCILLATORS

5. FUNDING NUMBERS

6. AUTHOR(S)
Wade F. Wilkenson

7. PERFORMING ORGANIZATION NAME(S) AND ADDRESS(ES)
Naval Postgraduate School
Monterey, CA 93943-5000

8. PERFORMING ORGANIZATION REPORT NUMBER

9. SPONSORING / MONITORING AGENCY NAME(S) AND ADDRESS(ES)
Naval Postgraduate School
Monterey, CA 93943-5000

10. SPONSORING / MONITORING AGENCY REPORT NUMBER

11. SUPPLEMENTARY NOTES
The views expressed in this thesis are those of the author and do not reflect the official policy of the Department of Defense or the U.S. Government.

12a. DISTRIBUTION / AVAILABILITY STATEMENT
Approved for public release; distribution unlimited.

12b. DISTRIBUTION CODE

13. ABSTRACT *(Maximum 200 words)*

The future safety of the U.S. Navy warship depends on the development of a directed energy self-defense system to keep pace with the ever-improving technology of anti-ship missiles. Two candidates are reviewed. The free electron laser (FEL) has the most advantages, but a chemical laser proposed by TRW is ready for installation on existing ships. Initial testing of issues related to directed energy use at sea can be conducted with the chemical laser. When the technology of the FEL matures, it can replace the chemical laser to provide the best possible defense in the shortest period of time.

Continuous tunability is a key advantage of the FEL over the conventional laser. But since the output wavelength is dependent on electron energy, it is subject to random fluctuations originating from the beam source. At the Stanford University Superconducting (SCA) Free Electron Laser (FEL) Facility, the effects are minimized through negative feedback by changing the input electron energy proportional to the observed wavelength drift. The process is simulated by modifying a short pulse FEL numerical program to allow the resonant wavelength to vary over many passes. The physical effects behind optical wavelength control are explained. A theory for the preferential nature of the FEL to follow the resonant wavelength from longer to shorter wavelengths is presented. Finally, the response of the FEL to a rapidly changing resonant wavelength is displayed as a transfer function for the system.

14. SUBJECT TERMS	15. NUMBER OF PAGES
FEL, free electron laser, short pulse simulation, optical wavelength control, trapped particle instability, desynchronism, mode competition, low gain FEL, resonance condition, wavelength stabilization, FEL transfer function, directed energy at sea	110
	16. PRICE CODE

17. SECURITY CLASSIFICATION OF REPORT	18. SECURITY CLASSIFICATION OF THIS PAGE	19. SECURITY CLASSIFICATION OF ABSTRACT	20. LIMITATION OF ABSTRACT
UNCLASSIFIED	UNCLASSIFIED	UNCLASSIFIED	UL

Approved for public release; distribution is unlimited.

A THEORY FOR OPTICAL WAVELENGTH CONTROL IN SHORT PULSE FREE ELECTRON LASER OSCILLATORS

by

Wade F. Wilkenson
Lieutenant, United States Navy
B.S., Northwestern University, 1986

Submitted in partial fulfillment of the
requirements for the degree of

MASTER OF SCIENCE IN PHYSICS

from the

NAVAL POSTGRADUATE SCHOOL

June 1992

Author: W.F. Wilkenson
Wade F. Wilkenson

Approved by: William B. Colson
William B. Colson, Thesis Advisor

Robert L. Armstead
Robert L. Armstead, Second Reader

Karlheinz E. Woehler, Chairman,
Department of Physics

ABSTRACT

The future safety of the U.S. Navy warship depends on the development of a directed energy self-defense system to keep pace with the ever-improving technology of anti-ship missiles. Two candidates are reviewed. The free electron laser (FEL) has the most advantages, but a chemical laser proposed by TRW is ready for installation on existing ships. Initial testing of issues related to directed energy use at sea can be conducted with the chemical laser. When the technology of the FEL matures, it can replace the chemical laser to provide the best possible defense in the shortest period of time.

Continuous tunability is a key advantage of the FEL over the conventional laser. But since the output wavelength is dependent on electron energy, it is subject to random fluctuations originating from the beam source. At the Stanford University Superconducting (SCA) Free Electron Laser (FEL) Facility, the effects are minimized through negative feedback by changing the input electron energy proportional to the observed wavelength drift. The process is simulated by modifying a short pulse FEL numerical program to allow the resonant wavelength to vary over many passes. The physical effects behind optical wavelength control are explained. A theory for the preferential nature of the FEL to follow the resonant wavelength from longer to shorter wavelengths is presented. Finally, the response of the FEL to a rapidly changing resonant wavelength is displayed as a transfer function for the system.

UNPUBLISHED 5

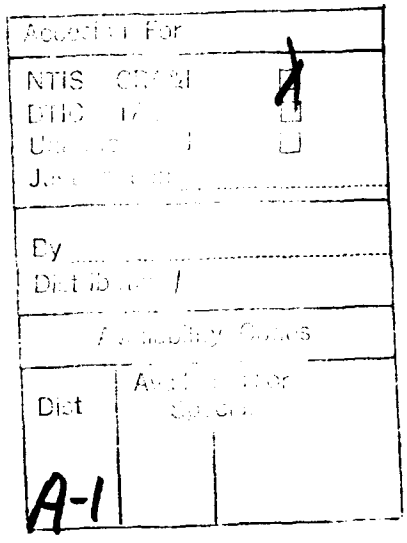

Table of Contents

I. INTRODUCTION 1

II. THE CASE FOR A MODULAR SHIPBOARD HIGH ENERGY LASER SYSTEM 4

A. INTRODUCTION 4

B. BENEFITS OF A LASER SYSTEM 5

C. A MODULAR DESIGN 6

D. EXISTING TECHNOLOGY 9

E. EFFECTIVENESS MODEL 12

F. DISCUSSION 13

G. TRANSITION TO THE FEL 15

III. FREE ELECTRON LASER THEORY 17

A. BASIC FREE ELECTRON LASER PHYSICS 17

B. RESONANCE CONDITION 20

C. ELECTRON DYNAMICS AND THE PENDULUM EQUATION 22

D. THE FEL WAVE EQUATION 25

E. THE LOW GAIN FEL 27

F. GAIN DEGRADATION DUE TO BEAM QUALITY 32

G. MODE COMPETITION 35

H. TRAPPED PARTICLE INSTABILITY 36

I. SHORT PULSE THEORY 39

J. DESYNCHRONISM EFFECTS 43

IV. RESONANT WAVELENGTH MODULATION THEORY 46

A. ELECTRON BEAM ENERGY MODULATION 46

B. COHERENCE AND MODE COMPETITION EFFECTS 46

C. LOW AMPLITUDE, HIGH FREQUENCY MODULATION 49

D. LOW FREQUENCY MODULATION 56

E. HIGH AMPLITUDE MODULATION 57

F. ELECTRON PULSE LENGTH EFFECTS 59

G. MODULATION AT VARIOUS VALUES OF DESYNCHRONISM 64

H. MODULATION AT VARIOUS VALUES OF LOSS 66

I. OPTICAL PHASE PROGRESSION 68

V. WAVELENGTH STABILIZATION THEORY 74

A. INTRODUCTION 74

B. MODULATION TRENDS 75

C. DISCRETE TRANSFER FUNCTION 78

D. LINEAR FEEDBACK THEORY 81

E. CONTINUOUS TRANSFER FUNCTION 83

F. DISCRETE VS. CONTINUOUS TRANSFER FUNCTION COMPARISON 93

VI. CONCLUSIONS 96

LIST OF REFERENCES 99

INITIAL DISTRIBUTION LIST 103

ACKNOWLEDGEMENT

The author gratefully acknowledges the guidance and thorough support of this research provided by Dr. William B. Colson. The author would like to thank Mr. Joe Blau for computer hardware and software assistance provided on many occasions. Much appreciation goes to Andre Marziali of Stanford University, who helped to define the direction of this research, to Dr. Robert Wong for many invaluable conversations, and also to Dr Robert Armstead for suggestions provided as second reader. Finally, the author would like to thank his loving wife, Margaret, and daughter, Rachel, for their patience, continual support, and assistance while writing this thesis.

I. INTRODUCTION

A relativistic pulse of electrons passing through the transverse, periodic magnetic field of an undulator in a free electron laser (FEL) oscillator results in an exchange of energy between the electrons and a co-propagating electromagnetic pulse, which is stored between the mirrors of an optical resonator [1]. When net energy is transferred from the electron pulse, the radiation pulse within the resonator is amplified, and coherent light is produced as the output. A schematic of an FEL oscillator is shown in Figure 1-1.

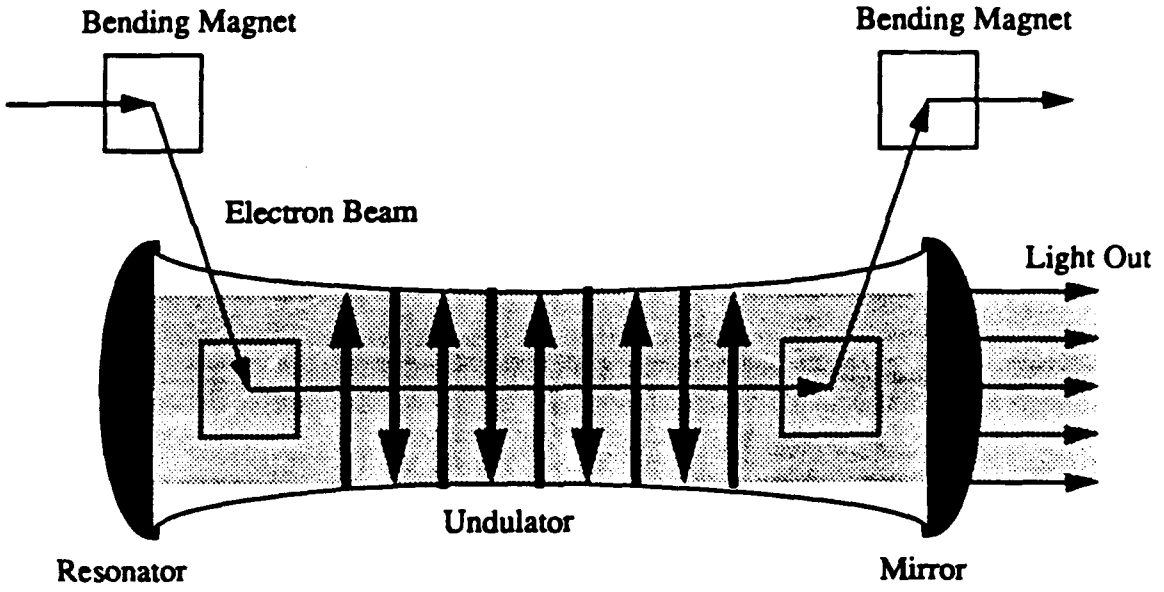

Figure 1-1 Major components of a free electron laser (FEL) oscillator. Bending magnets guide an electron beam through the periodic magnetic field of an undulator. Co-propagating light interacts with the electrons in the optical resonator, resulting in amplification. The amplified coherent light then passes through a partially transmitting mirror at one end of the resonator.

First conceived in 1970 [1], by J.M. Madey at Stanford University, the FEL has since been the subject of considerable research throughout the world. Present FEL development is focused toward the construction of reliable FELs as sources of coherent radiation for medical, industrial, and scientific applications. The FEL shows strong promise for use in military applications as well. The motivation for this research is discussed in Chapter II. The technology of the anti-ship missile has nearly reached the point where conventional kinetic energy defenses are no longer effective. Further, the ever-changing political climate gives rise to the increased possibility that an advanced weapon will fall into the hands of a terrorist aggressor. A directed energy defense system is clearly required for the U.S. Navy warship of the future.

For an efficient energy exchange in an FEL, the forces on the electron beam produced by the undulator and radiation fields must be in a condition of resonance [2]. In a weak undulator, this occurs when the radiation wavelength λ, the electron beam energy γmc^2, and the undulator period λ_o combine to satisfy $\lambda \approx \lambda_o / 2\gamma^2$, where γ is the Lorentz factor, m is the electron mass, and c is the speed of light in vacuum. This resonance condition leads to one of the primary benefits of the FEL design. By changing the electron beam energy, an FEL may be continuously tuned to operate over a wide variety of radiation wavelengths [3].

However, the wavelength of the output light may be subject to objectionable drifts from processes that are not fully understood, and cannot be easily predicted. Fortunately, by measuring the magnitude of drift and providing negative feedback to the electron source, the electron energy can be adjusted to compensate and hold the output wavelength fixed.

Researchers at the Stanford University Superconducting Accelerator (SCA) Free Electron Laser (FEL) Facility have already successfully demonstrated wavelength control in such a manner [4]. But in order to fully optimize the system, detailed information about the process of wavelength control is required. The goal of of this thesis is to describe the basic physics involved.

An overview of FEL theory required for the development of optical wavelength control discussion is presented in Chapter III. In Chapter IV, an FEL simulation describing the evolution of a multimode short optical pulse is modified to allow the resonant wavelength to oscillate over many passes. The result is identical to changing the electron beam energy in the Stanford SCA/FEL experiment. An asymmetry is observed in the ability of the short optical pulse to follow resonant wavelength. The FEL preferentially follows shifts from longer to shorter optical wavelengths with higher corresponding optical power. A theory is presented to explain this phenomenon.

When the resonant wavelength of the FEL is varied slowly over many passes, the short optical wavelength easily follows the transition. The ability of the optical pulse to follow resonant wavelength over shorter time scales is of concern to researchers at the Stanford SCA/FEL facility, because it can allow faster feedback to the electron energy source in order to optimize the wavelength control system. In Chapter V, simulations are used to determine the nature of the change in resonant wavelength over increasing frequency scales. Two different methods are used to determine the response of the FEL to a rapidly changing resonant wavelength. The results are displayed as a transfer functions for the system.

II. THE CASE FOR A MODULAR SHIPBOARD HIGH ENERGY LASER SYSTEM

A. INTRODUCTION

For many decades, the proliferation of weapons to Third World countries was subsidized in an attempt to gain alliance with one of the two major superpowers. Seeking political advantage, missiles and other arms were freely sold to allies of each power. There was also little or no concern that nations like France and China routinely traded advanced weapons for monetary gain. With the collapse of the Soviet Union came drastic changes in the views toward Third World arms proliferation. No longer would the preoccupation with East-West problems overshadow regional Third World differences. Today, the US Navy faces the responsibility of peace-keeping in a world strewn with regional instabilities. Further, since many of these regions of strife tend to overlap, there is the continued threat of additional arms proliferation. An attack on the US Navy by a Third World nation, although likely to be much smaller than a Soviet multi-regiment and coordinated air attack, could still inflict significant damage upon individual ships. This became apparent in 1982 during the British war over the Falkland Islands, when Argentina used Exocet missiles supplied by France to sink a state-of-the-art frigate. Five years later, during the Iran-Iraq War, the Iraqis nearly sank the *USS Stark* with the same system [5].

It is also likely that an engagement on US naval forces by a Third World country will be driven by political rather than military goals. Any type of attack profile might be used, since positive identification may not be required for actual targeting. In effect, the damage or destruction of a single ship may be sufficient for

embarrassment of the US [6]. The threat is real. A modern naval warship must be defensible against all types of missiles if it is not to become obsolete. However, the advent and proliferation of long-range, high-speed, low-flying, and jinking anti-ship missiles makes this a formidable task [7]. One solution could be the installation of a Modular Shipboard High Energy Laser (MODSHEL) for anti-ship missile self-defense.

B. BENEFITS OF A LASER SYSTEM

The technology to support anti-ship missiles seems to have outreached the means to defend a ship against them by kinetic means. Missiles produced today are supersonic sea skimmers that are highly maneuverable and utilize the most advanced stealth and electronic warfare. In fact, a missile which is proposed for active service in 1995 as a replacement for the Exocet is the Aerospatiale/MBB Supersonic Anti-Ship missile (ANS) [8]. The ANS is intended to be a long range (≈180 km), sea-skimming missile capable of about $10g$ terminal jinking at speeds greater than 2 Mach, where $g = 9.8\ m/s^2$ acceleration. A convenient rule of thumb given by Dr. Robert S. Bradford, Jr., Manager of the Directed Energy Systems Department at TRW, in a briefing presented to students at the Naval Postgraduate School is that defensive missiles require at least three times the maneuverability of the offensive missile they are targeting [9]. Here it is easy to see that a 30g maneuverable missile would be required to defend a ship against the ANS, and then, the same technology required to develop that missile could readily be used to create another anti-ship missile. The advantage is always going to be with the attacker unless a system is designed which is insensitive to maneuverability advances. A laser is just such a system. At speed of light delivery, it is not necessary to calculate the trajectory of the missile. If the missile can be detected, that line-of-sight information is all that is required to kill it.

Instead of firing physical projectiles or missiles, the MODSHEL would irradiate the incoming missile with electromagnetic energy, collimating and focusing the beam as much as possible to increase the effective lethality of the system. Since the laser fires massless energy rather than bulky, cumbersome missiles, the size of the "magazine" that can be accommodated in the same amount of space on a ship could be greatly enhanced [10]. This is often termed magazine depth and is only limited by the amount of fuel that can be carried in the case of a chemical laser, or of the amount of electrical power available if using a Free Electron Laser (FEL).

A laser system for anti-ship missile defense could potentially have a very high effective lethality. Since current missile defense doctrine usually includes the firing of two missiles to engage a single incoming missile, the cost per engagement could be lowered substantially. By design, a laser system would be relatively insusceptible to electro-optical and electronic warfare countermeasures. It is feasible that the system would also readily integrate with existing acquisition and fire control systems. In fact, the beam director optics available to the system would also be available for use in enhanced line-of-sight surveillance. [9]

C. A MODULAR DESIGN

Modularity in ship design is the utilization of modules or standardized units which can be assembled or put into place to perform a specific purpose or function [11]. Modularity is not a new concept. In fact, examples of it are prevalent ranging from prefabricated homes to the cartridges used in the NINTENDO video game. Modular weapon design would necessarily require the use of standard foundations, dimensions and common interfaces for cooling water, power supplies and data cables [11]. Obviously, this would increase the complexity of design of any new system. However, the potential benefits can greatly outweigh the initial inconvenience. For

example, the modular design permits construction of the ship independent of the weapon system delivery time. Further, the outfitting time of the system on the ship can be reduced with a subsequent increase in quality assurance since the module can be pretested under workshop conditions. It would also be convenient to remove the system for upgrade, overhaul or even replacement by new systems as technology allows.

A concept proposed by the TRW Space and Technology Group called for a shipboard Deuterium Fluoride (DF) High Energy Laser (HEL) which could be installed in the B module of a MK-41 Vertical Launch System (VLS). In response to a request by the Deputy Chief of Naval Operations, Naval Warfare (Op-07) in July 1990, the Center for Naval Analysis began to evaluate this concept. The results of this evaluation are published in a secret report, CNA Research Memorandum 91-81 [6]. From the unclassified portions of this report many interesting facts can be obtained. The CNA analysis found that current technologies could easily allow installation of a shipboard modular HEL on existing ship platforms for the use of initial testing of critical issues concerning laser shipboard operation. The HEL would replace existing weapon systems on any of three ship classes: (1) replace the NATO Seasparrow in DD-963 destroyers, (2) replace the forward Phalanx Close-in Weapon System (CIWS) and VLS module in DDG-51 destroyers, (3) replace one 5-in/54 caliber gun mount in CG-52 cruisers.

The major components of MODSHEL would include: (1) reactant storage for the chemicals pressurized in cryogenic tanks; (2) the laser device; (3) laser cooling systems including turbine water pumps and connected equipment; (4) an extensive exhaust management system designed to prevent hazard to humans and also to prevent beam attenuation caused by small amounts of deuterium fluoride entering the laser beam path; (5) a beam transfer system which would be designed to automatically

maintain alignment in spite of ship vibration and flexing at sea; and finally, (6) a safe replenishment system in which chemicals could be replaced at sea via helicopter or delivery ship. The CNA study narrowed the list of feasibility criteria to three critical issues. First, if the system is to be successful, it must fit in the desired area. The capability of other remaining weapon systems and the overall operation of the ship must not be degraded. And most importantly, the ship's architectural safety margins, i.e. stability and maneuverability, must not be diminished.

Another study conducted by CNA in August 1990 [12] further investigated the shipboard design issues associated with the installation of the MODSHEL in the configurations listed above. Since current technology would call for a chemical high energy laser, it was noted that the ultimate design and feasibility criteria would be the safe handling of the toxic effluents (hydrogen fluoride and deuterium fluoride) so as not to put topside personnel at hazard. Further, the laser system would be a great deal larger than any system it would replace, requiring reconfiguration and design of those systems nearby which would not be replaced. Also under consideration was the increased peak electrical demand which the MODSHEL would place on the engineering system. Finally, the study evaluated the ultimate cost of emplacement of the MODSHEL.

Obviously, there are more issues which must be considered when designing a laser weapon system for use at sea. For example, the structure of a ship is subject to significant motion due to wave action [12]. The MODSHEL must be capable of withstanding these vibrations and stresses without loss of effectiveness. There is also the likelihood of frequent inundation by sea water in heavy seas--a hazard to any intricate weapon system but an effect which must be designed for. Using all these criteria, the CNA studies concluded that the installation of MODSHEL in the above configurations could be realized with little effect on stability of the ships involved.

The peak electrical demand would not impose a significant burden to the existing engineering plants, and the overall performance of the ships would not be degraded.

The CNA study did find one operational disadvantage worthy of note. Installation of the MODSHEL would require replacement of a large number of long range offensive and defensive missiles by a system which is designed to be defensive with a range on the order of a few kilometers. However, it was concluded that a truly modular system could be designed such that only a few would be produced, installed pierside or by tender to specific ships expecting missions requiring additional defensive capability, i.e. single-ship power projection or escort operations.

D. EXISTING TECHNOLOGY

The Department of Defense has been interested in the possibility of directed energy weapons (DEWs) since the mid-1970s. The first effort directed toward this goal was the gas dynamic CO_2 laser developed under a program called the Airborne Laser Laboratory (ALL) [13]. A 400 kilowatt version was installed on a KC-135 aircraft, along with a high technology beam director. After the ability to shoot down missiles in flight was demonstrated [14], the program was considered to be a success. However, due to schedule slippages, complexity, cost and susceptibility to countermeasures, it was considered unsuccessful relative to competitive air-to-air kinetic defense methods. At the time, it was thought that missiles could be hardened easier than it would be to make a more powerful CO_2 laser. The main results from ALL were the need for a type of DEW which could readily scale to higher power levels and utilize a less complex fire control system. [13]

The Navy's first interest in DEWs stemmed from the possibility that the threat of missiles launched against a battlegroup of ships could be minimized by shipboard laser weapons. These DEWs would be less complex due to the relatively stable sea

environment compared to the rigorous demands imposed on an airborne beam director [13]. Moreover, chemical DF lasers had reached a level of technology which could allow scaling to significantly higher power levels than the CO_2 versions. Under these assumptions, the Navy funded several programs resulting in the MIRACL (Mid-Infrared Advanced Chemical Laser) device developed by TRW, and the Sea Lite Beam Director (SLBD) developed by Hughes Aircraft Co. [13] The MIRACL device is a continuous-wave DF chemical laser which can produce power in excess of 1 MW [15]. Operation is based on a combustion-driven process in which atomic fluorine, F, reacts with molecular deuterium, D_2, to produce deuterium fluoride in any of several excited states with an inherent population inversion of states. Subsequent atomic transitions between the various energy levels produce output wavelengths between 3.7-4.0 micrometers. The MIRACL/SLBD combination was subject to a series of tests at White Sands, New Mexico. First, a stationary missile booster was destroyed. Then, a drone was shot down while in flight. Finally, in a key demonstration, the MIRACL/SLBD device was used to destroy a Mach 2.2 Vandal anti-air missile in flight [9]. Unfortunately, by the time the MIRACL Laser was operational, shipborne missiles and guns proved to be a more attractive choice to the Navy due to their lower cost and more mature technology.

The ever-increasing sophistication and wide proliferation of anti-ship missiles has since brought the MIRACL/SLBD program back into the spot-light. Improved miniaturization and increased performance design have made it possible to create a self-contained, modular HEL package suitable to replace the weapon systems discussed earlier. An advanced concept recently proposed by TRW and considered by the Navy is the High Energy Laser Weapon System (HELWEPS) designed primarily for anti-ship missile defense [9]. This presents the latest HEL weapon system candidate for use on Navy warships, and it seems to correspond nicely to the type of system

previously considered by the Center for Naval Analysis. HELWEPS produces power equivalent to the MIRACL/SLBD system. As shown in Figure 2-1, it is packaged to be weight and size equivalent to a 5-in/54 caliber gun. The chemical used, deuterium fluoride, allows an output wavelength of 3.8 micrometers. It is designed to have a pointing accuracy of 5 microradians from an aperture of 1.5 meters. The estimated cost of the system is 70 million dollars. TRW estimates the magazine depth to be at least 50 shots with a response time of 1 second and a corresponding cost per kill of 10 thousand dollars. Further, the extrapolated kill range is purported to be 2-5 kilometers under nearly all weather conditions with an effective lethality of 96 percent.

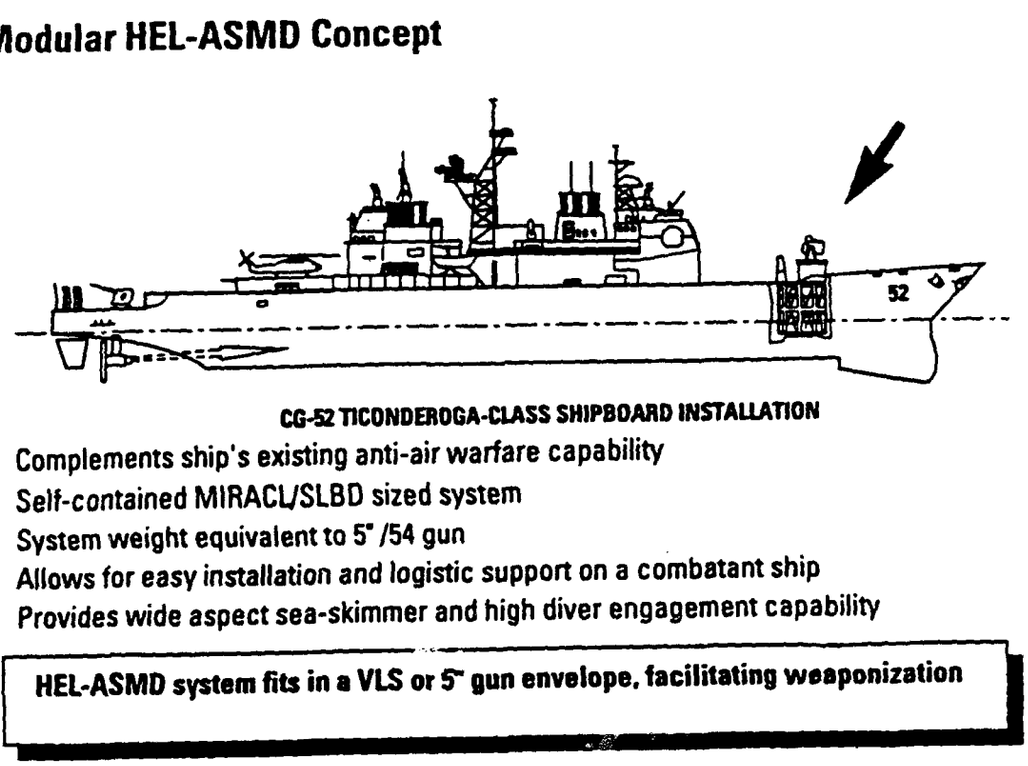

Figure 2-1. The High Energy Laser Weapon System (HELWEPS) concept for Anti-Ship Missile Defense (AMSD). Proposed by TRW, this system can be the prototype for evaluation of "speed of light" defense at sea. [9]

TRW also suggests the addition of a "green", 550 nanometer wavelength, low-power laser within the module designed to provide auxiliary missions [9]. These missions could include submarine periscope or mine detection and secure, line-of-sight communications. The optics for this system would be small, and thus could be placed in several locations throughout the ship.

E. EFFECTIVENESS MODEL

The numbers proposed by TRW are relatively easy to verify using standard laser propagation equations. Since the laser aperture, $D = 1.5$ meters, and radiation wavelength, $\lambda = 3.8$ micrometers, are given, the spot size, A, at an incoming missile at range $R = 5$ kilometers can be calculated by: [15]

$$A = \frac{\pi R^2 \lambda^2}{D^2} = 5.0 \text{ cm}^2 \quad . \tag{2.1}$$

Fluence, F (in J/cm^2) , is the common measure of "hardness" of a missile, since it describes the amount of energy absorbed by the skin which destroys it. Fluence is calculated by: [15]

$$F = \frac{P \Delta t}{A} \quad , \tag{2.2}$$

where P is the actual power received at the missile, and Δt is the dwell time that is required to incapacitate it. A moderately hardened missile might require a fluence of 10 kJ/cm^2. TRW states a total response time of 1 second, the dwell time must be a fraction of this, accounting for acquisition time and slew rate of the beam director. If a 0.1 second dwell time is assumed, the total power required at the missile, calculated from equation (2), is $P = 500$ kilowatts. The extinction coefficient due to aerosols in the atmosphere is $\alpha \approx 5 \times 10^{-2}$/km, and through $e^{-\alpha z}$ describes the removal of power at $\lambda = 3.8$ micrometers wavelength over a distance z. Therefore, the power required to

leave the ship at 5 km range to destroy the missile, P_o, is given by:

$$P_o = \frac{P}{e^{-\alpha z}} = \frac{(500.0)}{e^{-(0.05)(5.0)}} \approx 640 \text{ kW} \quad . \tag{2.3}$$

Since TRW reports a design power approximately equivalent to the MIRACL/SLBD device, or about 1 MW, the required output power of 640 kW is well within capability. If the missile is assumed to be traveling at about Mach 3 or 1000 m/s, the time for the laser beam radiation to reach the missile at 5 km is:

$$T_{light} = \frac{(5000.0 \text{ m})}{(3.0 \times 10^8 \text{ m/s})} = 16.7 \text{ μs} \quad . \tag{2.4}$$

Meanwhile, the distance the missile can travel during this time is:

$$D_{missile} = (1000 \text{ m/s})(16.7 \text{ μs}) = 16.7 \text{ mm} \quad . \tag{2.5}$$

So the missile moves very little during this time--even at Mach 3, which effectively eliminates the threat of a terminal jinking maneuver by the missile. All in all, these calculations attest to the viability and effectiveness of the system.

F. DISCUSSION

The world political outlook is murky at best. The collapse of the Soviet Union has indeed brought an end to the Cold War, but regional instabilities remain. Correspondingly, the United States has assumed the role of the single superpower in the New World Order. However, recent military spending cuts have brought a decrease in force structure, emphasizing the significance of the modern naval warship as an extremely valuable asset. Anti-ship missile technology has progressed to the point where survival by ordinary kinetic means is at question. Projectile and missile self-defense systems face critical problems. They have limited speed, range, lethality, and they require calculation of ballistics and trajectories to hit the target. Missile

systems requiring update information from the ship are highly susceptible to electronic warfare countermeasures. Terminal jinking or maneuvering of the attacking missile can also serve to reduce the effectiveness of these systems. In effect, the time has come for the consideration of a weapon system capable of delivering destructive energy at the speed of light.

A modular shipboard high energy laser like the HELWEPS, proposed by TRW, seems well suited to the task of providing effective close-in defense in conjunction with weapon systems already in use. Fire-control systems are compatible, and the advanced optics of the beam director can actually enhance target detection, identification, and kill assessment for all shipboard systems. The power requirements, weight and size of the system readily allow emplacement on existing ships, thus making HELWEPS a logical first choice as an initial testbed for laser related at-sea reliability, effectiveness, and system integration. Even though the system is designed only for short range defense, it can be particularly effective for a single ship involved in forward-deployed patrol operations. The modularity of the HELWEPS provides the means for changing a ship's configuration to meet the requirements for such a mission.

Still, there are many crucial areas of concern when considering successful long term use of the HELWEPS. The depth of magazine of the laser depends upon the amount of chemical fuel which can be stored onboard. Further, the toxic effluents of combustion must be safely routed away from topside personnel. Also, since the laser depends upon quantum transitions from excited molecular states, the output wavelength is tied to the properties of the chemicals used and thus is not readily controllable. Anti-ship missiles designed with shielding against the small range of wavelengths available to the laser can eliminate the effectiveness of the system.

G. TRANSITION TO THE FEL

The FEL is not subject to the same limitations that plague the chemical laser. First, the radiation source is a relativistic beam of electrons which emit coherently when subject to the accelerating forces of a periodically changing magnetic field, so the depth of magazine is only limited by the amount of electrical power available from the ship's turbine generators. Additionally, the FEL is completely and relatively easily tunable to a wide range of wavelengths by various means, as will be discussed in Chapter III. This provides the FEL with an advantage over the chemical laser--being able to select the operating output wavelength for optimum atmospheric transmission and missile lethality. FELs have already successfully operated in the infrared and ultraviolet spectral ranges with wide tunability [16]. Another advantage of the FEL is the potentially high overall or wallplug efficiency of the system. The wallplug efficiency of a FEL is defined as the ratio of average emission power output to the electric power input, and is dependent upon energy extraction efficiency of the undulator and design technology of the electron beam source. Through extensive beam recovery and well-designed beam transport, it is likely that a wallplug efficiency as high as 40% can be achieved [16].

However, the technology to support FEL use at sea is not complete. FELs have indeed demonstrated high peak powers on the order of a gigawatt, but high average power in the megawatt range is yet to be shown. The primary problem is not FEL design, but rather the production of an electron beam with sufficient quality to support the required conditions for FEL operation [17]. Moreover, the size of a typical FEL system is usually quite large disproportionally due to the immense size of the electron beam source. Technological improvements in electron beam quality, compactness of design and high average power are on the forefront of FEL research, but will take time. Meanwhile, the U.S. Navy can benefit from implementation of a program

involving a system like HELWEPS. Then, shipboard use issues (i.e., operation and accuracy in the hostile sea environment) can be addressed and solved at the same time FEL design issues are solved. The technology already exists to install and use the HELWEPS. The HELWEPS seems to be the logical stepping stone to the future of warfare at sea--"speed of light" defense.

III. FREE ELECTRON LASER THEORY

A. BASIC FREE ELECTRON LASER PHYSICS

Emission from a FEL oscillator is the result of an interaction among three basic elements: a relativistic electron beam supplied by an accelerator, a co-propagating electromagnetic wave, and finally, a spatially periodic magnetic field produced by an "undulator" [2,18]. The interaction space is the length of the undulator, $L = N\lambda_o$, where N is the number of magnetic undulator periods, and λ_o is the corresponding wavelength. As the electrons in the beam travel through the undulator, forces from the magnetic field cause their trajectories to "wiggle" in the transverse direction. Accelerating from side to side, the electrons can spontaneously emit light in a forward cone along the beam path. Spherical mirrors placed on the beam axis beyond the ends of the undulator allow a fraction of the radiation to collect and resonate. Stimulated emission then arises through coupling between the growing optical field and subsequent electrons entering the undulator; coherent radiation is output [3].

Before reaching the undulator, the electrons are accelerated to the relativistic energy, γmc^2, where m is the electron rest mass and c is the velocity of light. The Lorentz factor is $\gamma = 1/\sqrt{1-\beta^2}$, where $\beta = \upsilon/c$, and υ is the electron velocity magnitude.

The properties of the undulator fully determine the properties of the resulting optical radiation. Magnetic polarization of an undulator defines the trajectory for electron deflection and is accomplished either by permanent magnets or electromagnets. Linear or helical polarization is possible with the emitted radiation having linear or circular polarization respectively [19]. The strength of the undulator

characterizes the magnitude of deflection of the electrons, and is defined as the "undulator parameter",

$$K = \frac{e\bar{B}\lambda_o}{2\pi mc^2} \quad , \tag{3.1}$$

where $\bar{B}$ is the root-mean-square (rms) magnetic field strength. Electrons are subject to constant acceleration in a helically polarized undulator, so $\bar{B} = B$, the peak magnetic field strength. On the other hand, the sinusoidal electron path in the linearly polarized undulator requires the correction $\bar{B} = B/\sqrt{2}$, due to non-constant acceleration.

Quantum mechanical processes are involved in the FEL interaction. For example, as an electron emits a photon, it is subject to a small recoil. But the loss of energy is so small that many such events are required to effectively change the interaction characteristics of a single electron. Since the electron density of the injected beam is usually very large, recoil effects are negligible. Similarly, the interaction volume of the FEL contains a large number of photons, so statistical fluctuations in the optical wave can be ignored. The net result is that classical electromagnetic theory correctly predicts the interaction between the electrons, light and undulator. [3]

The classical approach to the FEL interaction is summarized in Figure 3-1 [20]. At the top, electrons enter the undulator and begin to oscillate in the presence of transverse magnetic fields. Radiation is emitted in a forward cone, and this optical wave propagates with the electrons. The middle portion of Figure 3-1 expands a single period within the undulator. Electron motion is in the y–z plane. If oscillation in the negative y direction occurs while the magnetic field from the optical wave is in the negative x direction, (shown at the bottom), an opposing Lorentz force will cause the electron to lose energy to the optical wave. This qualitative description illustrates

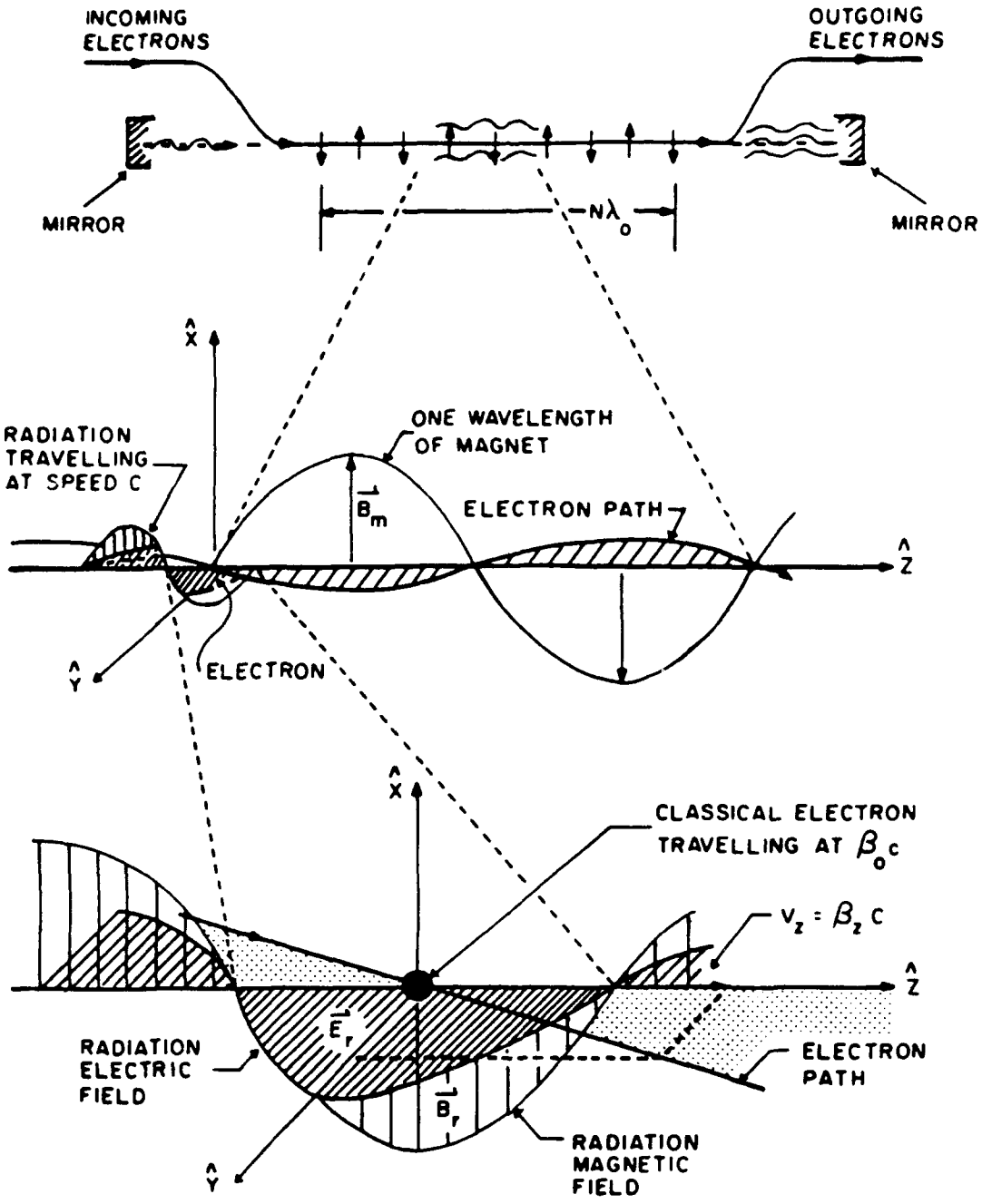

Figure 3-1. Fundamental physics of the FEL interaction.

the importance of the relative phase of each electron to the optical wave. Electrons in the wrong phase will gain energy from the radiation field, countering amplification. With electrons spread equally over all phases of the optical field, some gain energy and some lose energy. Overall, the electrons form into bunches on the scale of the optical wavelength. Over many optical wavelengths, the bunches of electrons produce coherent radiation at the end of the undulator [3].

B. RESONANCE CONDITION

In an FEL, the electrons travel through the undulator as free particles in vacuum, rather than being attached to atoms as in a conventional lasing medium. As a result, the wavelength of light emitted is not confined to a particular atomic energy level transition. Instead, the electrons emit radiation by shifting energies in a continuum [18]. Further, the electrons are relativistic, so the magnetic periods of the undulator appear Lorentz contracted to the effective wavelength $\lambda'_o = \lambda_o/\gamma$ in the beam frame. The radiation field passing over the electrons during the interaction appears Doppler shifted to the longer effective wavelength $\lambda' = (1 + \beta_z)\gamma\lambda = 2\gamma\lambda$, where λ is the optical wavelength in the lab frame [2]. Efficient energy exchange between the electrons and the optical wave is contingent upon a condition of resonance. Resonance occurs between the undulator and the radiation field forces in the beam frame when $\lambda' = \lambda_o'$. When converted to the undulator frame, the FEL resonance condition becomes,

$$\lambda = \frac{\lambda_o(1 + K^2)}{2\gamma^2} \quad . \tag{3.2}$$

As shown in Figure 3-2, the electromagnetic wave travels the distance of one undulator period plus one optical period in the time that the electron moves one undulator period, causing the radiation to continuously slip ahead of the electron beam [21].

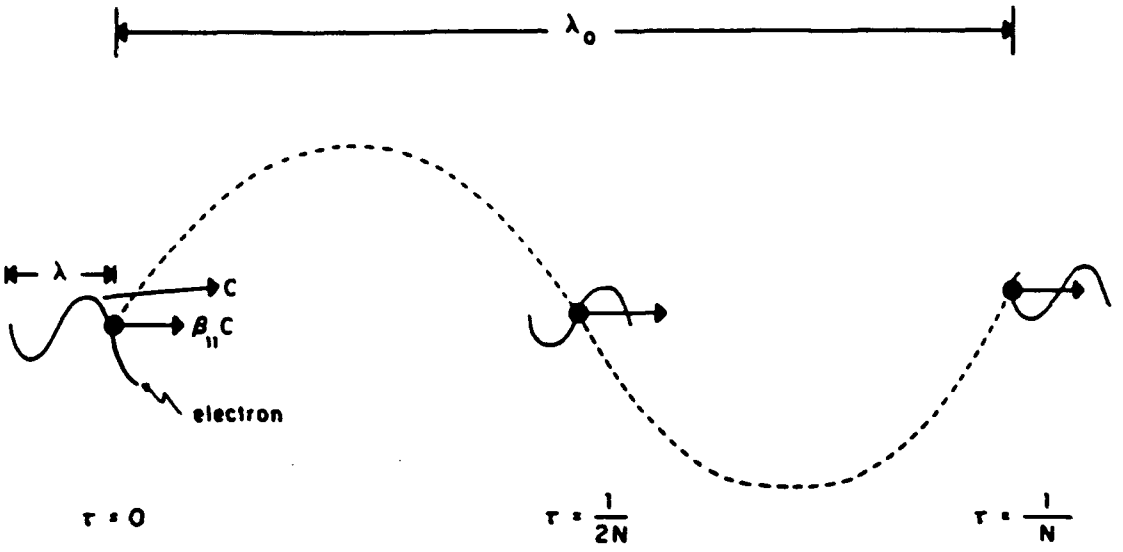

Figure 3-2. A resonant electron slips back one optical wavelength λ as it traverses one undulator period λ_o.

Two of the most attractive features of the FEL are inherent in Equation (3.2). First, the FEL is continuously tunable; shifts in optical wavelength are accomplished by changing the electron energy γmc^2, the magnetic field strength B, or the undulator wavelength λ_o. Researchers have demonstrated this property by varying all three of these variables [22]. Second, the FEL has great design flexibility.

Particularly useful is the ability to change the properties of the undulator along its length to compensate for electrons falling out of resonance as they give up energy to the optical wave. By tapering the undulator, i.e., decreasing λ_o, resonance is extended over more of the undulator length, thereby improving the efficiency of the interaction [23].

C. ELECTRON DYNAMICS AND THE PENDULUM EQUATION

The FEL electron dynamics are described by solving the Lorentz force equations of motion for a single electron in the presence of the undulator magnetic and optical wave electromagnetic fields [23]. A helical design is assumed for the undulator; the corresponding magnetic field will be circularly polarized which, in ideal form, is given by

$$\vec{B} = (B_x, B_y, B_z) = B(\cos(k_o z), \sin(k_o z), 0) \ , \tag{3.3}$$

where $k_o = 2\pi/\lambda_o$ is the undulator wavenumber, and z is the direction along the undulator axis. For the optical field within the undulator, a circularly-polarized plane wave is assumed of the form

$$\vec{E}_R = E(\cos\Psi, -\sin\Psi, 0) \ , \quad \vec{B}_R = E(\sin\Psi, \cos\Psi, 0) \ , \tag{3.4}$$

where E is the optical field magnitude. Here, $\Psi = kz - \omega t + \phi$, where $k = 2\pi/\lambda$ is the optical wave number, ω is the radial frequency, and ϕ is the optical phase angle.

The Lorentz force equations governing the electron motion are written:

$$\frac{d(\gamma\vec{\beta})}{dt} = \frac{-e}{mc}[\vec{E}_R + \vec{\beta} \times (\vec{B} + \vec{B}_R)] \ , \tag{3.5a}$$

$$\frac{d\gamma}{dt} = \frac{-e}{mc}\vec{\beta} \cdot \vec{E}_R \ , \tag{3.5b}$$

$$\gamma^{-2} = 1 - \vec{\beta} \cdot \vec{\beta} \ , \tag{3.5c}$$

where $\vec{\beta}c$ defines the electron velocity vector. Only four of the five Equations (3.5) are required for complete solution since there are only four unknowns, namely $x(t)$, $y(t)$, $z(t)$, and $\gamma(t)$. To solve, the undulator magnetic field (3.3) and the optical wave electromagnetic fields (3.4) are substituted into the Lorentz force equations (3.5). When the transverse and longitudinal components are separated, the equations become:

$$\frac{d(\gamma\vec{\beta}_\perp)}{dt} = \frac{-e}{mc}[E(1-\beta_z)(\cos\Psi, -\sin\Psi, 0) + \beta_z B(-\sin k_o z, \cos k_o z, 0)] \ , \qquad (3.6a)$$

$$\frac{d(\gamma\beta_x)}{dt} = \frac{-e}{mc}[E(\beta_x\cos\Psi - \beta_y\sin\Psi) + B(\beta_x\sin k_o z - \beta_y\cos k_o z)] \ , \qquad (3.6b)$$

$$\frac{d\gamma}{dt} = \frac{-e}{mc}E[\beta_x\cos\Psi - \beta_y\sin\Psi] \ , \qquad (3.6c)$$

where $\vec{\beta}_\perp = (\beta_x, \beta_y, 0)$. The electrons traveling in the z direction are subject to a transverse force from the optical electromagnetic fields. For relativistic electrons, this is proportional to $E(1-\beta_z) \approx E/2\gamma^2$, which is negligible; the transverse force on the electrons is primarily determined by the undulator magnetic field. Applying this approximation to (3.6a) yields

$$\frac{d(\gamma\vec{\beta}_\perp)}{dt} \approx \frac{-e}{mc}\beta_z B(-\sin k_o z, \cos k_o z, 0) \ , \qquad (3.7)$$

which can then be integrated, resulting in the transverse electron velocity,

$$\vec{\beta}_\perp = \frac{-K}{\gamma}(\cos k_o z, \sin k_o z, 0) \ . \qquad (3.8)$$

Integration constants are zero assuming perfect electron injection. Insert (3.8) into (3.6c) to get the time rate of change of the electron energy,

$$\dot{\gamma} = \frac{-e}{mc}(\vec{\beta}_\perp \cdot \vec{E}_R) = \frac{eKE}{\gamma mc}\cos(\zeta + \phi) \ , \qquad (3.9)$$

where $\dot{\gamma} = d\gamma/dt$, and $\zeta = (k + k_o)z - \omega t$ is a dimensionless variable determining the relative phase of an electron with respect to the optical and undulator fields. Note for time $t = 0$, the initial value of phase is $\zeta_o = (k + k_o)z_o$, but since $k \gg k_o$, the initial phase is approximately given by $\zeta_o = kz_o$. Thus ζ determines the approximate electron z position relative to a single optical wavelength. Using the relations $\gamma^{-2} = 1 - \beta_z^2 - \beta_\perp^2$ and $\beta_\perp = K/\gamma$, the second derivative of the electron phase with respect to time becomes

$$\ddot{\zeta} = \frac{2\omega_o eKE}{\gamma^2 mc}\cos(\zeta + \phi) \ , \tag{3.10}$$

where $\omega_o = \omega(1 + K^2)/2\gamma^2$. To make (3.10) dimensionless, define $\tau = ct/L$. Then an electron makes a single pass down the undulator in dimensionless time $\tau = 0 \rightarrow 1$. Further, the dimensionless optical field is defined $a = |a|e^{i\phi}$, with magnitude $|a| = 4\pi NeKLE/\gamma^2 mc^2$. Inserting these into (3.10) shows that an electron in the FEL evolves according to the simple pendulum equation [24]

$$\overset{oo}{\zeta} = \overset{o}{v} = |a|\cos(\zeta + \phi) \ , \tag{3.11}$$

where $v(\tau) = \overset{o}{\zeta} = L[\,(k + k_o)\beta_z - k\,]$ is the dimensionless phase velocity of the electron, $(\overset{o}{..}) = d(\,..\,)/d\tau$, and $(\overset{oo}{..}) = d^2(\,..\,)/d\tau^2$. If an electron has $v = 0$, then it is at resonance with the optical wave and Equation (3.2) applies. A decrease in electron energy corresponds to a decrease in phase velocity. The lost energy is given to the optical wave. Inspection of (3.11) reveals that maximum energy loss occurs when the phase $(\zeta + \phi)$ is near π. For all the electrons within the beam, each is identified uniquely by its initial phase ζ_o and phase velocity v_o, and will individually evolve according to (3.11). The beam preferentially loses energy to the optical wave when bunching of electrons occurs near $(\zeta + \phi) \approx \pi$, thus amplifying the optical field.

D. THE FEL WAVE EQUATION

The evolution of the complex optical wave is governed by Maxwell's wave equation driven by the transverse electron beam current $\vec{J}_\perp$ [25]:

$$\left[\nabla^2 - \frac{1}{c^2}\frac{\partial^2}{\partial t^2}\right]\vec{A} = -\frac{4\pi}{c}\vec{J}_\perp \ . \tag{3.12}$$

where $\vec{A}$ is the vector potential for a circularly polarized plane wave, and is given by

$$\vec{A} = \frac{E_R(t)}{k}(\sin\Psi, \cos\Psi, 0) \ . \tag{3.13}$$

Equation (3.13) assumes no x or y dependence, so $\nabla^2 \rightarrow \partial^2/\partial z^2$ in the wave equation (3.12). For optical coherence to be maintained, the optical field amplitude and phase must vary slowly during the interaction [23]. This requires $\dot{E} \ll \omega E$ and $\dot{\phi} \ll \omega\phi$; so after inserting the vector field (3.13), all second derivatives and terms with two derivatives can be dropped from the wave equation (3.12) obtaining

$$2\left[\frac{\partial E_R}{\partial z} + \frac{1}{c}\frac{\partial E_R}{\partial t}\right]\hat{\epsilon}_1 - 2E_R\left[\frac{\partial \phi}{\partial z} + \frac{1}{c}\frac{\partial \phi}{\partial t}\right]\hat{\epsilon}_2 = -\frac{4\pi}{c}\vec{J}_\perp \ , \tag{3.14}$$

where the two orthogonal unit vectors have been defined as $\hat{\epsilon}_1 = (\cos\Psi, -\sin\Psi, 0)$ and $\hat{\epsilon}_2 = (\sin\Psi, \cos\Psi, 0)$. As the electron moves in the z direction, the undulator magnetic field forces the transverse electron velocity to rotate as the optical field passes over it [19]. Maxwell's wave equation (3.14) is projected onto $\hat{\epsilon}_1$ and $\hat{\epsilon}_2$, forming two first order scalar equations:

$$\left[\frac{\partial E_R}{\partial z} + \frac{1}{c}\frac{\partial E_R}{\partial t}\right] = -\frac{2\pi}{c}(\vec{J}_\perp \cdot \hat{\epsilon}_1) \tag{3.15a}$$

$$E_R\left[\frac{\partial \phi}{\partial z} + \frac{1}{c}\frac{\partial \phi}{\partial t}\right] = \frac{2\pi}{c}(\vec{J}_\perp \cdot \hat{\epsilon}_2) \ . \tag{3.15b}$$

The contribution to the transverse beam current from a single electron is $\vec{J}_{\perp i} = -ec\vec{\beta}_{\perp}\delta^{(3)}(\vec{x} - \vec{r}_i)$, where $\vec{r}_i$ is the position vector of the ith electron, and $\delta^{(3)}(\ ..\ )$ is the three dimensional Dirac delta function [25]. Using $\vec{\beta}_{\perp}$ from (3.8), and summing over all single particle currents, the total transverse electron beam current becomes

$$\vec{J}_{\perp} = \sum_i \frac{ecK}{\gamma}(\cos k_o z\ ,\ \sin k_o z\ ,\ 0)\delta^{(3)}(\vec{x} - \vec{r}_i)\ . \tag{3.16}$$

Projecting (3.16) onto the the unit vectors $\hat{\epsilon}_1$ and $\hat{\epsilon}_2$ results in the following two equations:

$$\vec{J}_{\perp} \cdot \hat{\epsilon}_1 = \sum_i \frac{ecK}{\gamma}\cos(\zeta + \phi)\delta^{(3)}(\vec{x} - \vec{r}_i)\ , \tag{3.17a}$$

and

$$\vec{J}_{\perp} \cdot \hat{\epsilon}_2 = \sum_i \frac{ecK}{\gamma}\sin(\zeta + \phi)\delta^{(3)}(\vec{x} - \vec{r}_i)\ . \tag{3.17b}$$

The wave equations (3.15) evolve slowly over several optical wavelengths. The beam current must be averaged over a small volume element a few optical wavelengths long. Since an electron pulse from the accelerator is much greater in scale than this volume element, the electron density ρ can be assumed fixed [23]. Applying this, and substituting (3.17), the new wave equations are

$$\frac{1}{c}\frac{\partial E_R}{\partial t} = -\frac{2\pi eK\rho}{\gamma} < \cos(\zeta + \phi) >\ , \tag{3.18a}$$

and

$$E_R\frac{1}{c}\frac{\partial \phi}{\partial t} = \frac{2\pi eK\rho}{\gamma} < \sin(\zeta + \phi) >\ , \tag{3.18b}$$

where $\rho< .. >$ represents the electron beam average over sampled electrons weighted by the electron density ρ. Equations (3.18) are expressed in final form by inserting the

dimensionless beam current $j = 8N\ (e\pi KL)^2\rho/\gamma^3 mc^2$:

$$\dot{|a|} = -j\langle \cos(\zeta + \phi) \rangle \ , \ \dot{\phi} = \frac{j}{|a|}\langle \sin(\zeta + \phi) \rangle \ , \tag{3.19}$$

or simply,

$$\dot{a} = -j\langle e^{-i\zeta} \rangle \ , \tag{3.20}$$

where $a = |a|e^{i\phi}$ is the complex dimensionless optical field, with $|a| = 4\pi NeKLE/\gamma^2 mc^2$. Inspection of (3.19) reveals that bunching of electrons around the phase $(\zeta + \phi) \approx \pi$ will lead to amplification of the optical wave, while bunching of electrons near $(\zeta + \phi) \approx \pi/2$ will drive the optical phase. Increasing the electron beam current density j will produce increased gain and optical phase evolution; the resulting increase in the optical field magnitude, however, will act to reduce the effect on phase evolution.

E. THE LOW GAIN FEL

The simple pendulum equation (3.11) and the optical wave equation (3.20) combine to form the Maxwell-Lorentz theory for the FEL [2]. The evolution of each electron traveling through the undulator follows (3.11), while the evolution of optical phase and amplitude is determined by (3.20). The dimensionless current j provides coupling between the two equations because it determines the response of the optical wave to bunching in the electron beam. In effect, a particular gain regime is identified by the magnitude of j [26]. The Maxwell-Lorentz theory is generally valid for both weak ($|a| \ll \pi$) and strong ($|a| \gg \pi$) optical fields, and also for high ($j \gg 1$) or low ($j \leq 1$) gain conditions [19].

Gain in the low-gain FEL oscillator develops from coherent electron bunching on the scale of the optical wavelength [26]. The bunched electron beam radiates

coherently and amplifies the radiation within the undulator. Each pass provides only a fractional increase in optical power at the resonant wavelength, but the resonator collects each increase such that substantial power is available after several hundreds of passes. When the electron beam enters the undulator, maximum coupling will occur between the electrons and optical wave if the initial dimensionless phase velocity for each electron is at resonance, $v_o = 0$. But since the electrons will likely enter with a random distribution in phase ζ, just as many electrons will gain energy as will lose energy from the optical wave; net gain is not achieved [3]. Useful gain is produced when the incoming electrons have velocities slightly above resonance. Then, more electrons tend to lose energy to the optical wave and the cancellation process is disrupted.

An important tool for understanding the operation of the FEL is obtained by displaying the evolution of electrons in (ζ, v) phase-space according to Equations (3.11) and (3.20). The initial phase ζ_o and initial phase velocity v_o uniquely determine the evolution of each electron, and therefore constrain it to follow a particular orbit or path in phase-space [27]. In the low gain FEL, the path followed by an electron is the same as that of the simple pendulum, and is represented analytically by

$$v^2 = v_o^2 - 2|a|[\sin(\zeta + \phi) - \sin(\zeta_o)] \quad . \tag{3.21}$$

Relating an electron in phase space to a mechanical pendulum, unstable fixed points located at positions $(-3\pi/2, 0)$ and $(\pi/2, 0)$ correspond to the pendulum sitting at the top of its arc. Electrons with phase-space positions near these points evolve slowly. The point $(\pi/2, 0)$ is a stable fixed point corresponding to the pendulum resting at the bottom of its arc. An electron with an open orbit is similar to a pendulum of sufficient energy such that it continuously rotates in a single direction about its pivot. An electron with a closed orbit is like a pendulum with small amplitude oscillation about

the stable fixed point. The curve in phase space which separates the open and closed paths of an electron is called the "separatrix" and is given by

$$v_s^2 = 2|a|[\,1 - \sin(\zeta_s + \phi)\,] \quad . \tag{3.22}$$

By inspection of (3.22), the separatrix has peak-to-peak height $4|a|^{1/2}$ and its horizontal position depends on the optical phase ϕ.

The particles in an electron beam are assumed to be spread uniformly over all wavelengths of the co-propagating radiation. Since the electron evolution in (ζ, ϕ) phase-space is periodic over each optical wavelength, the FEL interaction can be effectively modeled by tracking only the sample electrons distributed over one optical wavelength [27].

The phase-space evolution in Figure 3-3 is obtained by solving the Maxwell-Lorentz theory numerically for a low gain FEL with $j = 1.5$. The undulator consists of $N = 120$ magnetic periods, and the electrons enter at time $\tau = 0$ with initial phase velocity $v_o = 2.6$. The electrons are given a uniform distribution in initial phase $\zeta_o = -\pi/2 \rightarrow 3\pi/2$, each interacting in the initial optical field of magnitude $a_o = 5$. At first, the electrons are displayed as light grey. As they evolve in τ they become darker until they are finally black at $\tau = 1$. The separatrix is drawn for ease in identification of open and closed electron orbits in the pendulum phase-space. Electrons initially positioned such that they lose energy to the optical wave will drop in phase velocity v, and fall behind the average flow of electrons. Others will gain energy, moving ahead of the flow [3]. The net result is spatial bunching of electrons, which is observed near phase $\zeta = \pi$ at $\tau = 1$. As discussed earlier, bunching near this phase provides overall gain to the optical wave.

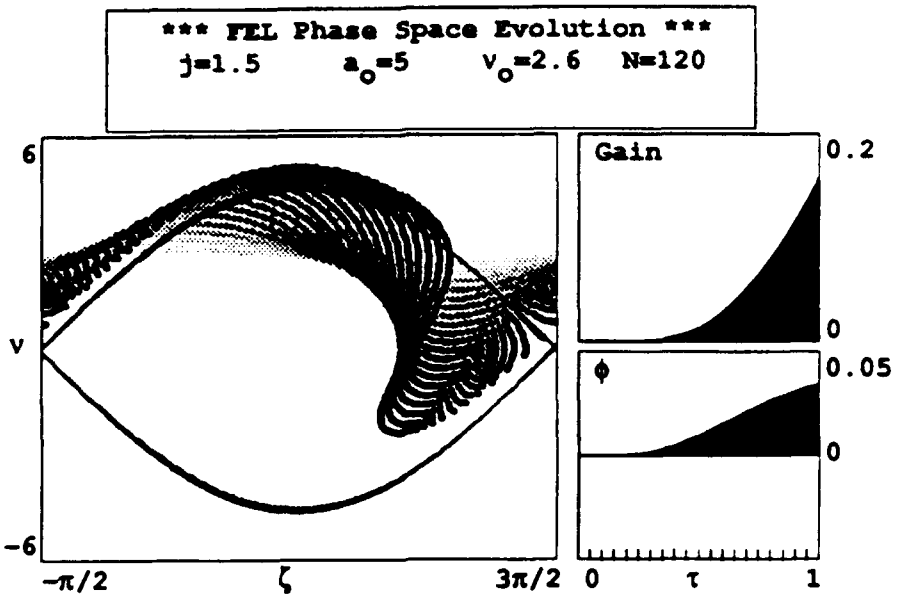

Figure 3-3. Electron (ζ, ϕ) phase-space for a low gain FEL. Electron bunching near phase $\zeta = \pi$ results in gain and optical phase growth.

Gain is defined as the fractional increase in optical power per unit time [28],

$$G(\tau) = \frac{[a(\tau)^2 - a^2{}_o]}{a^2{}_o} \quad , \tag{3.23}$$

and is shown at the upper-right in Figure 3-3, along with the progression in optical field phase ϕ at the lower-right. At the beginning, there is no gain or phase shift, since the electron beam is uniformly distributed. As bunching develops with increasing time τ, the gain increases with a corresponding shift in optical phase.

An analytical expression for low current FEL gain $G(\tau)$ in weak optical fields is obtained using energy conservation [3]. The pendulum equation (3.11) is expanded in orders of the initial optical field a_o. Electrons in the beam are assumed uniformly distributed in phase ζ_o and each have the same initial phase velocity ν_o.

Near resonance, the expression for the electron phase velocity is $v(\tau) \approx L[k_o - k(1 + K^2)/2\gamma^2]$. A change in the electron energy $\Delta\gamma mc^2$ results in a corresponding change in electron phase velocity $\Delta v \approx 4\pi N \Delta\gamma/\gamma$. For gain to occur, net energy must be transferred from the beam of electrons to the optical wave. The average energy lost by an electron is $\gamma mc^2(\langle v\rangle - v_o)/4\pi N$, and the corresponding contribution to optical gain is $G = 2j(v_o - \langle v\rangle)/a_o^2$. The phase velocity average $\langle v\rangle$ is found from the pendulum equation expansion, resulting in the small signal gain equation [3]

$$G(\tau) = j\left[\frac{2 - 2\cos(v_o\tau) - v_o\tau\sin(v_o\tau)}{v_o^3}\right] . \tag{3.24}$$

For weak optical fields and low gain, the gain per unit current, G/j, depends only on the initial electron phase velocity of the electrons [3].

Figure 3.4 is a plot showing the final gain spectrum for a low gain FEL at time $\tau = 1$ versus the initial phase velocity v_o. The spectrum is anti-symmetric about $v_o = 0$ with a peak gain of $G = 0.17j$ at $v_o \approx 2.6$. Exactly at resonance, $v_o = 0$, there is no gain. Negative values of phase velocity near resonance correspond to net absorption of optical power by the electrons. Electrons with positive phase velocities near resonance amplify the optical wave.

Phase velocities far off resonance, $|v_o| \gg \pi$, result in many small amplitude gain oscillations shifting between amplification and absorption; FEL coupling is effectively diminished. The range of good FEL coupling is roughly $|v_o| \leq \pi$, and since positive gain takes place for about half these values, the FEL natural gain bandwidth is $\Delta v_o \approx \pi$. Using the relation $\Delta v_o \approx 4\pi N \Delta\gamma/\gamma$ the FEL natural gain bandwidth becomes

$$\left|\frac{\Delta\gamma}{\gamma}\right| \approx \frac{1}{2N} . \tag{3.25}$$

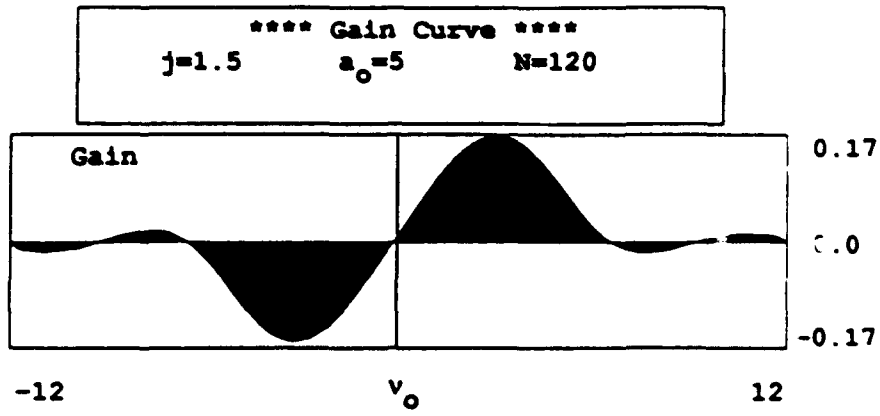

Figure 3-4. Weak-field gain spectrum $G(\nu_o)$ for low current FEL.

Changes in electron beam energy and resonance act to shift the gain spectrum along the phase velocity axis. When subject to a change in electron beam energy $\Delta\gamma = \gamma\Delta\nu_o/4\pi N$, the ν_o-axis becomes a function of the resonant energy $\gamma = (\lambda_o(1 + K^2)/2\lambda)^{1/2}$. When subject to a change in optical wavelength $\Delta\lambda = \lambda\Delta\nu_o/2\pi N$, the ν_o-axis is centered about the resonant wavelength $\lambda = \lambda_o(1+K^2)/2\gamma^2$. [3]

F. GAIN DEGRADATION DUE TO BEAM QUALITY

The results of the previous section assumed perfect electron beam injection into the undulator. The electrons were distributed uniformly throughout the optical wavelength each with the same initial energy, ν_o. Realistically, an ideal beam cannot be achieved. An experimenter wishing to optimize an FEL's performance must consider a design trade-off between the current density and the quality of the electron beam [29]. For a fixed wavelength λ, the dimensionless current $j = 8N(e\pi KL)^2\rho/\gamma^3 mc^2 \propto IN^3\lambda^{1/2}$ must be maximized. Increasing the beam current $I \propto \rho$ reduces beam quality. With increased N the gain spectrum bandwidth is reduced, and the FEL becomes more sensitive to electron beam quality. Poor beam

quality reduces coherent electron bunching and therefore degrades the performance of the FEL [3].

The effects of electron beam quality are evaluated analytically by combining the pendulum equation (3.11) and the optical wave equation (3.20) to form the FEL integral equation [29,30]

$$a(\tau) = a_0 + \frac{ij}{2}\int_0^{\tau} d\tau' \, \tau' F(\tau') e^{-iv_0\tau'} a(\tau - \tau') \quad , \tag{3.26}$$

where

$$F(\tau') = \int dq \, f(q) e^{-iq\tau'} \quad , \tag{3.27}$$

is the characteristic function of $f(q)$. The function $f(q)$ is a normalized distribution of initial electron phase velocities $v_i = v_0 + q$ about v_0 such that $\int dq \, f(q) = 1$ [3]. By using (3.26), the electrons within the undulator are no longer labeled by their initial phase-space coordinates. Initial electron phases are indistinguishable, but an average over the distribution of initial electron phase velocities is retained. As an example, two electrons having different z velocities, as a result of an initial energy difference $\Delta\gamma mc^2$, will be separated in phase by $4\pi N \Delta\gamma/\gamma$ at the end of the undulator [30]. Therefore, in a Gaussian distribution of phase velocities, the standard deviation measuring the energy spread takes the form $\sigma_G = 4\pi N \Delta\gamma/\gamma$, and the distribution function becomes

$$f_G(q) = \frac{e^{-q^2/2\sigma_G^2}}{\sqrt{2\pi}\,\sigma_G} \quad . \tag{3.28}$$

Evaluating (3.27) with (3.28), the corresponding characteristic function for a Gaussian distribution in phase velocities is

$$F_G(\tau) = e^{-\sigma_G^2\tau^2/2} \quad . \tag{3.29}$$

When the beam quality is perfect, $\sigma_G = 0$, so $F(\tau) = 1$. During the FEL interaction, the optical field in (3.26) begins to grow exponentially through feedback from the integrand $a(\tau-\tau')$. However, with an imperfect electron beam $|F(\tau')|$ decays rapidly in time, deteriorating the optical feedback mechanism by reducing the ability of the FEL to bunch electrons. [3]

Figure 3-5 is a surface plot showing the degradation of the gain spectrum $G(\nu_o)$ with increasing electron energy spread σ_G. The current density is $j = 3$. For a mono-energetic beam, $\sigma_G = 0$, the gain spectrum is antisymmetric with a peak at phase velocity $\nu_o = 2.6$ as in Figure 3-4. As the beam energy spread is increased, the maximum available gain decreases while the phase velocity for peak gain increases away from resonance [30]. Further, the overall gain spectrum becomes broader in ν_o around the maximum so that optical growth is allowed over a greater range of initial phase velocities. Even though maximum gain is reduced, the gain bandwidth increases.

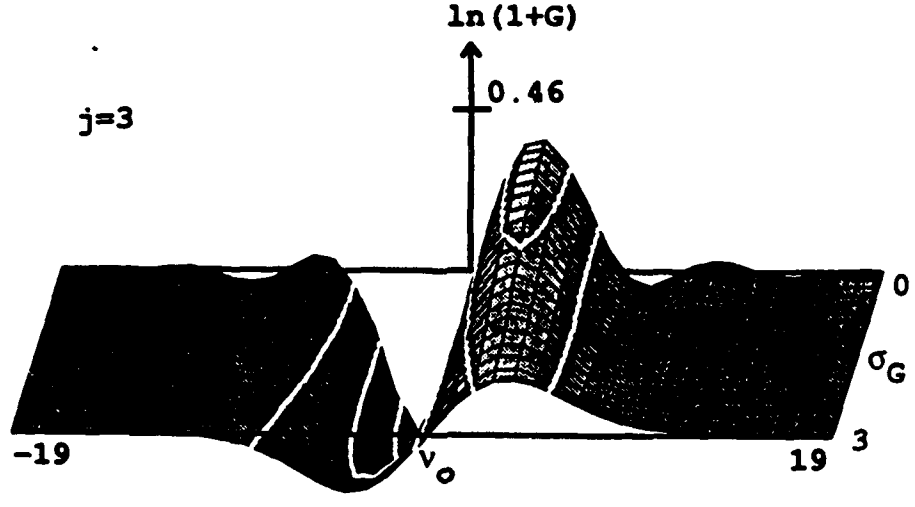

Figure 3-5. Weak-field gain $G(\nu_o)$ spectrum for low current FEL with increasing electron energy spread σ_G.

G. MODE COMPETITION

In the low gain FEL oscillator, the optical wavefront is generated by spontaneous emission from electrons in the beam. Mode competition serves to narrow the frequency spectrum and to increase the coherence length of the light wave. The weak-field gain equation (3.24) solves the evolution of gain in a single optical mode over a single pass. For low gain, separate modes in an FEL oscillator evolve independently. The coherence development of output frequency and optical power are analyzed using (3.24) to follow the various modes simultaneously over many passes n. In the longitudinal z dimension, modes are scaled by the gain bandwidth (3.25) and normalized to the electron-optical slippage distance $N\lambda$ [3]. The slippage distance refers to the length a resonant electron lags behind a point in the optical wave at the end of the undulator $\tau = 1$. The lag arises because of the difference between the electron speed $c\beta_z$ and the speed of light c, resulting in $(c - \beta_z)(L/c) \approx N\lambda$, where L/c is the interaction time [3]. In the transverse direction, modes are scaled by the approximate radius of the optical beam, $(L\lambda/\pi)^{1/2}$. Since the electrons in the beam are relativistic, intermode spacing is $\Delta\nu(k) \approx \gamma^{-2}$, which is small compared to the size of the mode. The FEL is therefore considered to have a continuum of modes across the gain spectrum bandwidth $\Delta\nu \approx \pi$ [3].

Each longitudinal mode is identified by a particular phase velocity $\nu(k) = L[(k + k_o)\beta_z - k]$ corresponding to an output wavelength $\lambda = 2\pi/k$. During each pass n, optical power in each mode is increased by the spontaneous emission spectrum $s(\nu) \propto (\sin(\nu/2)/(\nu/2))^2$ and the FEL gain spectrum $G(\nu)$. Optical losses at the resonator mirrors are described by Q so that $e^{-n/Q}$ determines the total optical loss per mode over n passes. Typically, Q ranges from $10 \rightarrow 100$ depending on resonator cavity design. The incremental change in optical power $P_n = |a(n)|^2$ on the nth pass is given by

$$\Delta P_n(\nu) = s(\nu) + P_n(\nu)[G(\nu) - 1/Q] \ , \tag{3.30}$$

where $P_n(\nu)$ is the optical power in mode $\nu(k)$ [3].

The plots in Figure 3-6 show how the normalized optical spectrum $P(\nu,n)/P_{max}$ evolves from spontaneous emission into a narrow spectrum over n=1000 and n = 8000 passes. For both plots, the peak gain is $G = 0.17j = 26\%$ for $j = 1.5$. The spontaneous emission spectrum is shown at the bottom. The gain spectrum $G(\nu)$ is plotted above showing the level of loss $Q = 30$, depicted as a horizontal line. The final optical spectrum $P_f(\nu)$ is given at the top of the plots after a designated number of passes n. After $n = 1000$ passes, the final spectrum is centered around the phase velocity $\nu = 2.6$ for peak weak-field gain, but retains a wide distribution of optical modes. After $n = 8000$ passes, however, the spectrum has narrowed significantly, and the coherence length of the peak mode is about four times greater than the modes surrounding it.

H. TRAPPED PARTICLE INSTABILITY

When the incremental change in optical power, $\Delta P_n(\nu)$, from Equation (3.30) is positive, the optical field will grow until saturation is reached. At the onset of strong-field saturation, more electrons in the beam have closed phase-space orbits, so the FEL efficiency is increased. However, electrons also begin to interact with each other in the presence of the growing optical field. Overbunching of electrons occurs as some electrons overtake, or fall behind others in the electron beam, and gain is diminished [3].

The trapped particle instability is observed in strong optical fields near the onset of saturation. Some electrons in the beam become trapped in deep potential wells in phase-space, created by the combined optical and undulator field forces [31]. Electrons in harmonic orbits oscillate at the synchrotron frequency, $\nu_s = |a|^{1/2}$. The

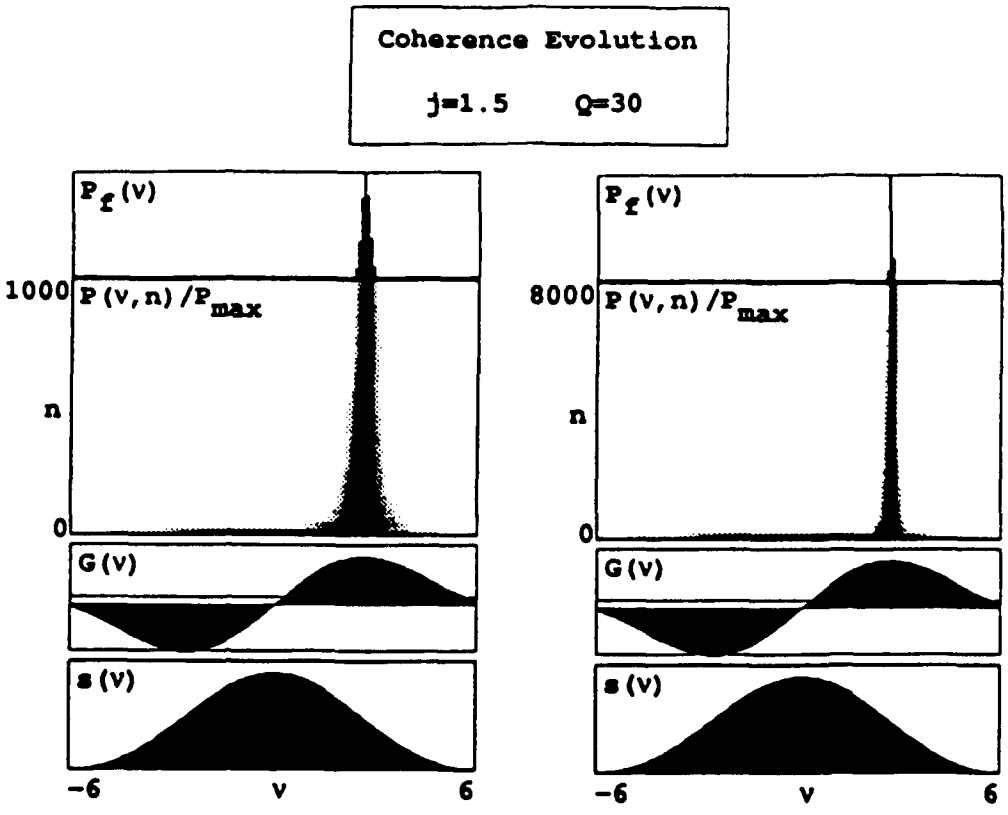

Figure 3-6. Coherence development resulting from mode competition in low-gain FEL for $n = 1000$ and $n = 8000$ passes.

oscillation of these electrons couples to the optical wavefront, mixing the synchrotron frequency with that of the optical carrier wave. This results in the nucleation and growth of optical sidebands. Any coherence established by mode competition in weak-fields is subsequently modified or destroyed [3].

Electrons trapped in the potential wells in the presence of an optical field strength $|a| = 4\pi^2 \approx 40$ will make one complete synchrotron oscillation as they traverse the undulator. The corresponding peak-to-peak separatrix height is $4|a|^{1/2} \approx 25$. Figure 3-7 shows a phase-space evolution for 100 sample electrons subject to a field strength of $a_0 = 40$. The dimensionless beam current is $j = 1.5$, and there are $N = 120$

magnetic periods in the undulator. Electrons in the beam are equally distributed in phase ζ, each with an initial energy $\nu_o = 7$.

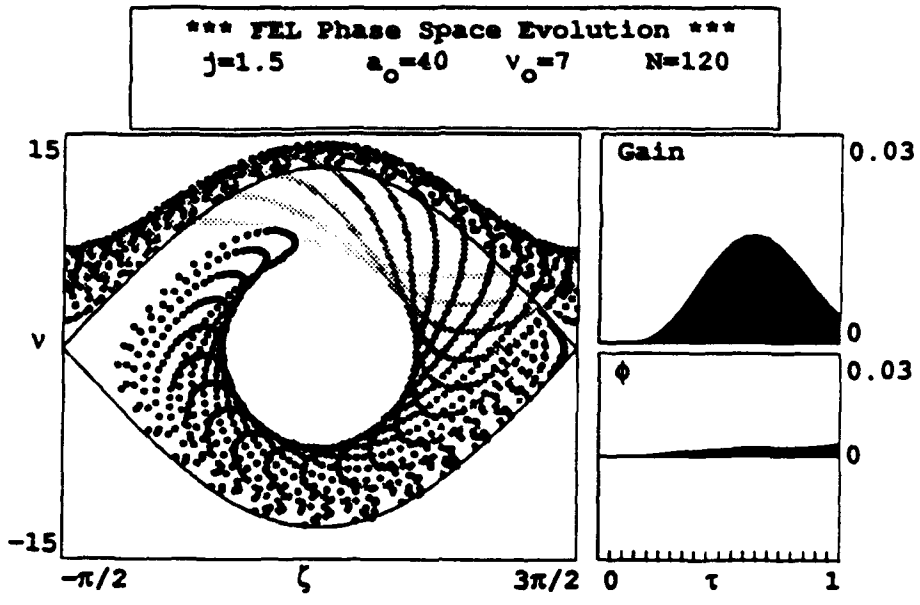

Figure 3-7. Phase space evolution of 100 sample electrons demonstrating trapped particle instability.

The stable fixed phase-space point $\zeta = \pi/2$ corresponds to the bottom of the trapped particle potential well. Electrons near this initial phase execute one complete synchrotron oscillation during the time $\tau = 0 \rightarrow 1$. The plots at the right show the evolution of gain $G(\tau)$ and optical phase ϕ. As bunching develops, the gain and optical phase grow. Overbunching causes optical saturation and a decrease in the gain to nearly zero.

I. SHORT PULSE THEORY

Radio-frequency (RF) accelerators are typical electron beam sources for the FEL. In an RF accelerator, a series of waveguides are used to slow a traveling microwave field to just above the velocity of a beam of injected electrons. As the electrons and the electromagnetic field move down the guide, electrons tend to bunch near the crest of each microwave wavelength, riding much like a surfer on an ocean wave. Since only a fraction of the electrons in the RF cycle survive full acceleration, the output from an RF accelerator is a series of short picosecond long pulses [31].

When the electron pulses enter the FEL oscillator, short optical pulses generated from spontaneous emission begin to bounce between the resonator mirrors [3]. The pulses in the optical wavefront are separated by a distance S, the length between the mirrors. Each rebounding optical pulse arrives at the beginning of the undulator at time $\tau = 0$, and the interval between consecutive pulses is $2S/c$. The timing of the FEL has to be such that a light pulse and an electron pulse enter coincident with each other for successful optical wave amplification. Short pulse effects dominate the FEL interaction when the length of the electron pulse approaches the slippage distance $N\lambda$ [3].

In short pulse theory, all longitudinal distances are normalized to the slippage distance such that $Z/N\lambda \rightarrow z$. The Maxwell-Lorentz theory is extended to track multiple sites along the complex wave envelope. So $a \rightarrow a(z)$ and is equivalent to an extension to longitudinal wavenumbers $a \rightarrow a(k)$. With this extension, the pendulum equation (3.11) and the optical wave equation (3.20) are modified to become

$$\overset{\circ\circ}{\zeta}_{z-\tau} = |a_z| \cos(\zeta_{z-\tau} + \phi_z) \ , \tag{3.31}$$

and

$$\overset{\circ}{a}_z = -j_{z-\tau} < e^{-i\zeta_{z-\tau}} > \quad . \tag{3.32}$$

The subscript z corresponds to a particular optical site along the undulator, while $z-\tau$ denotes an electron site that has slipped back to the optical site in time τ because of the lower velocity of the electron pulse. As electrons travel along the undulator they slip back over a range of sites in the optical wave envelope. In doing this, the electrons actually pass information from one optical site to another [3]. The extension for the electron current density is $j \rightarrow j(z) = 8N(\pi eKL)^2\rho(z)/\gamma^3 mc^2$, where $\rho(z)$ is the actual electron density at the particular longitudinal site z. The electron pulse shape is taken to be parabolic in form:

$$j = \begin{cases} j_o(1 - 2z^2/\sigma_z^2) & \text{for } j(z) > 0 \\ 0 & \text{for } j(z) = 0 \quad , \end{cases} \tag{3.33}$$

where j_o is the peak beam current, and $\sigma_z = l_e/N\lambda$ normalizes the actual electron pulse length l_e [3].

Desynchronism, d, refers to the normalized displacement between the electron and optical pulses at the beginning of each pass $\tau = 0$. Exact synchronism occurs for $d = 0$, where the electron pulse time interval is $2S/c$. Desynchronism is adjusted by moving the resonator mirrors a short distance, increasing or decreasing the optical path length $2S$ [3].

The optical wavefront is tracked over a number of longitudinal sites N_W. The particular value of N_w depends on the amount of detail desired in the optical spectrum. The calculational window width is measured in slippage distances $N\lambda$, and is given by $W = N_W\Delta z$, where Δz is the dimensionless spacing between longitudinal sites. Optical modes $\nu(k)$ are followed according to

$$\nu_l = \nu_o - \left[\frac{\pi}{W} \right] (2l - N_W) \quad \text{for } l = 0, 1, 2, \ldots, N_W - 1 \ . \tag{3.34}$$

where l is an integer [3]. The spacing between optical modes is $\Delta\nu = 2\pi/W$. Longitudinal site spacing Δz is made proportional to the integration time step $\Delta\tau$, so the electron pulse slips back a known distance each time step. At each site z, the simulation follows a number of electrons in phase and phase velocity as they interact with the optical field. For short pulses, a calculational window width W slightly larger than the extent of the light and electron pulses provides adequate detail to characterize FEL performance [3]. Figure 3-8 demonstrates short-pulse behavior for a low gain FEL.

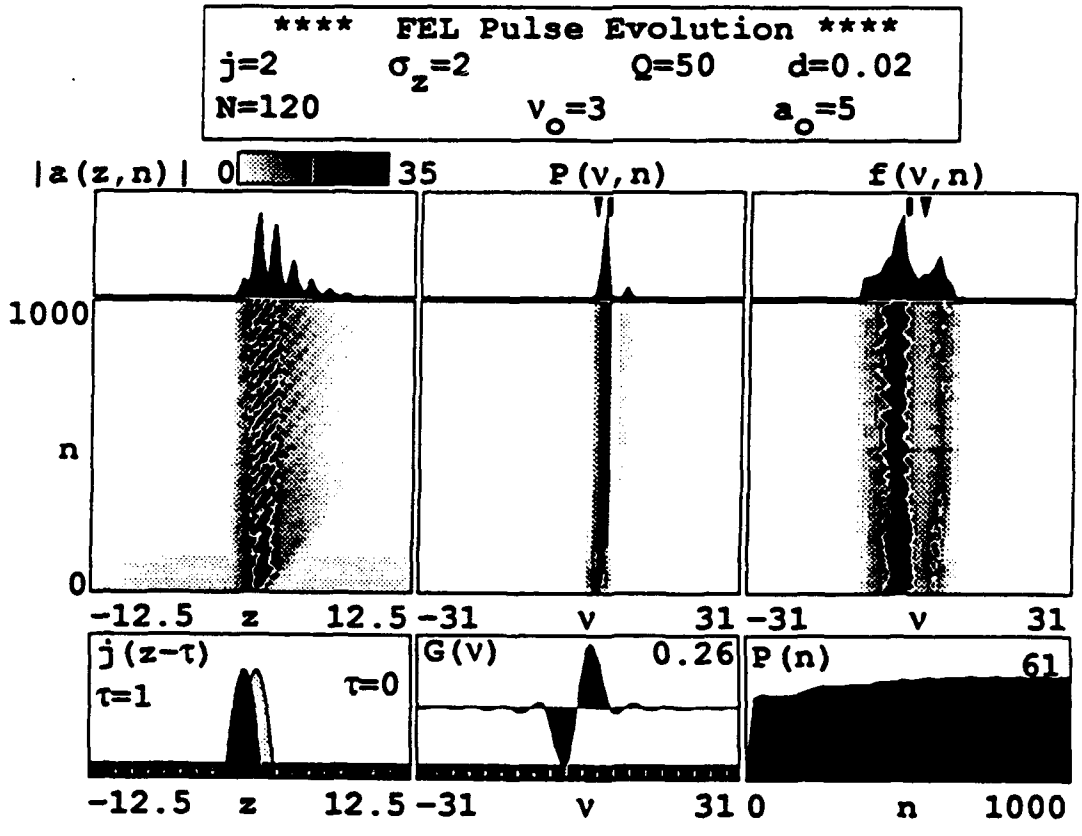

Figure 3-8. Short pulse evolution in a low-gain FEL oscillator.

The calculational window is $W = 19$ slippage distances long, and stays with the optical pulse. Shown at the lower-left, the electron pulse $j(z - \tau)$ has a pulse length $\sigma_z = 2$ with a peak current $j = 2$. The initial position of the electron pulse is determined by desynchronism $d = 0.02$ and is indicated in light grey at $\tau = 0$. The electron pulse is slower than the light pulse, and slips back to the position indicated in dark grey at $\tau = 1$. The weak-field gain spectrum $G(\nu)$ centered at $\nu = 0$ is plotted for reference. The undulator contains $N = 120$ magnetic periods, and resonator losses are determined by $Q = 50$. The electrons are mono-energetic at a phase velocity $\nu_0 = 3$. They interact with an initial optical field $a_0 = 5$ around the regime of peak gain. During simulation over $n = 1000$, passes the optical field evolves subject to amplification by consecutive electron pulses and to uniform loss described by Q [3].

Each pass, a new electron pulse slips back in z and bunches as it passes through the local radiation field $a(z, n)$. As coherent bunching develops, the optical field is amplified. Over many passes, the optical spectrum $P(\nu, n)$ narrows through mode competition around peak gain, and the optical power $P(n)$ grows to steady state. The pointed tick mark at the top of the final power spectrum $P(\nu)$ indicates the central wavelength of the initial radiation at resonance. The rectangular tick mark shows the center of the final power spectrum

The peak optical field, $|a(z, n)| = 35$, is large enough to permit the trapped particle instability. The optical power, $P(n)$, grows to saturation early and remains steady for about 200 passes; then the power increases again with the onset of the instability. The extra power is a result of sideband growth, since the fundamental optical mode remains saturated [31].

A stable optical sideband appears in $P(\nu, n)$ near the fundamental at $\nu_o + \nu_s$. This corresponds to a shift away from the fundamental wavelength by $\Delta\lambda/\lambda = \nu_s/2\pi N$ [3]. As the electrons which are trapped in the potential wells execute synchrotron oscillations, they continually modulate the optical wavefront. This modulation is seen in $|a(z, n)|$ after about $n \approx 300$ passes.

Many of the electrons in the phase velocity distribution are tightly bunched in closed orbits, as indicated by the dark band in $f(\nu, n)$. The pointed tick mark at the top of the final phase velocity spectrum $f(\nu)$ indicates the phase velocity of the electrons at the beginning of each pass n. Initially inserted with phase velocity $\nu_o = 3$, they lose energy to the optical wave and bunch slightly below resonance $\nu_o = 0$. The value of the electron beam's averaged phase velocities at the end of the interaction is marked by a rectangular tick above $f(\nu)$. After $n = 300$ passes, the trapped particle instability causes the distribution $f(\nu, n)$ to modulate, but the electrons still remain closely bunched.

J. DESYNCHRONISM EFFECTS

When the electron and optical pulse are both synchronized at $d = 0$, they enter the undulator at the same time. The leading edge of the optical pulse immediately begins to over-take the electron pulse. However, for small time $\tau \ll 1$ the weak-field gain equation (3.24) can be written $G(\tau) \approx j\nu_o\tau^4/12$. The optical wave experiences no gain at the beginning of the undulator and the electron bunching is slow to occur. This results in a delay of the electron-optical gain mechanism which is termed "lethargy" [3]. The initial part of the optical pulse is poorly coupled to the electron beam and begins to decay. As time continues, the increased gain and corresponding bunching of electrons provides good interaction coupling. This causes the back of the

optical pulse to grow, distorting the optical pulse. This distortion continues on each subsequent pass as gain is preferentially deposited on the trailing edge of the pulse [3]. In effect, the centroid of the light pulse travels at a speed slightly slower than c. Over many passes, gain continues to grow on the trailing edge at the expense of the front of the pulse. Finally, the optical pulse centroid actually moves away from the electron pulse, and the optical wavefront is no longer driven by bunched electrons and power decays. Steady state FEL power is zero at exact desynchronism.

The slower speed of the light pulse is more properly matched to the speed of the electron pulse by adjusting desynchronism, $d = -2\Delta S/N\lambda$, to reduce the optical path length S. Figure 3-9 plots the normalized steady state optical power and weak-field gain over a range of desynchronism distances $d = 0 \rightarrow 0.061$ for a low-gain, short-pulse FEL.

Near $d \approx 0$, lethargy effects restrict FEL coupling and steady state power is zero. Increasing desynchronism to $d \approx 0.003$ leads to a sharp peak in optical power, where the electron and optical pulse repetition rates are most nearly matched. Here, the FEL is subject to the trapped particle instability and the development of optical sidebands arising from strong optical fields. Also, mechanical vibration of the optical cavity in an FEL oscillator can cause unpredictable changes in desynchronism. Even though power is at a peak, operation of the FEL at this desynchronism will likely lead to unstable optical output.

When d is increased further, power falls off steadily, but weak field gain grows to a maximum at $d = 0.028$. In this region, the FEL is less likely to be affected by optical vibration or noise since gain at the maximum peak is fairly level and the incremental change in power is nearly linear.

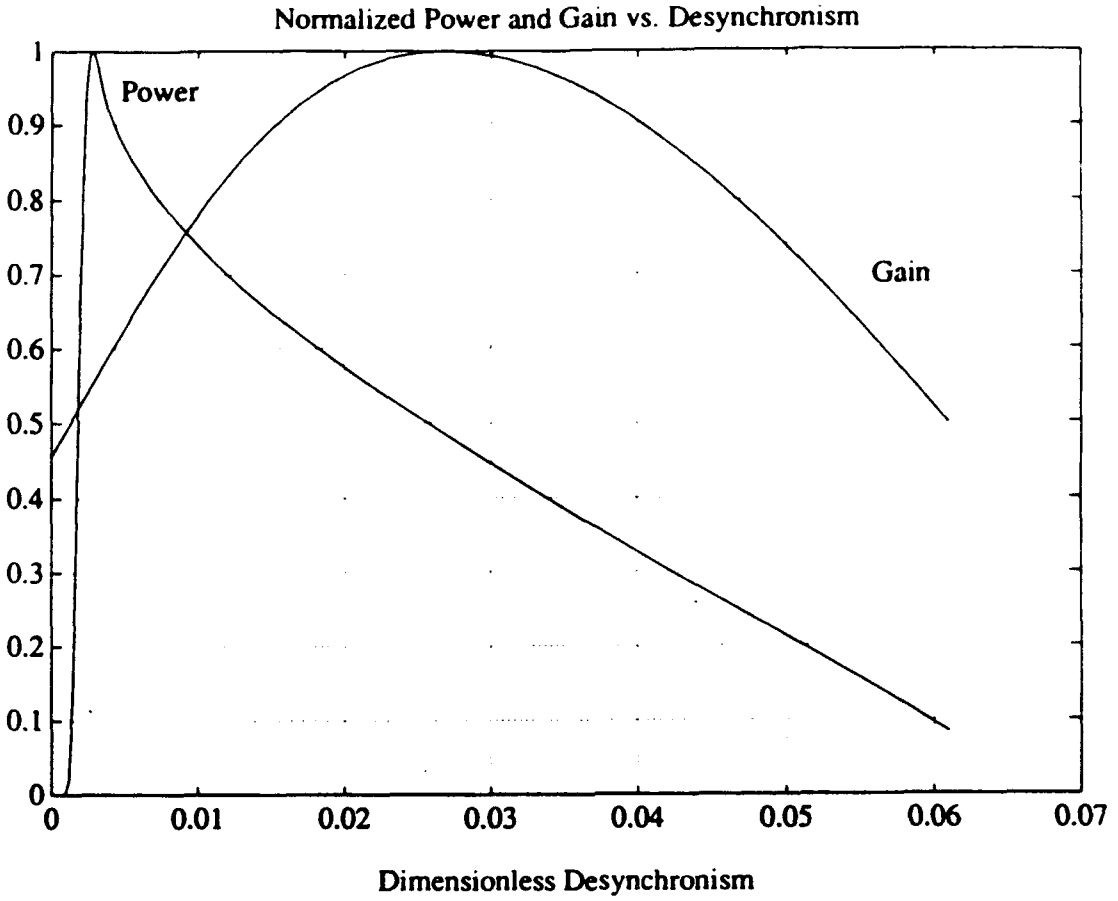

Figure 3-9. Simulated desynchronism curve for a low-gain, short-pulse FEL.

When d is very large, the compensation is too severe, and overlapping of the electron and optical pulses cannot occur over a sufficient number of passes n. FEL interaction coupling deteriorates, again resulting in decreased power and gain.

IV. RESONANT WAVELENGTH MODULATION THEORY

A. ELECTRON BEAM ENERGY MODULATION

The resonance equation (3.2) governs the interaction between the electrons and the optical wave in an FEL. The change in resonance due to a variation in the electron beam energy $\Delta\gamma mc^2$ is given by $\Delta\nu = 4\pi N \Delta\gamma/\gamma$. The corresponding fractional wavelength variation is $\Delta\lambda/\lambda = -\Delta\nu/2\pi N$. Over many passes, beam energy changes are simulated by superimposing a sinusoidal variation in electron phase velocity around ν_o. The resonant phase velocity then becomes

$$\nu(n) = \nu_o + A_o \sin\left[\frac{2\pi n}{N_o}\right] \quad . \tag{4.1}$$

The electron beam phase velocity is modulated by amplitude A_o and makes one complete oscillation after N_o incremental passes n. Since an optical pulse travels twice the length of the resonator, S, in a single pass, the time per pass is $\Delta t = 2S/c$. The frequency of electron beam modulation becomes $f_o = c/2SN_o$. The sensitivity of an FEL to electron beam energy modification can be explored using coherence and short-pulse theory.

B. COHERENCE AND MODE COMPETITION EFFECTS

Figure 4-1 shows the coherence evolution over $n = 7500$ passes for an FEL with $N = 120$ undulator periods and beam current density $j = 2$. Optical loss per pass is determined by $Q = 50$. The input electron beam energy is modulated with amplitude $A_o = 1\pi$, taking $N_o = 1000$ passes to complete each oscillation. The modulation is centered about $\nu_o = 3$, corresponding to the position for peak gain. The weak field

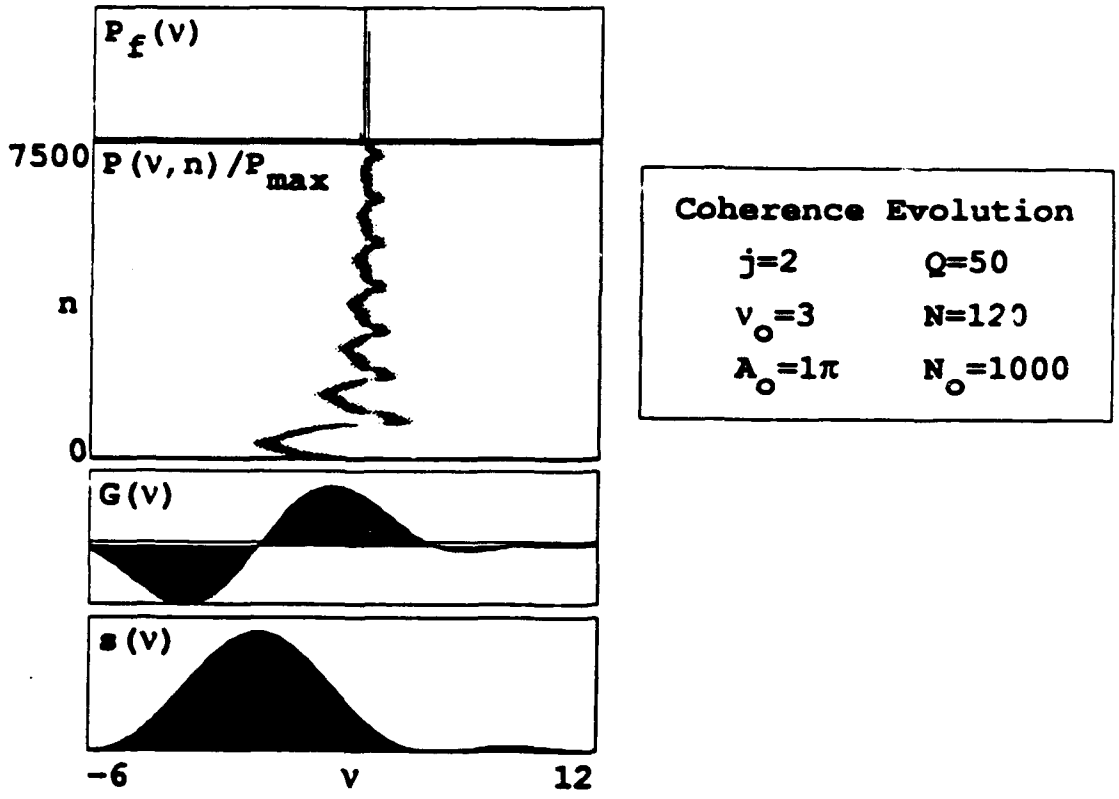

Figure 4-1. Coherence evolution for low-gain FEL with constant small-amplitude electron beam modulation.

gain spectrum $G(\nu)$ and the spontaneous emission spectrum $s(\nu)$ are shown at their initial positions at pass $n = 0$. The resonance equation (3.2) requires that $G(\nu)$ and $s(\nu)$ shift along the phase velocity ν-axis as the electron beam energy changes. When the electron energy varies sinusoidally, the spectrum moves back and forth in ν. Optical power starts from $s(\nu)$ and grows through $G(\nu)$. The optical spectrum $P(\nu, n)$ is normalized to the maximum power at each pass n, so that net power growth and decay are not shown. Over the first $n \approx 1000$ passes, the optical spectrum is broad and readily follows changes in electron beam energy. However, mode competition forces $P(\nu, n)$ to narrow with each successive pass. As the optical spectrum narrows, it

becomes more resistant to resonant beam energy modulation, and cannot follow. The magnitude of oscillation of the optical spectrum decreases, and steady-state optical wavelength modulation is never achieved.

An increase in electron modulation amplitude to $A_o = 3\pi$ is demonstrated in Figure 4-2, for n = 1500 passes. All other FEL parameters remain the same.

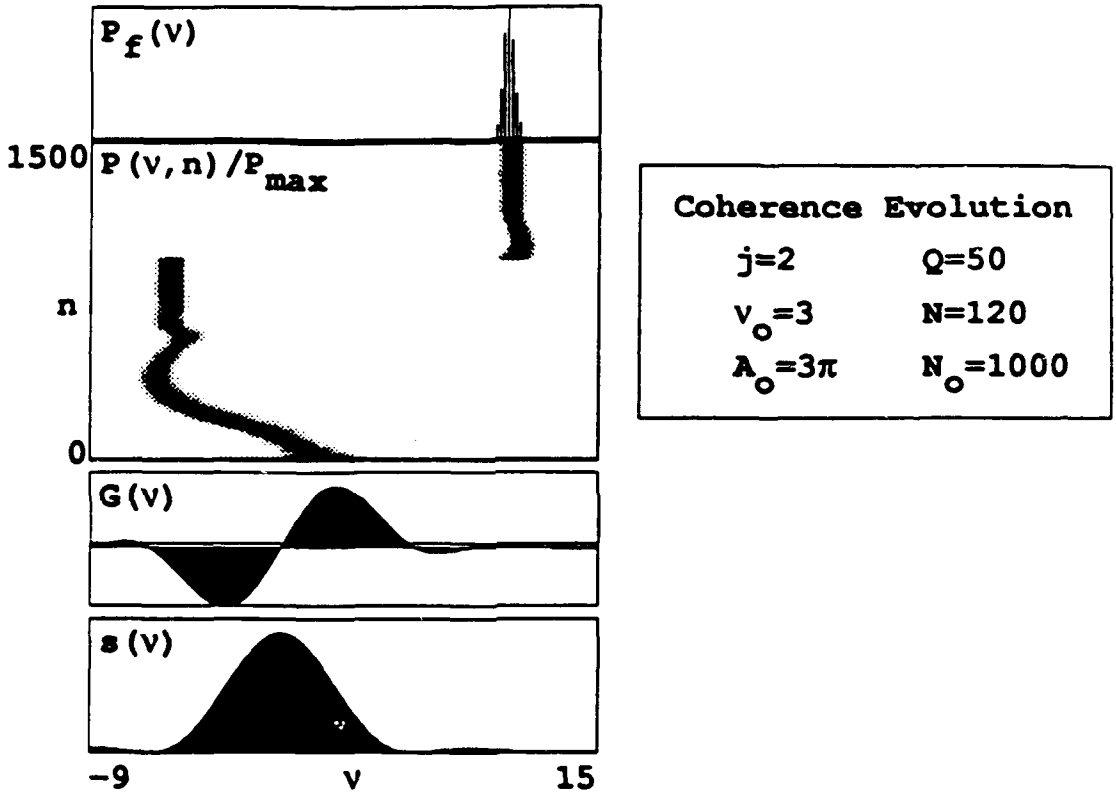

Figure 4-2. Coherence evolution for low-gain FEL with large amplitude electron beam modulation.

The optical spectrum $P(\nu, n)$ initially follows the shift in $G(\nu)$ and $s(\nu)$. The first maximum of the modulation is reached at $n \approx 250$ passes. When $\sin(2\pi n/N_o)$ is at its maximum value, both $G(\nu)$ and $s(\nu)$ stay near the same optical mode $\nu(k) \approx -6$ for a longer period of time, and mode competition during that time begins to narrow

$P(\nu, n)$. As the optical spectrum narrows, it becomes resistant to resonant electron beam changes. When the resonant electrons move away from $\nu(k) = -6$, the light remains in a single mode and decays according to Q. When the electron energy modulation reaches the next maximum of $\sin(2\pi n/N_o)$ at $n = 750$ passes, both $G(\nu)$ and $s(\nu)$ again remain near a single mode for a longer period of time. Optical power starts from $s(\nu)$ and grows through $G(\nu)$. As the optical mode again narrows, the resonant electrons move away from $\nu(k) = 12$, and the optical spectrum $P(\nu)$ remains near that mode to narrow and decay.

The simulations used for Figure 4-1 and Figure 4-2 only show coherence development and mode growth trends based on Equation (3.30). Strong fields are not considered, and therefore the trapped particle instability cannot be simulated. The broadening of the optical spectrum and increased power that accompanies the trapped particle instability can serve to enhance the ability of an FEL to respond to changes in the electron beam energy. Further, short electron pulses inherently broaden the optical spectrum, again allowing an FEL to follow the resonant electron energy modulation. Short pulse theory provides the perfect medium for studying related effects.

C. LOW AMPLITUDE, HIGH FREQUENCY MODULATION

The response of a short-pulse FEL to resonant electron beam energy modulation is examined using the same FEL dimensionless parameters as in Figure 3-8. The input electron energy ν_o is subject to the sinusoidal variation described by (4.1). Figure 4-3 shows one such simulation. The energy of consecutive electron pulses oscillates with amplitude $A_o = \pi$ and period $N_o = 150$ passes per oscillation. Just over three energy oscillations are completed over $n = 500$ passes.

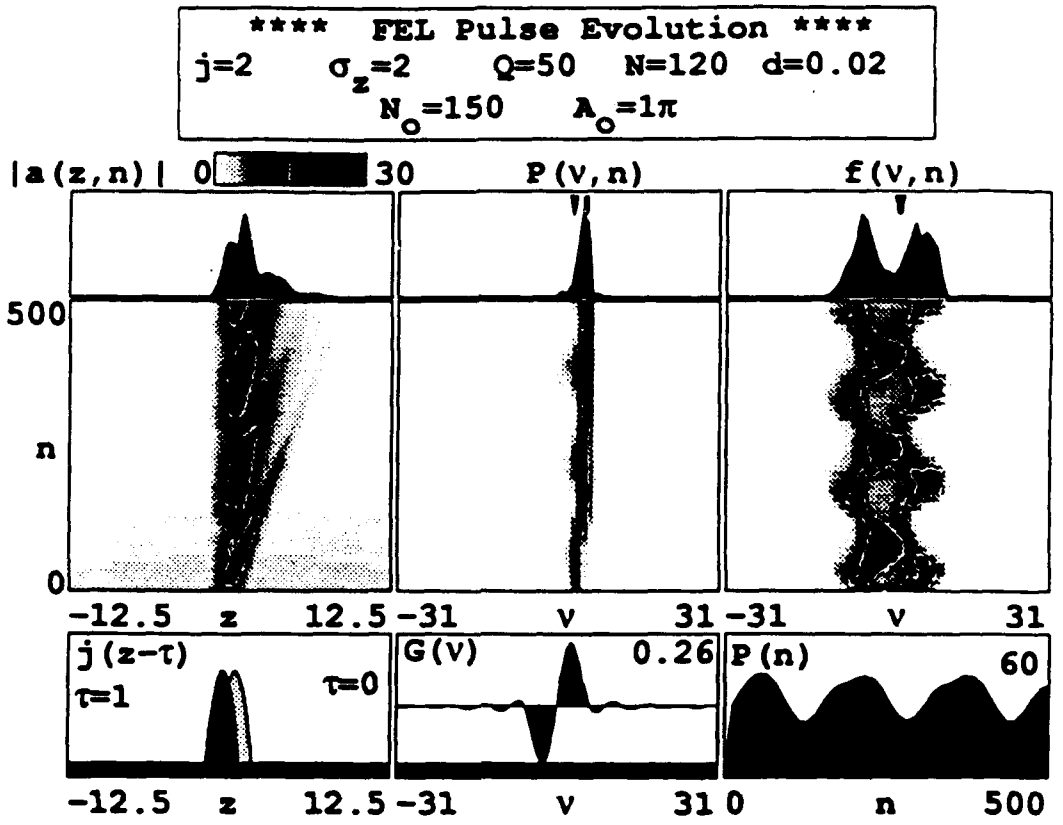

Figure 4-3. Short pulse evolution for low-gain FEL oscillator subject to very high frequency electron beam energy modulation.

Both the optical power spectrum $P(\nu, n)$ and the electron energy distribution $f(\nu, n)$ are plotted with respect to the dimensionless electron phase velocity ν. The phase velocity can be expressed in the form

$$\nu = L\left[k_o\beta_z - \frac{2\pi}{\lambda}\frac{1+K^2}{2\gamma^2}\right], \tag{4.2}$$

showing the dependence on electron energy γ and optical wavelength λ. The optical power spectrum is given in terms of $\nu(\lambda)$, so $P(\nu, n) \rightarrow P(\nu(\lambda), n)$. The electron phase velocity distribution becomes a function of $\nu(\gamma)$, so $f(\nu, n) \rightarrow f(\nu(\gamma), n)$.

Increasing values of phase velocity v correspond to longer wavelengths λ and higher electron energies γ.

The phase velocity distribution $f(v(\gamma), n)$ shows the electron energy oscillation directly. During each cycle, bunches of electrons below resonance give energy to the optical wave, increasing the optical field $a(z, n)$ and the optical power $P(n)$. Conversely, electrons that bunch above resonance take energy from the optical wave, and both $a(z, n)$ and $P(n)$ decrease. The result is that optical power $P(n)$ oscillates with the frequency of the input electron energy. The peak optical power $P = 60$ is nearly the same as the steady state power in Figure 3-8, but the average power $P \approx 40$ is much less.

The optical spectrum $P(v(\lambda), n)$ appears to undergo variation in width, but the wavelength does not modulate with significant amplitude. Electron energy oscillation is too rapid for the resonant wavelength to follow. The spectrum remains within a small variation $\Delta\lambda$ about the center of oscillation of the weak field gain spectrum $G(v)$. Small sidebands attempt to form on either side of the fundamental power, but rapidly die away each cycle. The final optical spectrum $P(v(\lambda))$ is broader than that in Figure 3-8, but not subject to large amplitude sidebands. Pulse modulation in $a(z, n)$, which is seen in Figure 3-8, has diminished.

In Figure 4-4, the modulation frequency has been decreased. One complete electron energy oscillation takes place every $N_o = 500$ passes. The band of electrons below $v = 0$ in the phase velocity distribution $f(v(\gamma), n)$ is more even throughout the simulation, indicating more consistent bunching. The added bunching coherence produces a peak optical power $P = 74$, which is greater than that shown in Figure 4-3. Again, bunches of electrons periodically form to the right of $v = 0$ in $f(v(\gamma), n)$. They take energy from the optical wave, causing the optical power $P(n)$ to oscillate.

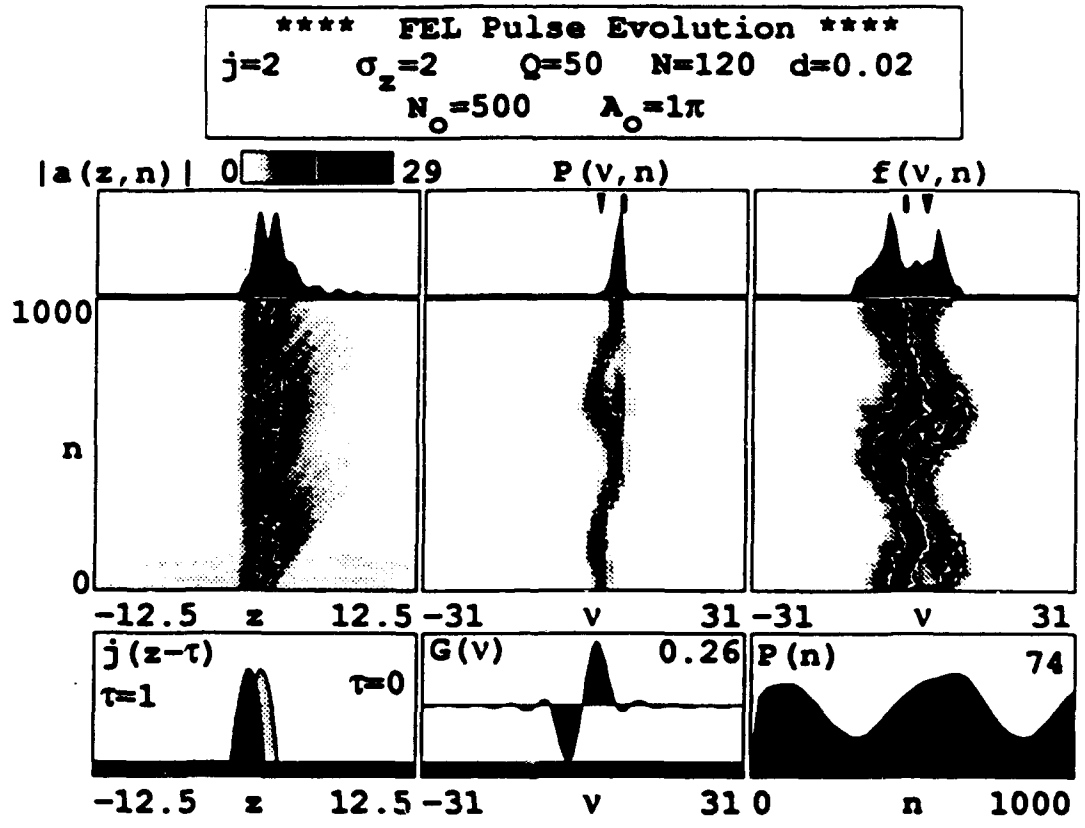

Figure 4-4. Short pulse evolution for low-gain FEL oscillator subject to high frequency electron beam energy modulation.

Variation of the optical wavelength is also illustrated. Movement of the electrons in $f(\nu(\gamma), n)$ to the right along the phase velocity ν-axis corresponds to an increase in electron beam energy. The resulting change in the resonance equation (3.2) shortens the optical wavelength at the output, which is marked as movement to the left in $P(\nu(\lambda), n)$. The optical wavelength follows at the frequency of the electron energy oscillation.

As shown in Figure 4-5, an increase in modulation amplitude to $A_o = 2\pi$ suppresses the effects of the trapped particle instability. The peak optical pulses in $a(z, n)$ are highlighted by a white contour line. They are markedly smoother, but

decrease slightly in longitudinal length z near the middle of each cycle. This results in a slight dip near each peak in the modulation of optical power $P(n)$.

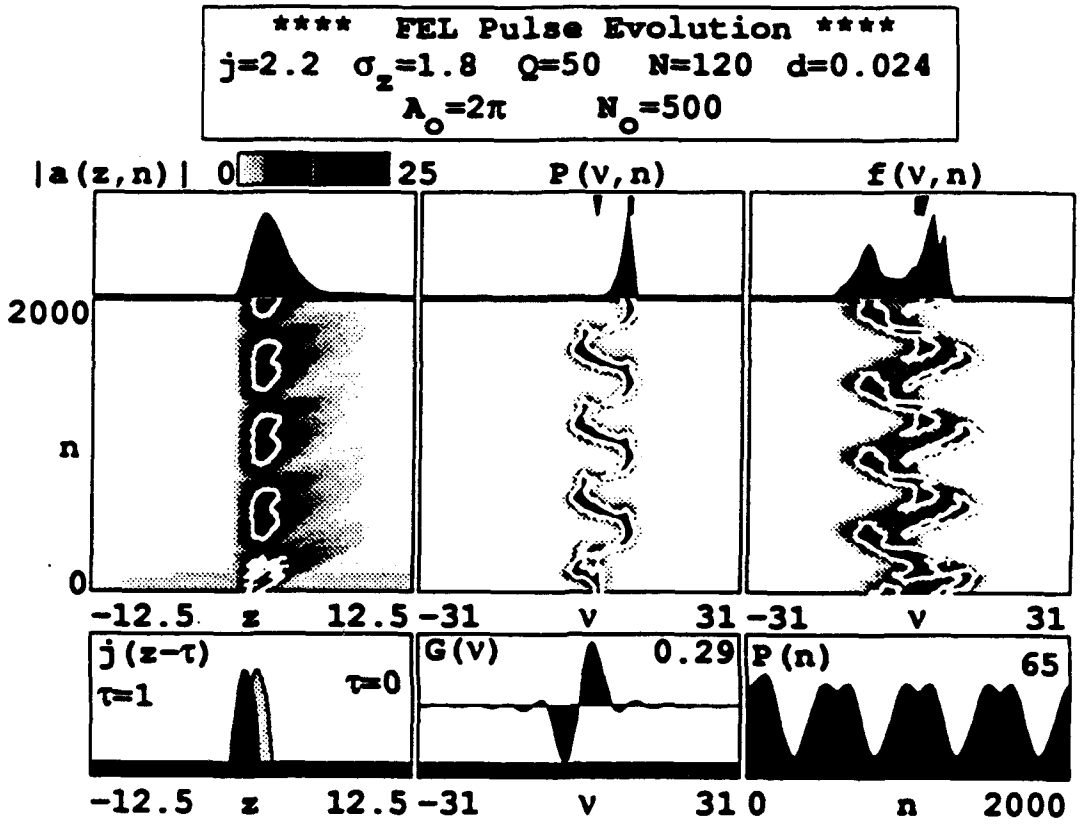

Figure 4-5 Short pulse evolution for low gain FEL. The optical spectrum $P(\nu(\lambda), n)$ preferentially follows resonant electron energy γ toward shorter wavelengths λ.

Wavelength modulation is clearly visible, but power in the optical spectrum is only significant when the electron beam is slewed toward increasing energy, which is depicted as movement to the right in $f(\nu(\gamma), n)$. Through the resonance condition (3.2), the optical pulse must shift toward shorter wavelengths λ, so the optical spectrum $P(\nu(\lambda), n)$ moves to the left. Optical power preferentially follows change toward shorter wavelengths. This is because of changes in the optical gain spectrum $G(\nu_o)$ in response to the stronger initial optical fields.

Figure 4-6 illustrates the change in $G(\nu_o)$ as the initial optical field strength a_o is increased [32]. The gain spectrum is calculated for each point in the (ν_o, a_o) plane for an electron beam current of $j = 2$ injected into an undulator consisting of $N = 120$ magnetic periods. In weak fields $a_o \leq \pi$, the gain spectrum is independent of a_o and looks like $G(\nu)$ shown in Figure 4-5.

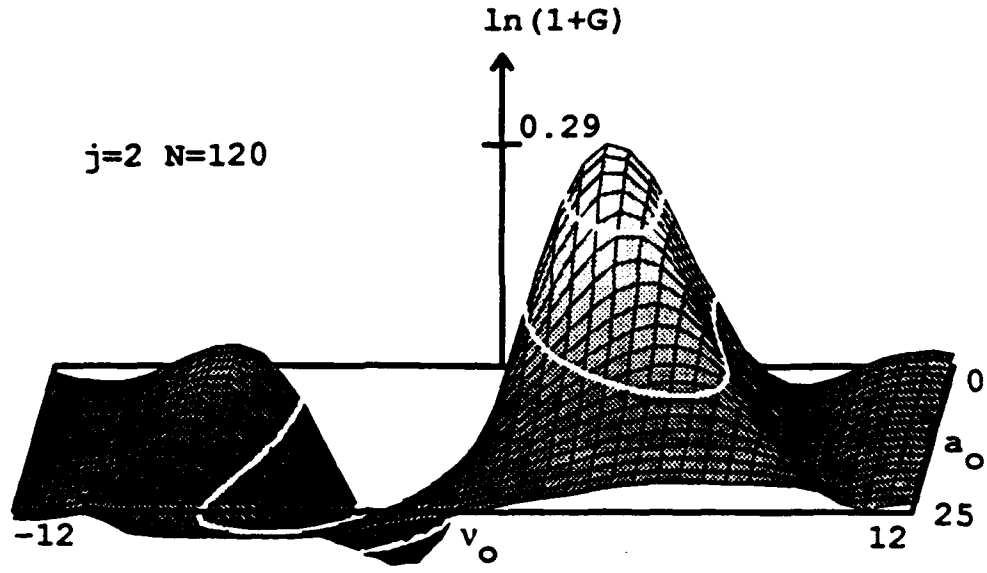

Figure 4-6 Gain spectrum $G(\nu_o)$ for low gain FEL with increasing optical field strength a_o.

The spectrum is antisymmetric about $\nu_o = 0$ with a maximum value $G = 0.29$ located at $\nu_o \approx 2.6$, and a minimum value $G = -0.29$ located at $\nu_o \approx -2.6$. As the initial optical field grows, the phase velocity corresponding to peak gain increases away from resonance $\nu_o = 0$. The value for peak gain decreases and becomes broader in the phase velocity ν_o. At the initial optical amplitude $a_o = 25$, the peak gain has decreased to $G = 0.035$ and is spread over phase velocities $\nu_o \approx 4 \rightarrow 8$.

As optical power $P(n)$ grows to saturation, electrons in $f(\nu(\gamma), n)$ bunch and lose energy to the optical wave. Meanwhile, the initial phase velocity corresponding to

peak gain increases, so the optical wave changes frequency to follow maximum gain. Recall in Figure 3-8 that the steady state power for a constant energy electron beam with a beam current $j = 2$ is $P \approx 61$ at $v \approx 5$.

At saturation the entire gain spectrum $G(v_o, a_o)$ shifts back and forth along the v-axis as the resonant electron energy is modulated. When the electron energy is increased through modulation, the electrons in $f(v(\gamma), n)$ move to the right along the v-axis. The gain spectrum moves to the left along the v-axis according to the resonance condition (3.2). See Figure 4-7.

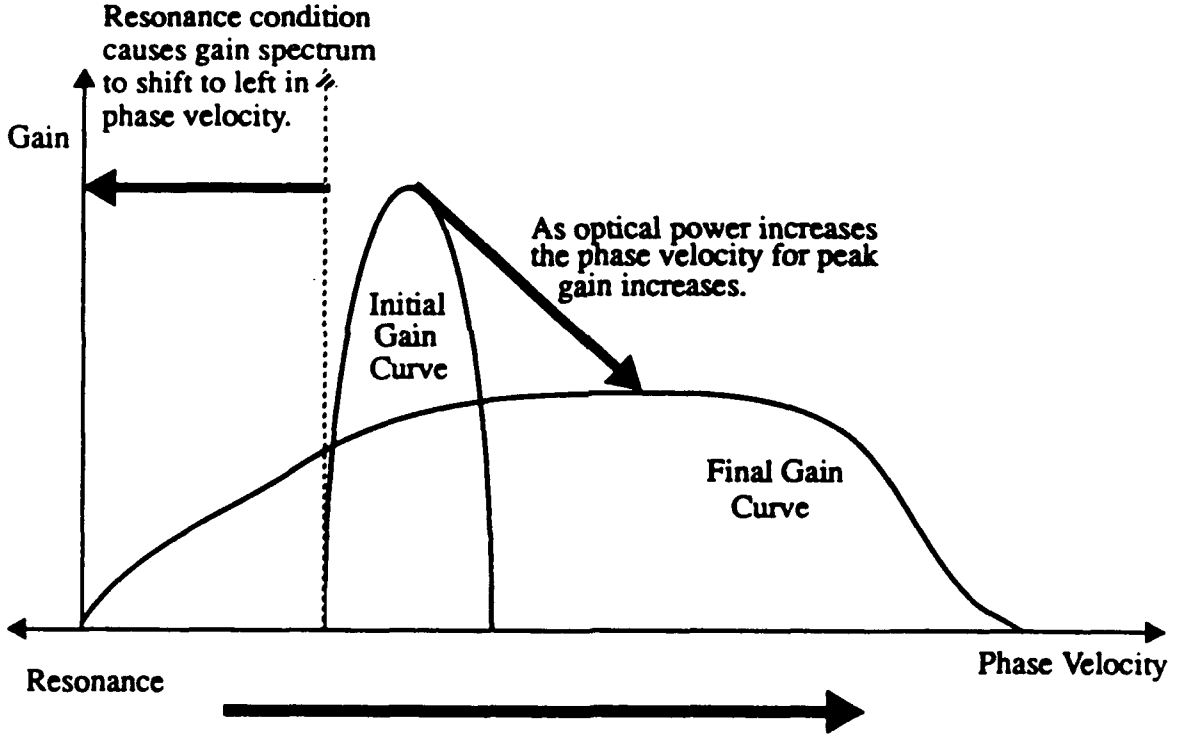

Figure 4-7 Schematic illustrating the primary effects that allow an FEL to slew preferentially toward shorter optical wavelengths λ in response to electron energy modulation. Here electron energy γ increases and electrons in $f(v(\gamma), n)$ shift to the right. The gain spectrum $G(v(\lambda), n)$ shifts to the left, but peak gain moves away from resonance to the right. FEL interaction between the bunched electrons and peak gain takes place over a longer period of time, and power is more able to follow the resonant energy shift.

If, at the same time, optical power P increases at either end of modulation, then the phase velocity corresponding to peak optical gain also increases. All three of these events combine to create a favorable condition under which resonance is maintained for a longer period of time than for normal steady state operation. The effect results in peak power $P \approx 65$ which is greater than the normal saturation power. Conversely, when the electron energy is decreased through modulation, and power $P(n)$ increases, movement of the gain spectrum $G(\nu)$ to the right along the ν-axis forces electrons to fall out of resonance more rapidly. The net result is for the FEL to shift more readily toward shorter optical wavelengths in response to electron beam modulation.

D. LOW FREQUENCY MODULATION

Other effects are observed by decreasing the frequency of the resonant energy modulation. Shown in Figure 4-8 is the result of a simulation with $N_o = 4000$ and with increased amplitude $A_o = 2\pi$. To better show detail in the FEL behavior, the simulation only follows one electron energy modulation period over 4000 passes.

The electron energy varies slowly in time, so many of the characteristics found in Figure 3-8 for a constant energy electron beam apply. The oscillation in $f(\nu(\gamma), n)$ causes wide variation in the optical wavelength, which is depicted as movement along the ν-axis in $P(\nu(\lambda), n)$. Optical power $P(n)$ oscillates with amplitude variation. The average power is as large as the steady state power achieved in Figure 3-8. Since higher power is achieved, the trapped particle instability has returned. Because the variation in resonant beam energy is slow, the optical sidebands are able to form and grow to stable power. The fundamental optical power spectrum remains narrow throughout the modulation. However, as the optical sidebands follow alongside, the final optical spectrum is widened.

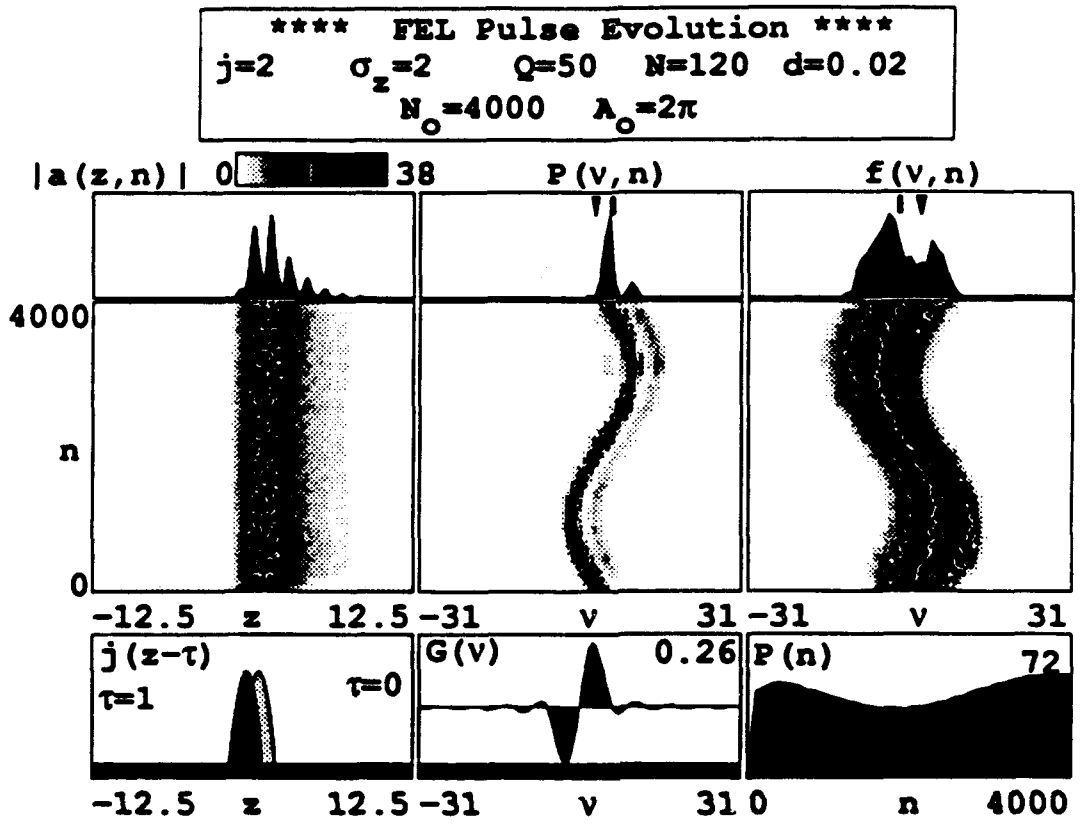

Figure 4-8. Short pulse evolution for low-gain FEL with low frequency electron beam energy modulation.

E. HIGH AMPLITUDE MODULATION

In Figure 4-9, the amplitude of modulation has been increased to $A_o = 10\pi$ with $N_o = 1000$ passes per oscillation. The electron phase distribution $f(\nu(\gamma), n)$ is narrow and slews rapidly back and forth along the ν-axis. Electron bunching occurs at both ends of the slew, but the largest optical gain occurs only below $\nu = 0$. The optical spectrum $P(\nu(\lambda), n)$ is much like that shown in Figure 4-2, but in contrast the optical spectrum briefly follows resonance on each sweep.

The contour plot of the optical field $a(z, n)$ shows alternating large and small amplitude peaks. Each optical peak is short-lived in n. The optical pulses are

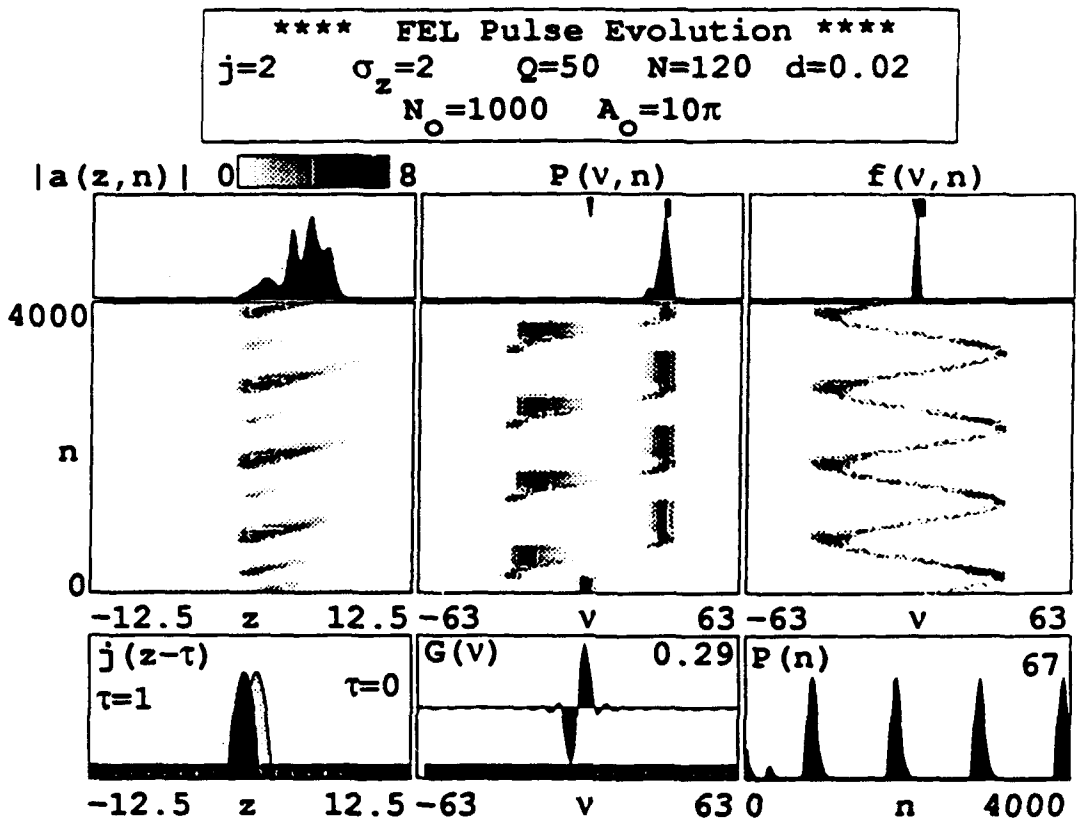

Figure 4-9. Short pulse evolution for low-gain FEL. Large amplitude electron beam energy modulation produces steady-state optical macropulses in $P(n)$.

observed to move ahead in z due to desynchronism d as the number of passes n is increased. The larger amplitude optical peaks are produced when electrons bunch below $\nu = 0$ in $f(\nu(\gamma), n)$. The smaller optical peaks come from electrons bunched above $\nu = 0$ in $f(\nu(\gamma), n)$. The picture at the top-left profiles the final optical pulse after pass number $n = 4000$ showing a peak in $a(z, n)$. Modulated subpulses along z are indicative of trapped particle instability which takes place during periods of maximum bunching.

The optical field is observed to grow rapidly only when electrons are bunched below $\nu = 0$ in $f(\nu(\gamma), n)$. The result is that the optical power $P(n)$ peaks in n

periodically with peak power greater than that achieved from the constant energy FEL in Figure 3-8. The peaks in optical power are produced by electrons bunched at lower phase velocities, so that the output wavelength is longer.

In effect, the FEL interaction is timed by the electron energy modulation. This process appears to be related to Q-switching in conventional lasers, where the optical cavity losses Q_c are artificially raised in order to build up a much larger than usual population inversion inside the cavity. Then, Q_c is suddenly lowered producing a high power "giant pulse" at the output [3]. In the case of the short pulse FEL, Q remains constant, but the off-resonant electrons reduce the interaction. When the optical pulse and electrons become resonant for a significant time, they provide gain above the loss for a few passes, and the optical power pulses.

The optical power spectrum $P(\nu(\lambda), n)$ shown in Figure 4-9 is normalized with respect to the maximum power at each pass so that movement along ν can be more clearly followed. Figure 4-10 plots the actual power $P(n)$ over the range of dimensionless phase velocities ν at each pass n. The result is a three dimensional optical spectrum in which optical wavelength information is obtained directly from the phase velocity axis since $\nu \rightarrow \nu(\lambda)$. The four large-amplitude peaks in power have the same wavelength, magnitude, and pulse shape. Note that the optical power attempts to follow the resonant electron energy but rapidly decreases in amplitude as the resonant electron energy moves away from the maximum wavelength.

F. ELECTRON PULSE LENGTH EFFECTS

In short pulse theory, the electron pulse shape is assumed to be parabolic. On each pass, the electron pulse is inserted just ahead of the optical pulse as determined by desynchronism. The interaction takes place as the optical pulse passes over the electron pulse while both traverse the undulator. The net electron beam current

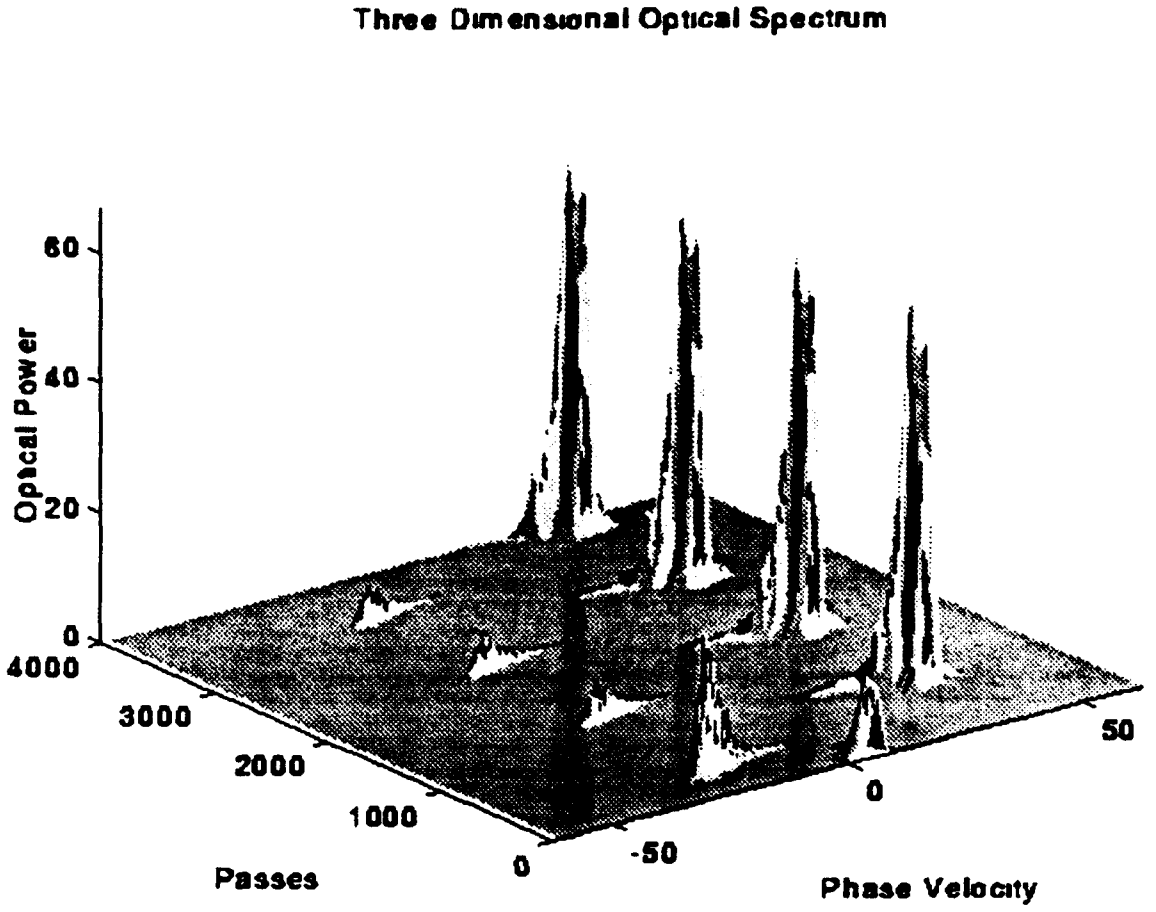

Figure 4-10. Three-dimensional optical spectrum. Optical power P is displayed as a function of dimensionless phase velocity $v(\lambda)$ and time n. Simulation parameters are the same as those used in Figure 4-9.

increases with increasing pulse length σ_z for fixed peak current j. Increasing the net current leads to higher net gain.

In Figures 4-11 through 4-13, the electron pulse length is increased over the range $\sigma_z = 0.3 \rightarrow 3.0$. All other FEL parameters are held constant. The electron beam energy is modulated with a period $N_0 = 1000$ passes per oscillation at a relatively large amplitude of $A_0 = 8\pi$. Figure 4-11 has low net gain with a short pulse of $\sigma_z = 0.3$. The resulting optical field strength is low with a maximum value $|a| \approx 6$, so there is no trapped particle instability throughout the simulation. The optical spectrum $P(v, n)$ is

normalized with respect to the maximum power at each pass in order to show movement of the resonant wavelength. But the optical power $P(n)$ is only significant when the electrons in $f(v, n)$ bunch below $v = 0$. The optical power peaks occur at the maximum in optical wavelength modulation, where the change in resonance is slowest. The peaks are seen as dark areas in the optical field contour map $|a(z, n)|$ and as spikes in the optical power $P(n)$. The peak optical power is low with a value $P \approx 3$.

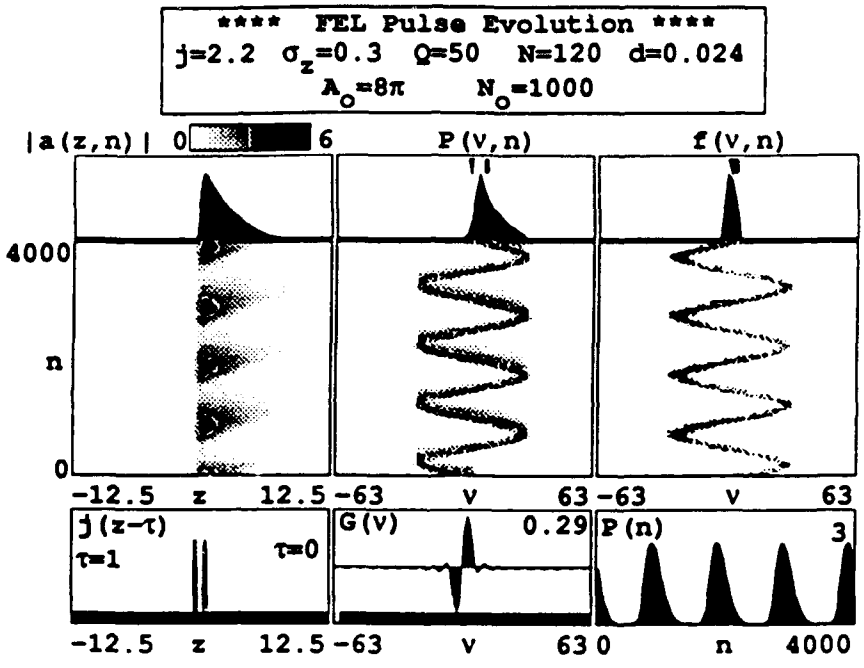

Figure 4-11. Pulse evolution simulation for FEL oscillator with electron pulse length $\sigma_z = 0.3$.

Figure 4-12 illustrates the effects of lengthening the electron pulse to $\sigma_z = 0.8$. Many of the characteristics shown in Figure 4-5 are observed here. Optical power preferentially follows resonant wavelength shifts toward shorter optical wavelengths. The optical power between modulation maximum and minimum values is more substantial because of the higher net gain. The secondary optical peaks in $P(n)$

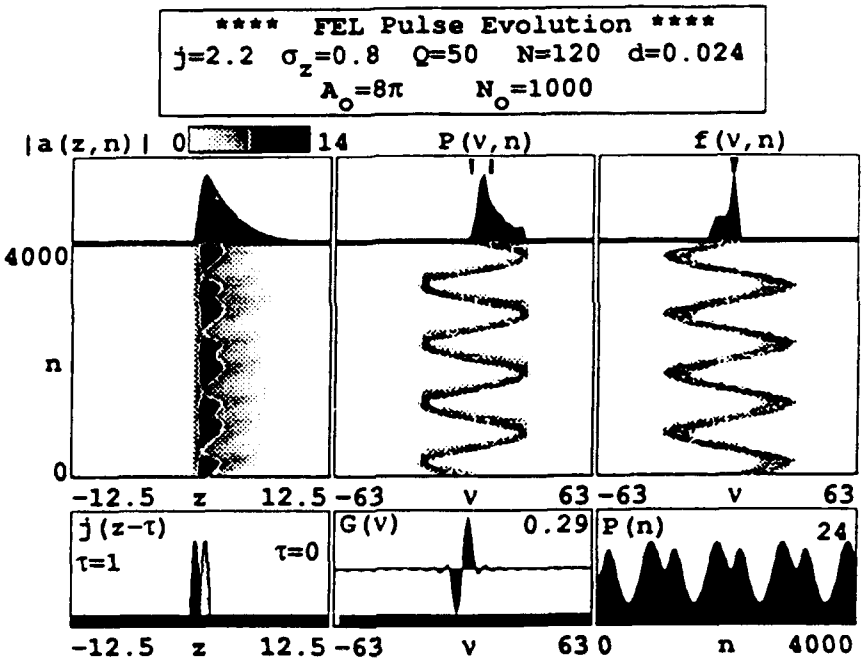

Figure 4-12. Pulse evolution simulation for FEL oscillator with electron pulse length $\sigma_z = 0.8$.

correspond to electron bunching above $\nu = 0$. The peak optical power increases because the FEL interaction efficiency improves with enhanced net gain. However, the maximum optical field magnitude $|a(z, n)|$ is still below the threshold for trapped particle instability. As a result, the optical pulse $|a(z, n)|$ is smooth.

In Figure 4-13 the electron pulse length has been increased by ten times the original value to $\sigma_z = 3$. Electron bunching occurs at both extremes in modulation, but the optical field grows only for bunching below $\nu = 0$. The characteristics are the same as those shown in Figure 4-9. The increase in net gain produces an optical field strength at each peak that is sufficient to cause the trapped particle instability. The large optical power peaks at $P(n) = 113$, occur on the long wavelength side of the modulation. The increased field strength $|a(z, n)|$ in this region allows the optical spectrum $P(\nu, n)$ to narrow, since the resonant wavelength remains near the same

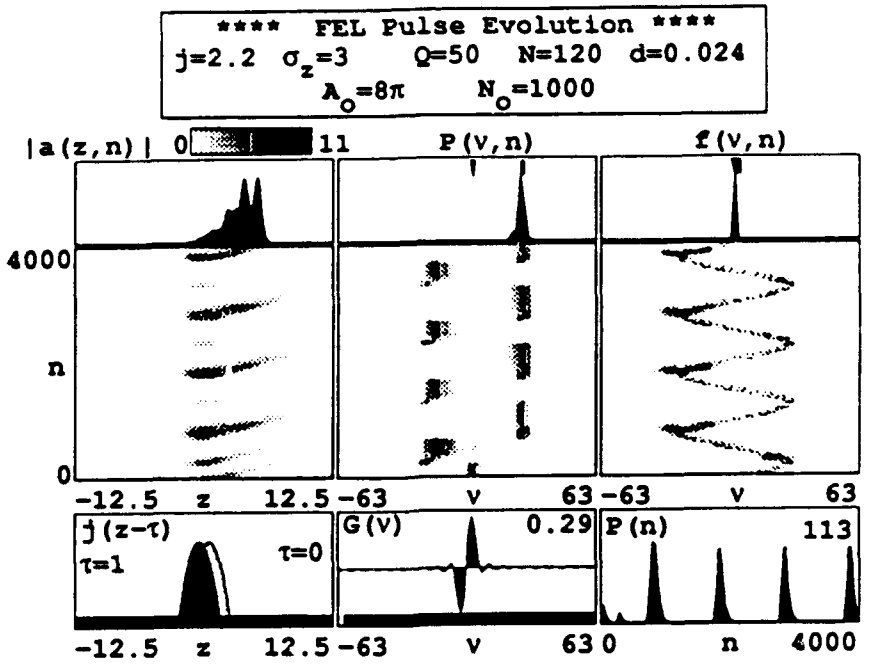

Figure 4-13. Pulse evolution simulation for FEL oscillator with electron pulse length $\sigma_z = 3$.

phase velocity for a longer time. As the optical spectrum narrows, it resists shifts in resonant electron energy and remains at the same optical wavelength to die out until the next cycle occurs.

Figure 4-14 summarizes the effects of increasing pulse length on the power evolution during electron beam modulation with large amplitude $A_o = 8\pi$ at moderate frequency of $N_o = 1000$ passes per oscillation. As the electron pulse length is increased through the range $\sigma_z = 0.3 \rightarrow 3$, the peak power increases through the range $P = 3 \rightarrow 113$. The peaks corresponding to electron bunching below $v = 0$ in electron phase-space remain throughout the increase in pulse length. As the electron pulse length is increased, the net gain increases and the power pulses sharpen and grow. The smaller peaks in optical power corresponding to electron bunching above $v = 0$ do not appear until the pulse length is increased to $\sigma_z = 0.5$. Note that the optical power

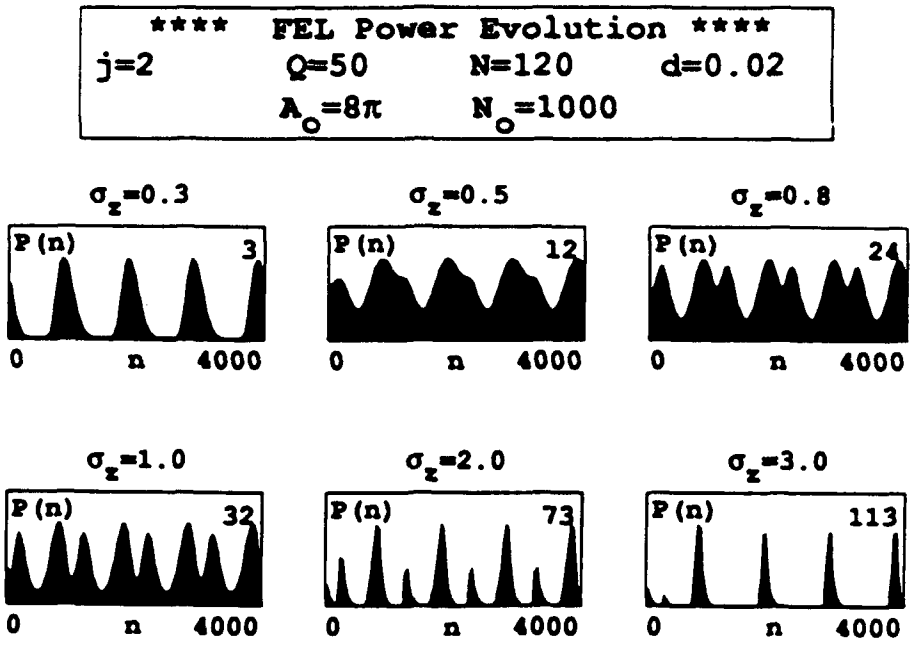

Figure 4-14. Progression in optical power $P(n)$ as net gain increases for large amplitude electron beam energy modulation. Gain increases coincidentally with increasing electron pulse length σ_z.

fills the passes between peaks in this regime because the net gain is sufficient to allow the resonant optical wavelength to follow the electron beam energy modulation. As optical power $P(n)$ grows, mode competition narrows the optical spectrum, so that it resists the resonant wavelength shift. Finally, at $\sigma_z = 3.0$, gain causes power to grow so rapidly at the peaks that mode competition allows the narrow optical spectrum to completely restrict resonant wavelength shifts. The result is high amplitude power switching with an optical wavelength longer than $\nu = 0$.

G. MODULATION AT VARIOUS VALUES OF DESYNCHRONISM

Recall from Figure 3-9 that weak-field gain and steady state optical power vary with dimensionless desynchronism $d = -2\Delta S/N\lambda$. Operation at a small value of desynchronism $d \geq 0$ maximizes optical power, but the weak-field gain is barely above

threshold. Approximately midway through the range of practical desynchronism values, weak-field gain is at a maximum and steady state power is decreasing linearly with increasing desynchronism. Increasing gain at moderate values of desynchronism increases the ability to follow the optical wavelength modulation. Decreasing desynchronism narrows the optical spectrum through mode competition so that the optical pulse resists wavelength modulation. The combined effects are shown in Figure 4-15, where the optical power evolution $P(n)$ is followed over the range of desynchronism values $d = 0.01 \rightarrow 0.1$.

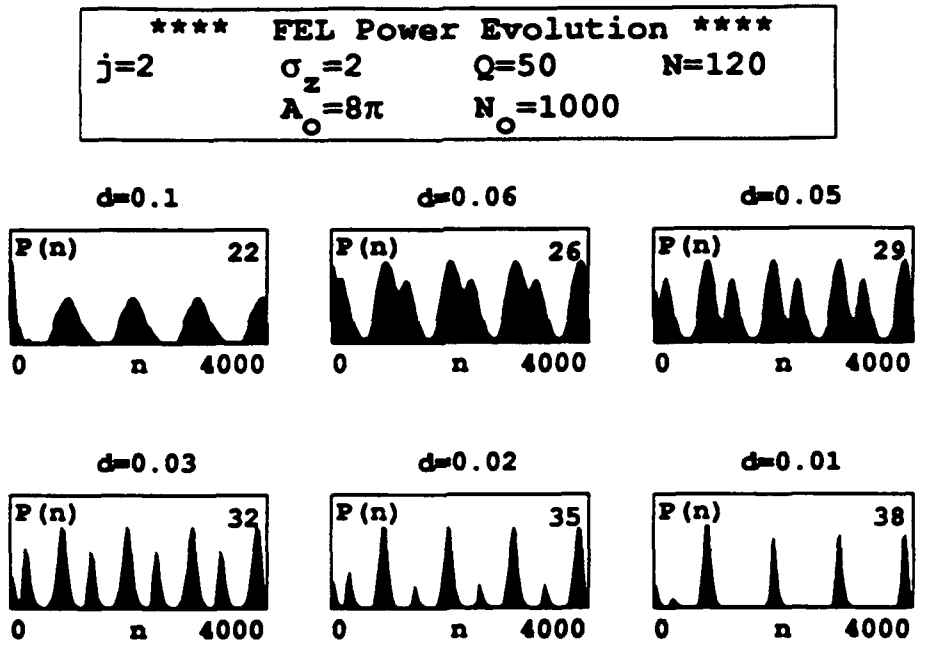

Figure 4-15. Progression in optical power $P(n)$ as steady state power increases for large amplitude electron beam energy modulation. Steady state power increases with decreasing desynchronism d.

The picture at the top left shows power evolution $P(n)$ for a large desynchronism $d = 0.1$. Gain is slightly above threshold, and the steady state power is small. The power pulses in n are wide, indicating that the optical spectrum is following resonant energy over a range of wavelengths. As desynchronism decreases,

the increase in the optical power at the extremes of the modulation leads to resistance of the resonant wavelength movement. A dip in power between the optical peaks is produced as resonance shifts from long to short wavelengths. At $d = 0.03$, the optical power between the modulation extremes is negligible. Since gain is large, the optical power at each peak grows rapidly. Finally, at a small value of desynchronism, $d = 0.01$, the optical power is only large during periods of maximum electron bunching below $\nu = 0$ in electron phase space.

H. MODULATION AT VARIOUS VALUES OF LOSS

In the low gain FEL oscillator, coherence length and width of the optical spectrum is determined by mode competition through Equation (3.30). The weak field gain per pass in each optical mode is given by Equation (3.24). Over many passes n, the optical spectrum narrows as modes with the largest gain continue to grow at the expense of surrounding modes. These modes grow in optical power to saturation, which is determined by resonator losses. To describe resonator losses in the absence of gain, the quality factor Q is defined so that optical power decays proportional to $e^{-n/Q}$ for each mode.

A narrow optical spectrum $P(\nu(\lambda), n)$ degrades the ability of a FEL to follow resonant wavelength modulation. When resonator losses are decreased by increasing the value of Q, the optical modes surrounding the resonant mode remain for a longer period of time. If the resonant wavelength shifts as a result of the electron energy modification, optical power in the newly resonant modes does not have to grow entirely from spontaneous emission. Figure 4-16 illustrates the progression in optical power $P(n)$ as the resonator loss per pass is decreased by increasing the quality factor over the range $Q = 20 \rightarrow 130$.

The electron beam energy is modulated with amplitude $A_o = 8\pi$ and with $N_o = 1000$ passes per oscillation. The simulation for each value of Q follows optical power $P(n)$ over $n = 4000$ passes. At $Q = 20$, resonator losses are large. The optical power only grows for electron bunching below $v = 0$, and the power profile is characteristic of giant power switching discussed earlier.

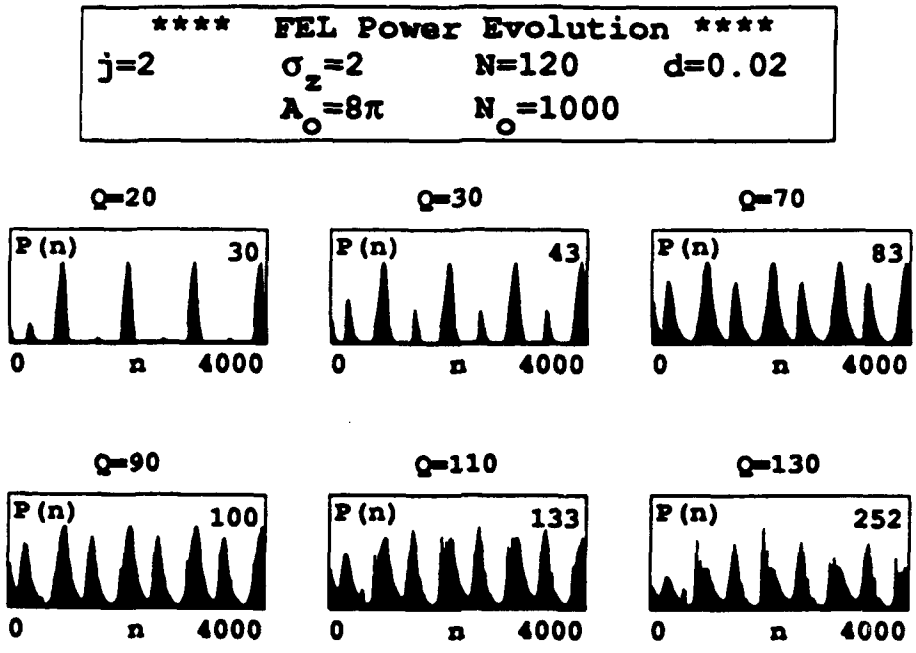

Figure 4-16. Progression in optical power $P(n)$ for decreasing resonator loss in a low gain FEL subject large amplitude electron beam modulation. Optical loss per pass is determined by $e^{-n/Q}$.

As Q increases, resonator losses decrease, and the power peaks corresponding to electron bunching above $v = 0$ begin to show. Peak optical power also grows with a decrease in resonator loss as expected. For low resonator loss Q>90, optical power for passes between the peaks becomes measurable.

Note, however, that the optical power peaks resulting from electron bunching at the modulation extremes retain their shape. Even for Q = 130, optical power at the peaks is substantially greater than the power between the peaks. Still, decreasing the resonator loss appears to help the optical field follow the resonant wavelength modulation.

I. OPTICAL PHASE PROGRESSION

Each short optical pulse that travels along the undulator is described by $a = |a|e^{i\phi}$, where $|a| = 4\pi NeKLE/\gamma^2 mc^2$ is the optical field amplitude and ϕ is the optical phase. The evolution of the optical field amplitude and phase is given by Equation (3.19). Recall that bunching of electrons near the phase $(\zeta + \phi) = \pi$ amplifies the optical wave amplitude, while electron bunching near $(\zeta + \phi) = \pi/2$ drives the optical wave phase. From Equation (3.13), the magnitude of the optical field vector potential can be written $A \propto \exp(ikz - i\omega t + i\phi)$. For fixed time $t = 0$, the change in the vector potential A with respect to longitudinal distance z is

$$\frac{dA}{dz} = i(k + d\phi/dz)A = ik'A \quad , \tag{4.3}$$

where the modified wavenumber is $k' = (k + d\phi/dz)$. When k' is inserted into the expression for dimensionless phase velocity, the result is

$$v = L[(k_o + k')\beta_z - k'] \quad . \tag{4.4}$$

After rearranging terms, (4.4) becomes

$$v = L[(k_o\beta_z - (k + d\phi/dz)(1 - \beta_z)] \quad . \tag{4.5}$$

Using the relation $L = N\lambda_o$, the resulting change away from the normal phase velocity v_o is

$$\Delta\nu = -N\lambda_o\frac{d\phi}{dz}(1-\beta_z) = -N\lambda\frac{d\phi}{dz} \quad , \tag{4.6}$$

where $\lambda_o \approx \lambda(1-\beta_z)$ near resonance. When the longitudinal distance is made dimensionless $z \rightarrow z/N\lambda$, the final form of (4.6) is

$$\Delta\nu = \nu(z) - \nu_o \approx -\frac{d\phi}{dz} \quad . \tag{4.7}$$

The slope in optical phase $\phi'(z) = d\phi/dz$ is therefore proportional to the change in the optical wavelength away from resonance ν_o [31].

In Figure 4-17, the output of a short pulse evolution simulation has been modified to show optical phase evolution $\phi(z, n)$ for a low gain $j = 1.5$ FEL with electron beam energy modulation amplitude $A_o = 3\pi$ and period $N_o = 3000$. The electron pulse length is $\sigma_z = 1.2$, and each pulse is injected ahead of the optical pulse with dimensionless desynchronism $d = 0.005$. The undulator contains $N = 120$ magnetic periods, and the optical losses per pass in the resonator are given by $Q = 30$. The optical pulse amplitude $|a(z, n)| = 25$ remains nearly constant throughout the simulation, so that changes in the optical power are small relative to the peak power of $P = 14$. The oscillation of the optical power is smooth and the power spectrum is centered about the phase velocity corresponding to peak gain for the optical field amplitude $a_o \approx 25$. As illustrated in Figure 4-18, the peak in optical gain is spread over the range of phase velocities $\nu \approx 4 \rightarrow 8$. The curve in Figure 4-18 shifts back and forth along the ν-axis as the resonant wavelength changes. The resonance condition (3.2) forces resonant wavelength to change when the electron beam energy is modified.

There are four peaks in optical power $P(n)$ in Figure 4-17, each corresponding to an extreme in electron beam energy modulation. Between the two center peaks, the electron energy is increasing and the optical spectrum $P(\nu(\lambda), n)$ is shifting toward decreasing values of phase velocity. This implies that the resonant wavelength is

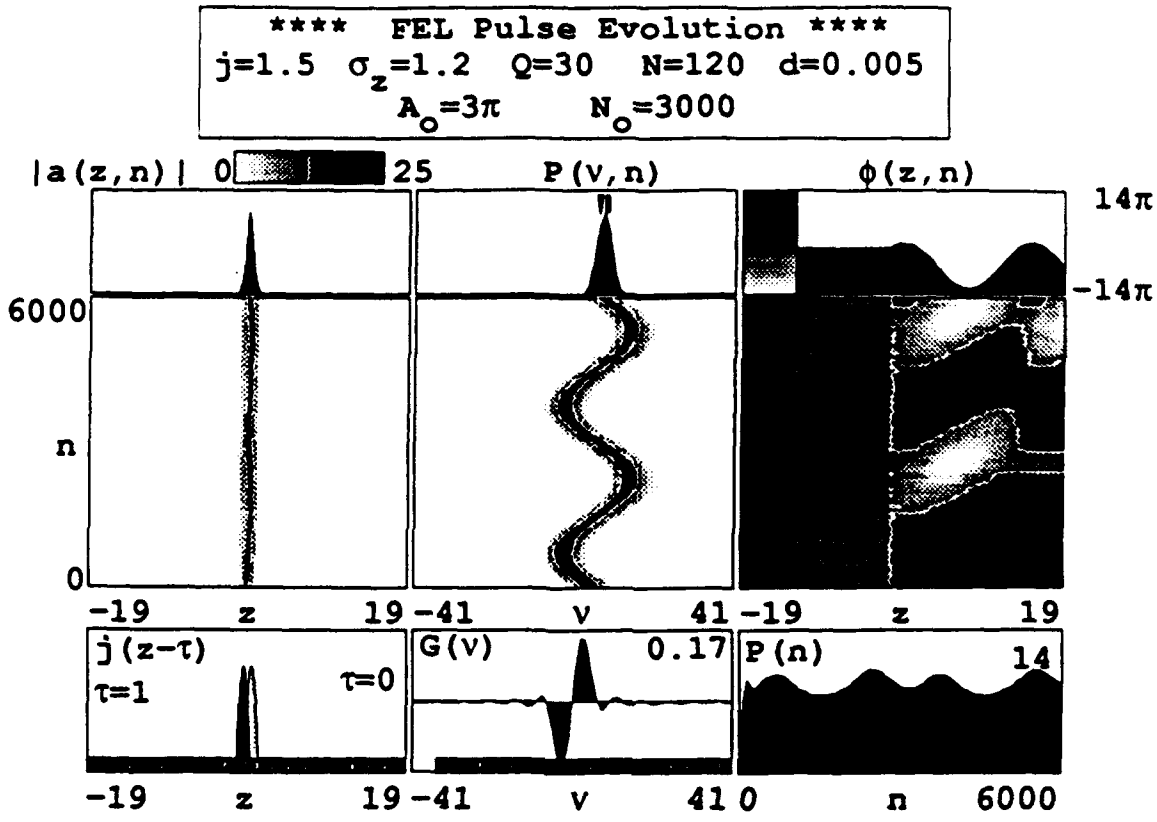

Figure 4-17. Modified pulse evolution simulation showing the progression of optical phase $\phi(z, n)$ for a low gain FEL with moderate electron beam energy modulation.

shifting toward shorter wavelengths. Since the FEL shifts toward shorter wavelengths easier than toward longer wavelengths, the optical power between the two center power peaks in $P(n)$ is slightly greater in magnitude than that in the vicinity of the outer peaks.

The final phase profile is shown at the top in $\phi(z, n)$. It is scaled to the maximum and minimum phase attained during the simulation. The grey scale to the left helps to identify phase amplitudes in the contour plot of $\phi(z, n)$ below. Outside the electron pulse located at the center of the window, the optical phase does not evolve. To the left of the electron pulse, the optical pulse remains at its initial value

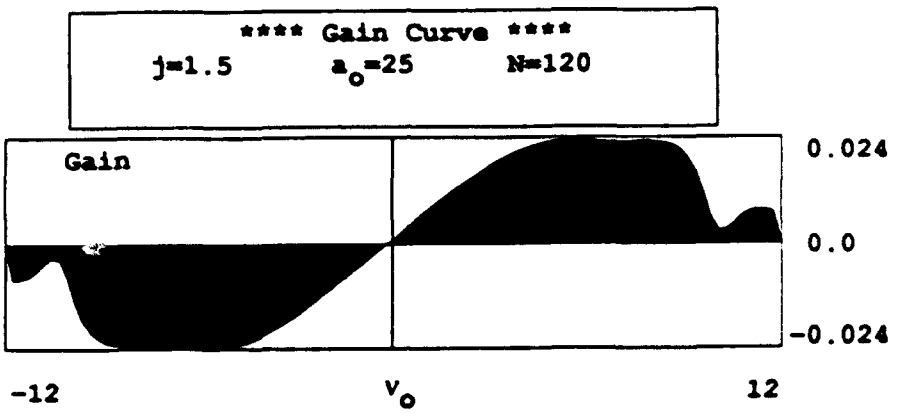

Figure 4-18. Strong-field gain spectrum $G(\nu_o)$ for low current j = 1.5 FEL.

of $\phi = 0$. At the center of the window, the optical phase is at the value necessary to shift the optical pulse to resonance as determined by the modulated electron beam. On the right of the window, the optical pulse is no longer interacting with the electron pulse and shifts right each pass through desynchronism. Actual phase amplitudes in $\phi(z, n)$ show a running history of the slope of phase over many passes. The electron energy modulation given by (4.1) is sinusoidal. Since the slope in the optical phase is related to the change in electron phase velocity in (4.7), the behavior of optical phase is characterized by

$$\frac{d\phi}{dz} = - A_o \sin\left[\frac{2\pi n}{N_o}\right] . \tag{4.8}$$

Equation (4.8), together with the relation for shifting by desynchronism along the longitudinal distance, $z = nd$, are used to derive the peak-to-peak amplitude of optical phase along z

$$\Delta\phi_{max} = \frac{dA_o N_o}{\pi} \quad . \tag{4.9}$$

Figure 4-19 provides a series of snapshots of the optical phase profile along the z-axis for the range of passes $n = 3000 \rightarrow 6000$. The peak-to-peak amplitude in phase $\Delta\phi_{max} = 14\pi$ remains constant throughout the simulation, but shifts up and down according to the slope at the beginning of the interaction between the optical wave and the electron pulse. The maximum and minimum optical phases are reached for electron bunching at the extremes of modulation. Optical power $P(n)$ grows to its peak value at these extremes, and decreases at all other times.

The maximum phase is attained when electrons bunch above $v = 0$. The resulting optical spectrum is on the short wavelength side of modulation. The minimum phase occurs when electrons bunch below $v = 0$, so the optical spectrum is on the long wavelength side of modulation. The phase slope at the interaction point in the center indicates the direction of wavelength movement. When the phase slope is negative, the optical spectrum is shifting toward longer wavelengths. When the phase slope is positive, the optical spectrum is shifting toward shorter wavelengths. The changes of the optical spectrum $P(v, n)$ in response to resonant electron energy modulation are thus revealed by the evolution of the optical phase $\phi(z, n)$.

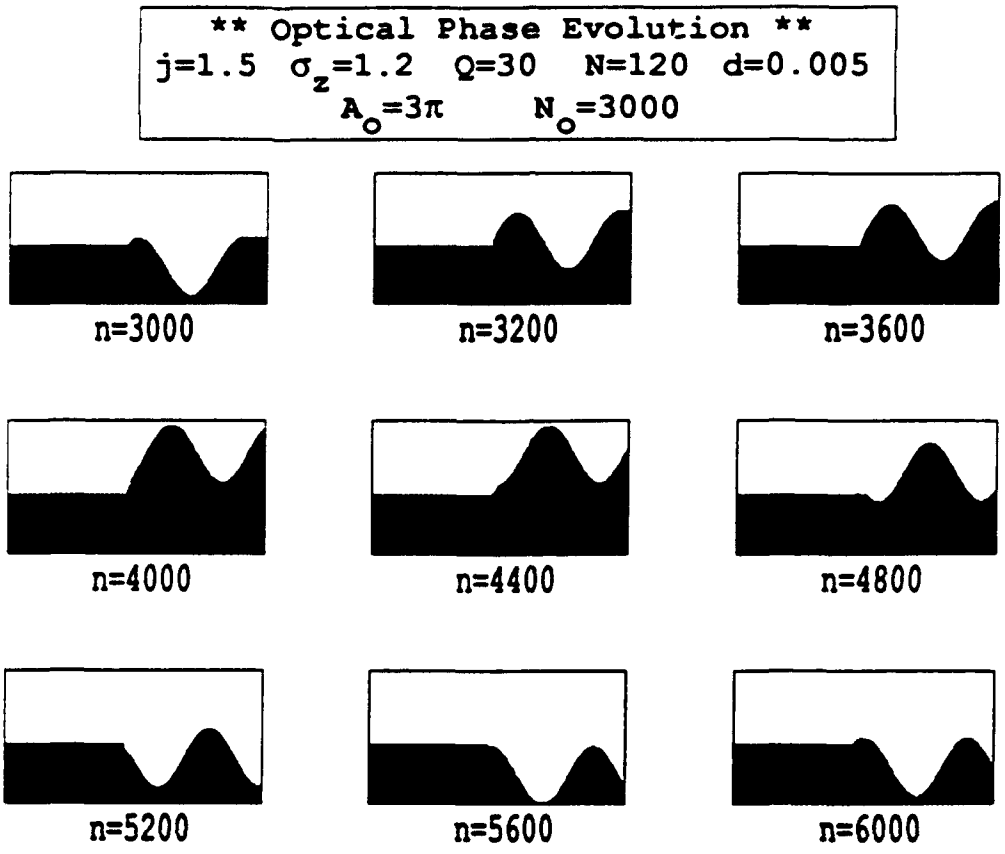

Figure 4-19. Optical phase evolution for low gain FEL subject to sinusoidal electron beam energy modulation.

V. WAVELENGTH STABILIZATION THEORY

A. INTRODUCTION

Design flexibility and choice of output wavelength are two of the most exciting advantages of the FEL over conventional lasers. The reliability of the technology used in design is such that an FEL may be used as a research tool, operating for long periods of time to supply light at of a wide range of wavelengths to users conducting experiments [2]. But the effectiveness of an FEL as a user facility is dependent on the stability of the power and wavelength of the light received by the user. Even though continuous tunability is normally considered to be an asset, the FEL system is complex and can be subject to undesired drifts in optical wavelength due to shifting in the parameters inherent in the resonance condition (3.2).

The Stanford University Superconducting Accelerator (SCA) Free Electron Laser (FEL) Facility is configured as an oscillator with a mirror separation of $S = 12.68$ meters. The magnetic field in the undulator is produced by stationary magnets forming $N = 120$ periods. The laser is driven by electron micropulses approximately 3 picoseconds long with an 85 nanosecond interval between micropulses. Nearly 120,000 micropulses are emitted within a single macropulse approximately 10 milliseconds long. Consecutive macropulses are separated by about 100 milliseconds. The average macropulse current in the electron beam is $I = 100$ microamps, with the corresponding energy adjustable to produce optical wavelengths in the range of $\lambda = 0.5 \rightarrow 5.0$ μm. [33,34]

In the Stanford SCA/FEL Facility, the optical wavelength around $\lambda \approx 4$ μm is observed to fluctuate randomly. The magnitude of fluctuation can be a fraction of a

percent over times less than a millisecond. Many experiments conducted at the Facility require that shifts in frequency be held to within a few parts in 10^4 at all times [35]. At the Stanford SCA/FEL, the optical wavelength is stabilized by measuring the deviation from the wavelength desired by the user, and proportionally adjusting the electron energy to correct the deviation [35]. Note that conventional atomic lasers may also have problems with output wavelength stability. However, this kind of control would not be possible in a conventional laser because the basic emission characteristics of the atom or the molecule are beyond the control of the experimenter.

B. MODULATION TRENDS

If the resonant electron energy is varied slowly over many passes, the optical pulse in the FEL is likely to follow with sufficient power. The rate at which the optical pulse is able to follow a given change affects the speed of the wavelength control system to be used. The performance of the wavelength control system is optimized by understanding the response of the FEL to variation of the resonant wavelength over decreasing time scales. In simulation, this is accomplished by observing the steady-state response to a sinusoidal variation in resonant electron phase velocity described by Equation (4.1). As shown in Figure 5-1 and Figure 5-2, both amplitude A_o and period N_o play a role in optical wavelength modulation.

In Figure 5-1, the power evolution $P(n)$ is shown for a low gain FEL oscillator in which the amplitude is varied over the range $A_o = 0.3\pi \rightarrow 8\pi$. This corresponds to a wavelength variation of $\Delta\lambda/\lambda \approx A_o/2\pi N \approx 10^{-3} \rightarrow 0.03$ for Stanford. The period of modulation is $N_o = 1000$ passes per oscillation, or ≈ 0.1 milliseconds. All other parameters are held constant and are the same as simulations used earlier. For a small amplitude $A_o \leq 0.3\pi$, the optical wavelength easily follows the modulated electron beam, and optical power $P(n)$ oscillation is minimal. As the amplitude is increased to

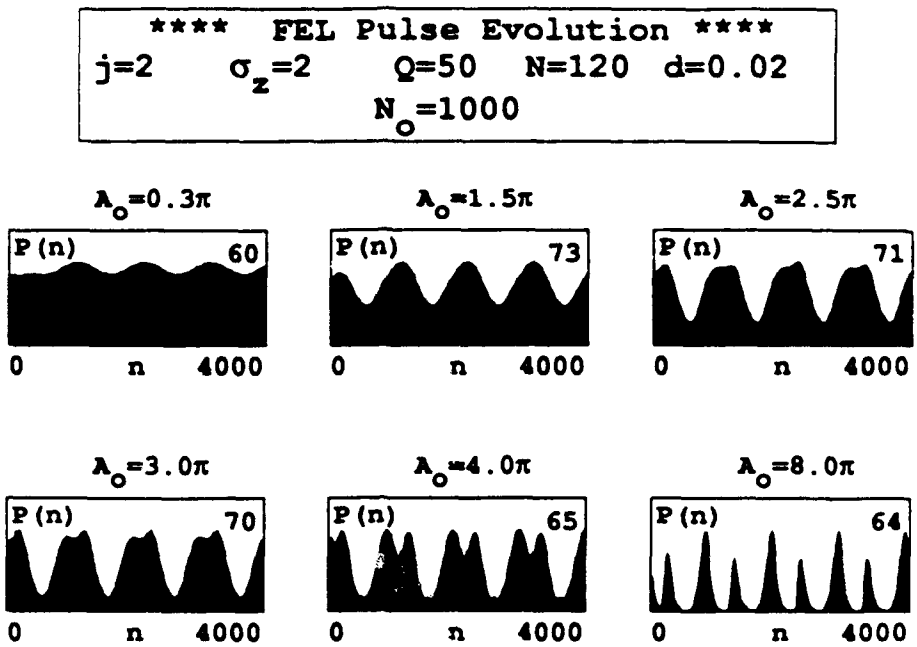

Figure 5-1 Progression in optical power $P(n)$ for a low gain FEL as the amplitude of electron energy modulation A_o is increased with frequency of modulation held constant.

$A_o = 1.5\pi$, the magnitude of optical power variation becomes substantial, but oscillates smoothly throughout the simulation. Above $A_o = 2.5\pi$, a small dip in power at each peak becomes distinguishable. Recall that the FEL preferentially the follows resonant wavelength shifts from longer to shorter wavelengths since the bunched electrons tend to stay in resonance for a longer time. The small dips in power correspond to these preferential shifts. The large decreases in power correspond to shifts in the resonant wavelength from shorter to longer wavelengths because the bunched electrons tend to fall out of resonance faster. At $A_o = 4\pi$, the power peaks resulting from electron bunching at either extreme in modulation are clearly visible. For large amplitude modulation $A_o \geq 8\pi$, the peaks corresponding to electron bunching above $v = 0$ in phase space begin to die out. The electron energy slew rate at these amplitudes is so

large that shifts in wavelength are not followed. Optical power of appreciable magnitude is only obtained during periods of maximum electron bunching.

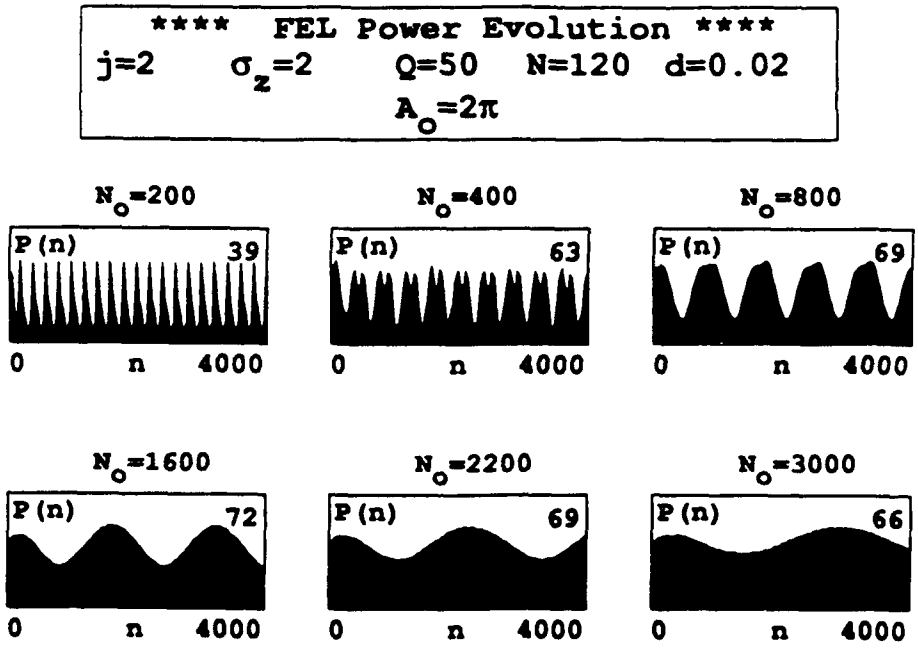

Figure 5-2 Progression in optical power $P(n)$ for a low gain FEL as the period of electron energy modulation N_o is decreased with amplitude of modulation held constant.

Figure 5-2 displays the power evolution $P(n)$ for modulation at an amplitude of $A_o = 2\pi$ over the range of periods from $N_o = 200 \rightarrow 3000$ passes per oscillation. At high frequency modulation of $N_o \leq 200$, peaks in optical power corresponding to bunching at modulation extremes are observed, with significant power loss between each peak. Decreasing the frequency of modulation decreases the rate of electron energy shift in either direction. At $N_o = 400$, the power peaks resulting from maximum electron bunching are still observed, but power begins to fill the space between peaks when the resonant wavelength shifts from longer to shorter wavelengths. This again shows the preferential nature of such a shift. Above $N_o = 800$, the separate peaks

become indistinguishable, and the optical power $P(n)$ begins to oscillate smoothly at the frequency of the electron energy modulation. Note that the peak power remains near the same order of magnitude $P \approx 67$ until the electron energy is modulated with a high frequency of $N_o \leq 200$. Then, the maximum power decreases significantly, indicating a possible roll-off in the response of the FEL at high frequency modulation.

C. DISCRETE TRANSFER FUNCTION

The FEL transfer function is a measure of the amplitude and phase response of the optical pulse as a result of electron beam energy variation. The fractional change in the optical wavelength determined from the resonance condition (3.2) is $\Delta\lambda/\lambda = -2\Delta\gamma/\gamma$ for for a small incremental change $\Delta\gamma mc^2$ in electron energy. If it is also assumed that the overall response of the FEL to continuous resonant shifts in wavelength is dependent on the modulation frequency $f = c/2SN_o$, then the FEL transfer function $H(f)$ is characterized by

$$\frac{\Delta\lambda}{\Delta\gamma} \propto -\frac{2\lambda}{\gamma} H(f) \ . \tag{5.1}$$

So the magnitude of the transfer function at a particular frequency determines the peak-to-peak amplitude of the variation in output wavelength for a given variation in electron energy. If $H(f) \rightarrow 0$ then the optical wavelength will not follow resonant electron energy movement. If $H(f) \rightarrow 1$ then the optical wavelength will readily follow an energy shift.

An estimate of the amplitude response of the FEL can be obtained by measuring the magnitude of the variation of the optical wavelength and comparing it to the magnitude of the input electron energy variation over a discrete number of modulation frequencies. The range of modulation frequencies selected is $f \approx 10^3 \rightarrow 10^6$ Hz, corresponding to a range of periods $N_o = 10{,}000 \rightarrow 10$ passes per oscillation. At the

selected frequencies, short-pulse simulations are run for at least ten full periods of electron energy modulation. One simulation is shown in Figure 5-3.

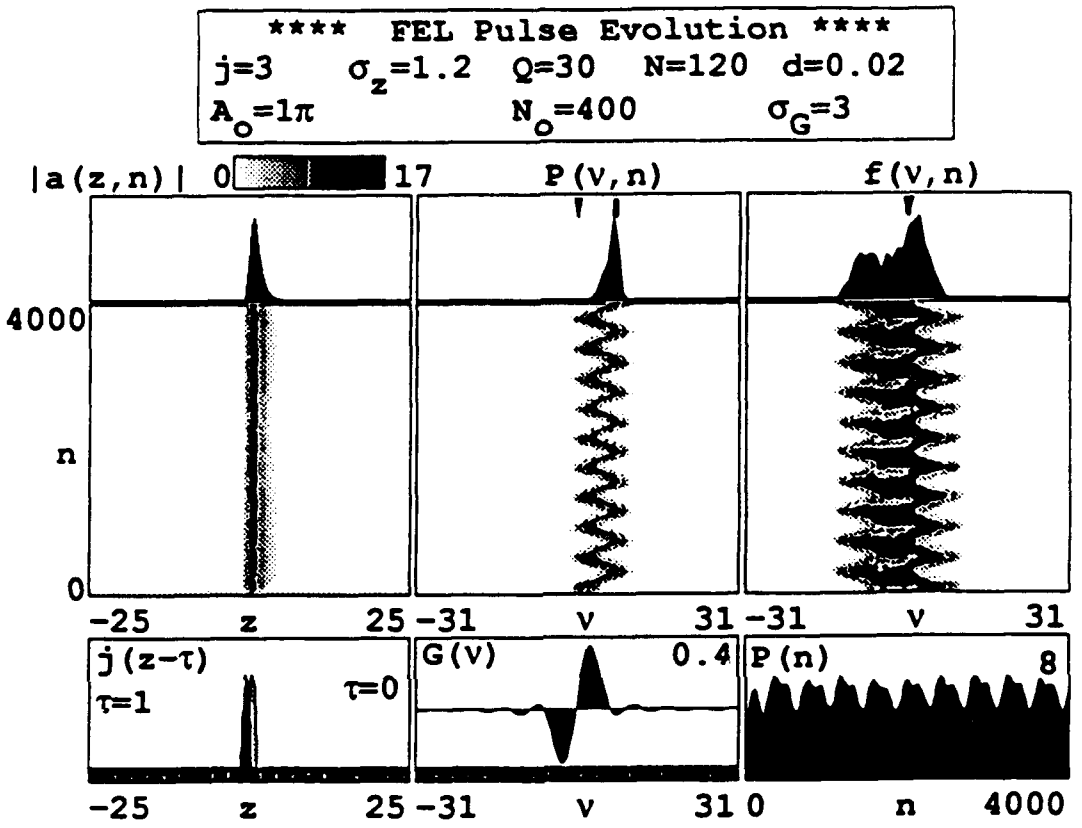

Figure 5-3 Example of short pulse evolution simulation used to prepare a discrete FEL transfer function. Optical wavelength variation is observed in $P(\nu(\lambda), n)$ and electron energy modulation is observed in $f(\nu(\gamma), n)$.

For each simulation the electron beam current is taken to be $j = 3$ with an input energy spread described by $\sigma_G = 3$. Recall from Figure 3-5 that increasing the electron energy spread causes the overall gain spectrum to broaden in phase velocity ν, at the expense of a decrease in peak gain. The electron pulse length is $\sigma_z = 1.2$, and each pulse is injected with dimensionless desynchronism $d = 0.02$. The undulator consists of $N = 120$ magnetic periods.

The amplitude of modulation is $A_o = \pi$ for all frequencies simulated. At each pass in a particular simulation, the phase velocity with maximum optical power in the optical spectrum $P(v(\lambda), n)$ is extracted to observe modulation in resonant wavelength. After steady-state oscillation is achieved, the peak-to-peak wavelength modulation distance is measured in units of dimensionless phase velocity v. This is compared to the known peak-to-peak electron energy modulation distance in $f(v(\gamma), n)$, also measured in dimensionless phase velocity v. The resulting ratio gives a measure of $\Delta\lambda/\Delta\gamma$, which is plotted with respect to frequency f as a single point in the discrete transfer function magnitude graph. Curves for resonator loss quality factors $Q = 30$ and $Q = 100$ are shown in Figure 5-4.

For low frequency electron energy modulation $f \leq 10$ kHz, the resonant wavelength follows with maximum amplitude. Above $f = 10$ kHz, both curves experience a roll-off in magnitude. The degree of roll-off is measured in decibels per decade of frequency increase (dB/decade). A decibel is defined

$$\text{dB} = 20 \log_{10}\left[\frac{A_\lambda}{A_\gamma}\right] , \tag{5.2}$$

where A_λ and A_γ are the peak-to-peak amplitudes of the resonant wavelength modulation and the electron energy modulation, respectively. For $Q = 30$ the initial roll-off is ≈ -6 dB/decade, and for $Q = 100$ the roll-off is ≈ -12 dB/decade. The steepest degree of roll-off for both curves occurs at frequencies beyond $f \geq 60$ kHz. The $Q = 30$ transfer function falls ≈ -60 dB/decade, and the rate of decrease for $Q = 100$ is ≈ -80 dB/decade. The shapes of both curves are similar, but the transfer function for $Q = 100$ falls off more rapidly than that of $Q = 30$. This indicates that decreasing loss in the optical resonator hampers the ability of the FEL to follow resonant wavelength at higher frequencies. It appears that an FEL oscillator with

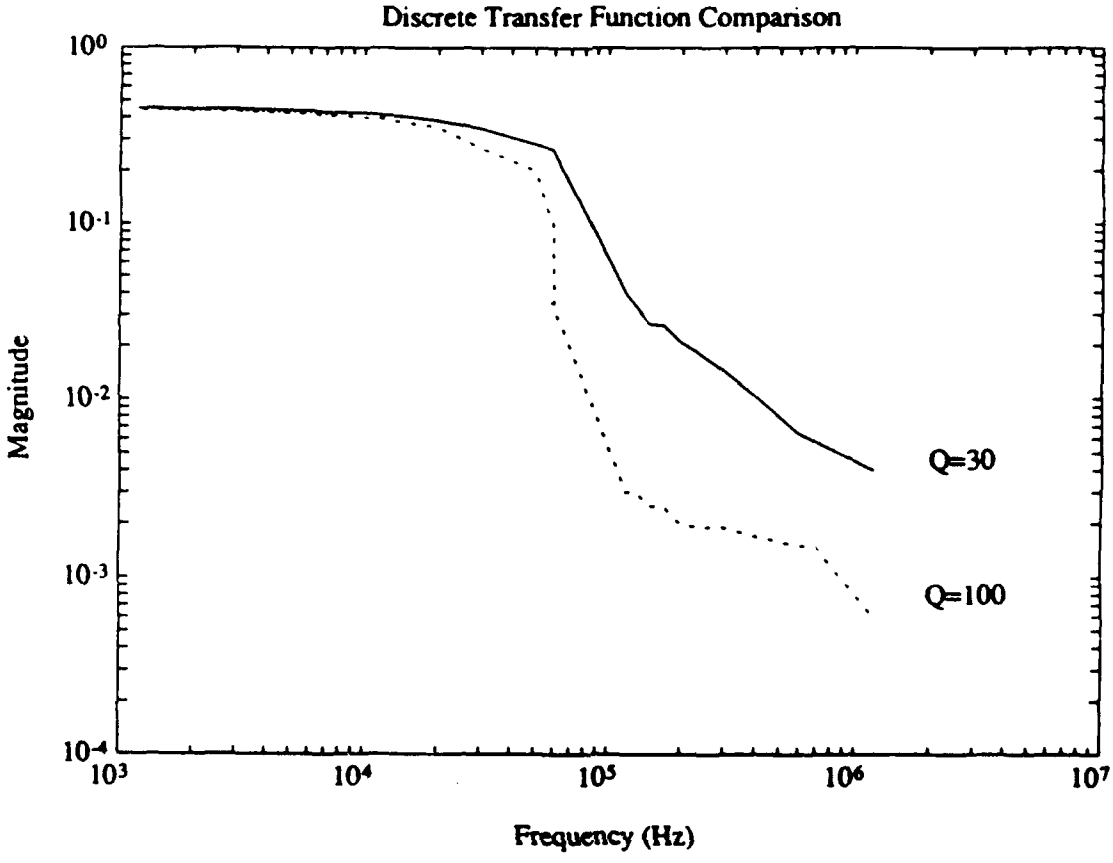

Figure 5-4. Discrete amplitude response of the transfer function $H(f)$ for a short pulse, low-gain FEL for two different values of the loss term Q.

lower resonator loss tends to resist fast resonant wavelength motion to new optical modes, because it "remembers" optical power at the previous mode for a longer period of time.

D. LINEAR FEEDBACK THEORY

In the previous analysis, the discrete transfer function curves provided only amplitude information. The phase relationship of the FEL transfer function is not easy to determine in such a way. More detail is obtained by applying Linear Time-

Invariant (LTI) feedback theory. The causality condition of LTI theory assumes that a given output sequence $y(n)$ is formed by the convolution of some linear transfer function h with an input sequence x, so that after discrete time $n > 0$

$$y(n) = \sum_{m=0}^{\infty} h(m)x(n-m) \quad . \tag{5.3}$$

To convert the sequence (5.3) into the frequency domain, the Fourier transform $F\{\cdots\}$ is applied to both sides,

$$F\{y(n)\} = \sum_{m=0}^{\infty} h(m)F\{x(n-m)\} \quad . \tag{5.4}$$

But a property of the Fourier transform is that

$$F\{x(n-m)\} = e^{-i2\pi fm}\, F\{x(n)\} \quad , \tag{5.5}$$

which when substituted into (5.4), gives the output function in the frequency domain,

$$Y(f) = F\{y(n)\} = \sum_{m=0}^{\infty} h(m)\, e^{-i2\pi fm} X(f) \quad , \tag{5.6}$$

where $X(f) = F\{x(n)\}$. Divide both sides of (5.6) by $X(f)$ to obtain the transfer function in the frequency domain $H(f)$,

$$\frac{Y(f)}{X(f)} = \sum_{m=0}^{\infty} h(m)\, e^{-i2\pi fm} = F\{h(m)\} = H(f) \quad . \tag{5.7}$$

The linear transfer function operator, $H(f)$, is often displayed as an amplitude and phase angle plot as a function of the frequency f. [36]

E. CONTINUOUS TRANSFER FUNCTION

The response of the FEL to a continuous range of electron energy modulation frequencies can be simulated using the following function for the input resonant electron phase velocity:

$$\nu(n) = \nu_o + A_o \sin\left[\frac{2\pi n}{N_{max}\left[\frac{N_{FM} - n}{N_{FM}}\right]}\right], \tag{5.8}$$

where N_{max} is the longest electron energy modulation period desired, and N_{FM} is the total number of passes to be simulated. When the pass number is small $n \ll N_{FM}$, then $\nu \approx \nu_o + A_o \sin(2\pi n / N_{max})$ and the resonant electron energy modulates with period near N_{max}. As n increases, the frequency of modulation increases. When $n \approx N_{FM}$, the frequency of modulation approaches infinity. However, the modulation period is tested separately in the program so that only values in the range $N_o \approx N_{max} \rightarrow 10$ passes per oscillation are allowed.

Figure 5-5 shows the result of simulation in a low-gain FEL with $N_{max} = 10{,}000$ over $N_{FM} = 30{,}000$ total passes. The effective range of modulation periods is $N_o \approx 10{,}000 \rightarrow 10$ passes per oscillation. The electron beam current is $j = 1.5$ with a pulse length $\sigma_z = 1.2$, providing about 20 percent gain in the weak-field regime. The optical power $P(n)$ follows the increase in modulation until very high frequencies are reached. Then, power cuts off completely. Peak optical power is $P = 26$, and although it oscillates, $P(n)$ remains about the same magnitude until the cut-off.

The same method is applied to the FEL input data used to compile the discrete transfer function $H(f)$, for $Q = 30$, in Figure 5-4. The resonant wavelength phase velocity is extracted from $P(\nu(\lambda), n)$ at each pass and plotted with the resonant electron energy phase velocity from $f(\nu(\gamma), n)$. Figure 5-6 displays the result. Using

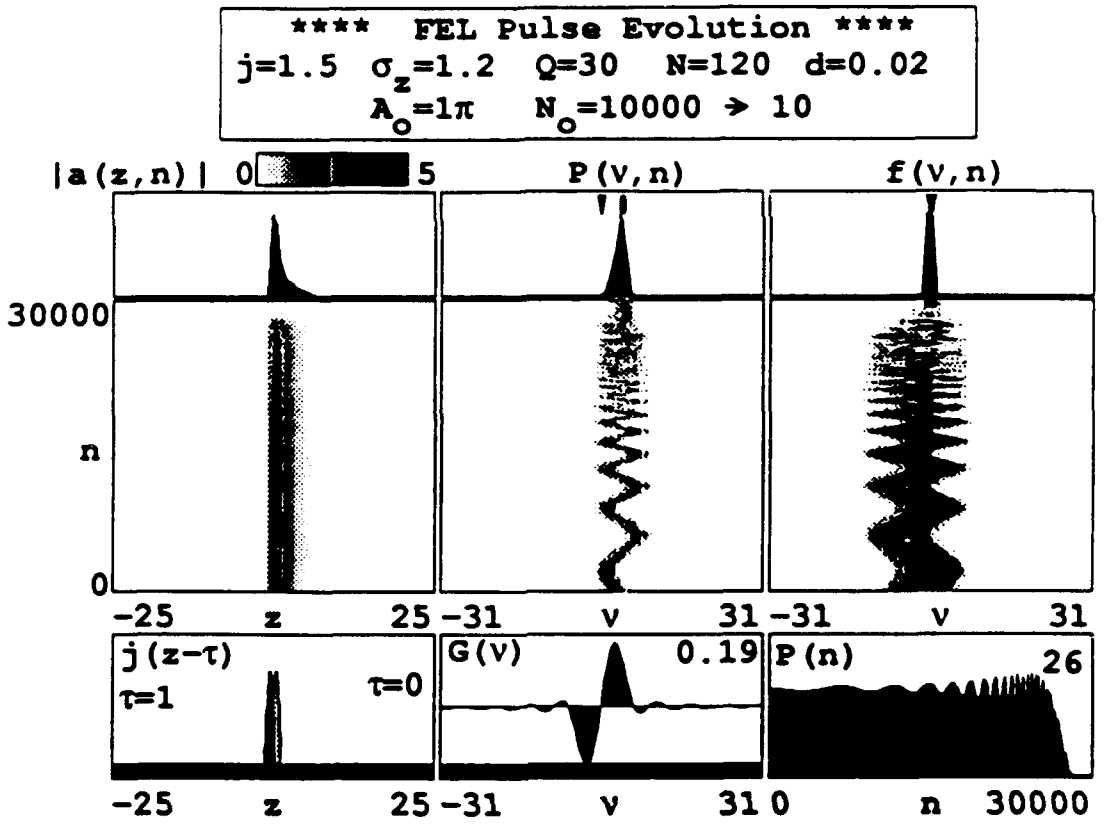

Figure 5-5. Short pulse evolution for low gain FEL illustrating frequency modulation in electron energy input.

the Stanford FEL parameters, each pass n is 85 nanoseconds long. The simulation runs for n = 30,000 passes, equivalent to approximately 2.5 milliseconds real time. The increase in electron energy modulation is shown at the top. The effective range of periods is $N_o \approx 10{,}000 \rightarrow 10$ passes per oscillation, corresponding to modulation frequencies in the range $f \approx 10^3 \rightarrow 10^6$ Hz. The amplitude of electron modulation, $A_o = \pi$, remains the same throughout the simulation. The resonant wavelength information is plotted at the bottom. The amplitude of wavelength oscillation decreases significantly at high frequencies, indicating that the FEL behaves like a low-pass filter for optical wavelength control through resonant electron energy modulation.

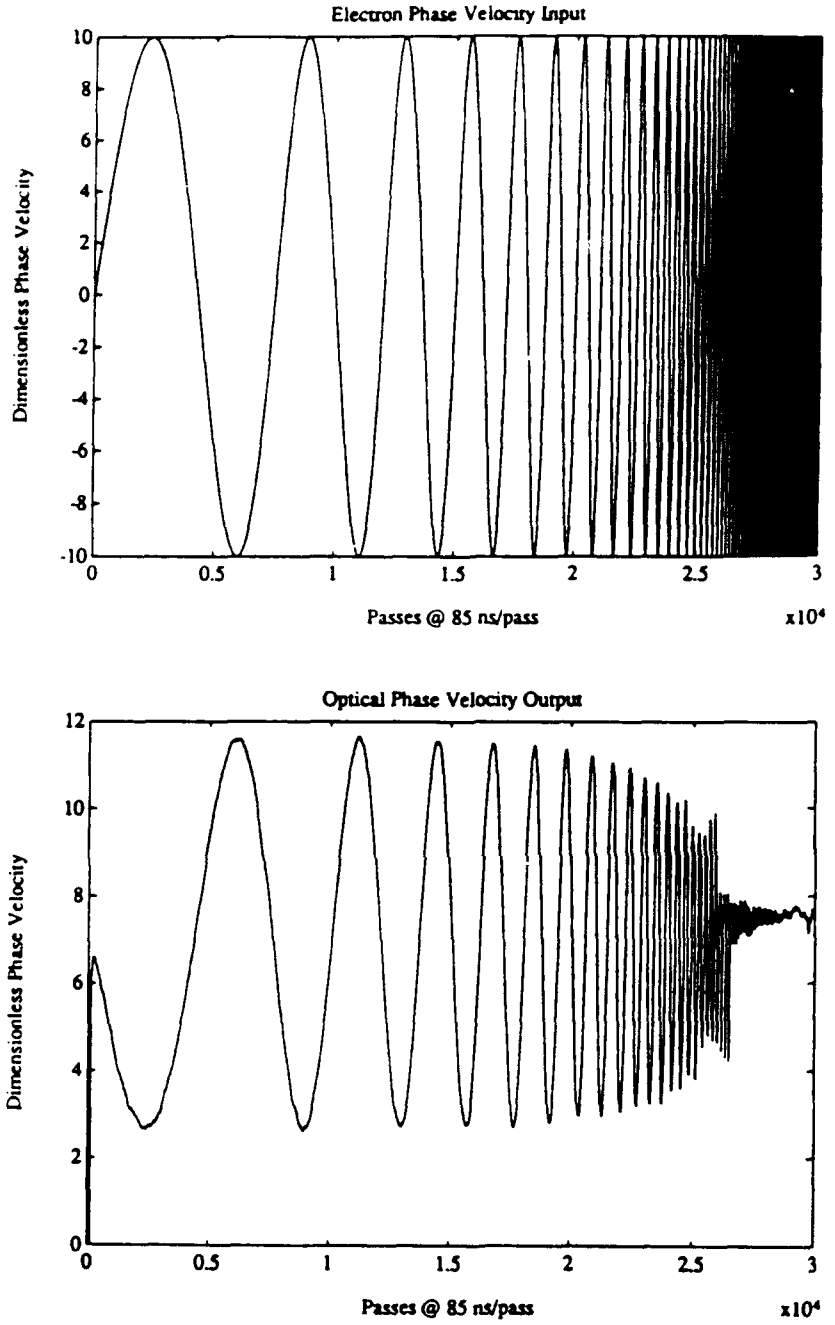

Figure 5-6. Resonant optical wavelength phase velocity and resonant electron energy phase velocity for frequency modulated input electron energy in a short pulse FEL with Q = 30.

Before equation (5.7) is applied to the input and output functions to obtain the continuous FEL transfer function $H(f)$ response, the Welch method of power spectrum estimation is used [38]. The purpose of the method is to make the result less susceptible to noise at the beginning and at the end of the frequency range due to truncation errors of the Fast Fourier Transform (FFT) [37]. The input and output signals are divided into consecutive sections of M-point sequences. Then, a Hanning window is applied to each section by FFT convolution. The Hanning window uses a method of statistical weighting to decrease the importance of the beginning and end of each M-point section. The effect is to force the ends of a section to approach the same amplitude value, thereby reducing sidelobes of the spectral output when the FFT is performed. [36,38]

Next, the windowed M-point sections are accumulated, and (5.7) is applied. The resulting transfer function $H(f)$ is complex. The real part is plotted as the amplitude response, and the imaginary part is plotted as phase response. Figure 5-7 displays the result for the input and output shown in Figure 5-6, with an FFT sampling size $M = 1024$ points.

The amplitude response is shown at the top. It demonstrates the same characteristics as the discrete transfer function shown in Figure 5-4, but the roll-off is slightly smoother. A series of spikes occur near $f \approx 2 \times 10^5$ and $f \approx 5 \times 10^5$ Hz. These are assumed to be noise resulting from the choice of the FFT sampling size M. To further investigate, figure 5-8 shows the transfer function amplitude response for three different FFT point sizes with all other variables held constant. Note that the overall shape of the transfer function remains the same for frequencies of interest $f \leq 4 \times 10^5$ Hz. The spikes at the end of the curves grow substantially as M is increased, so FFT sampling noise must be the cause. The curve with $M = 1024$ points per FFT seems to provide the best information in the region desired.

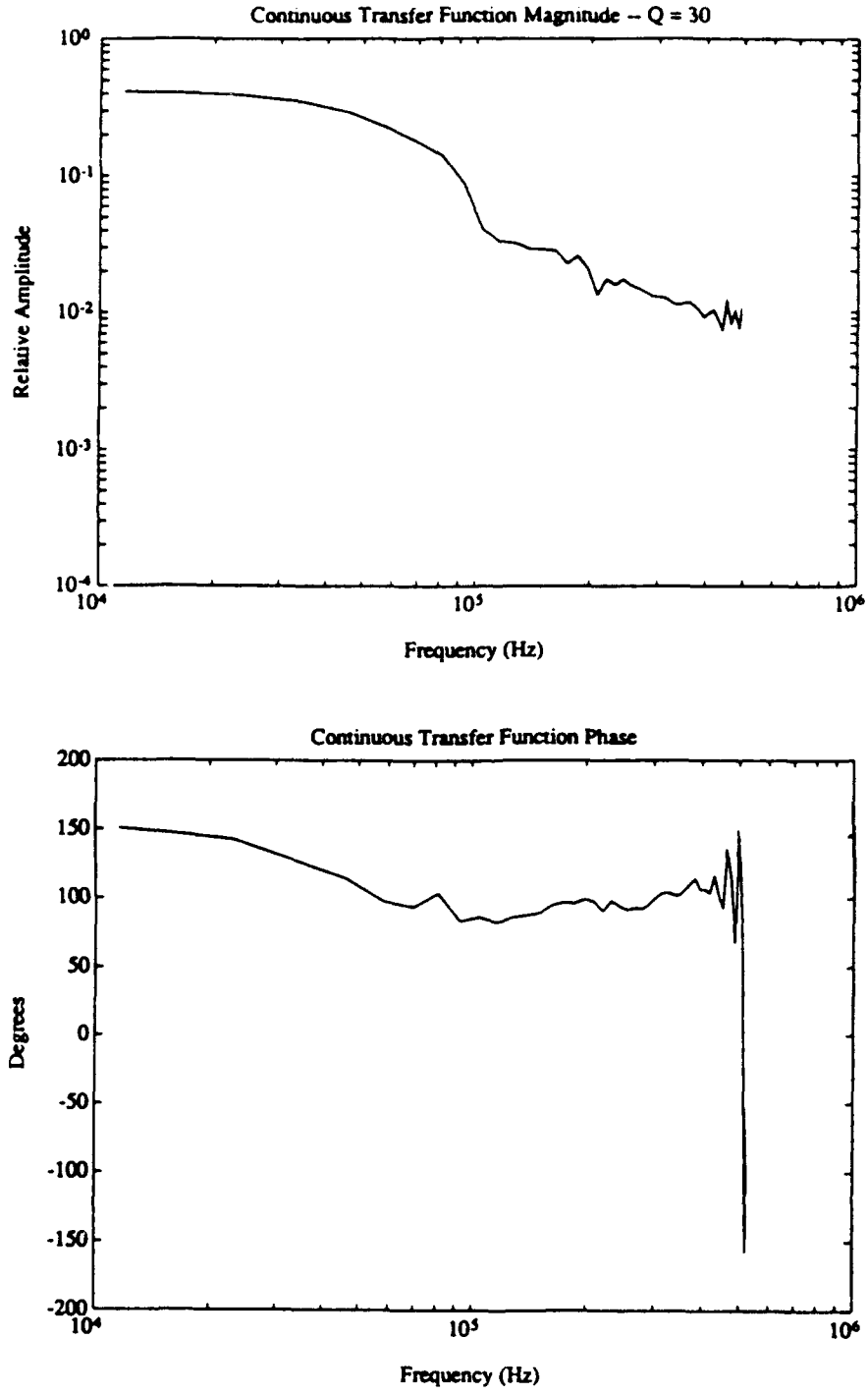

Figure 5-7. Amplitude and phase response of the continuous transfer function $H(f)$ for low gain FEL with $Q = 30$.

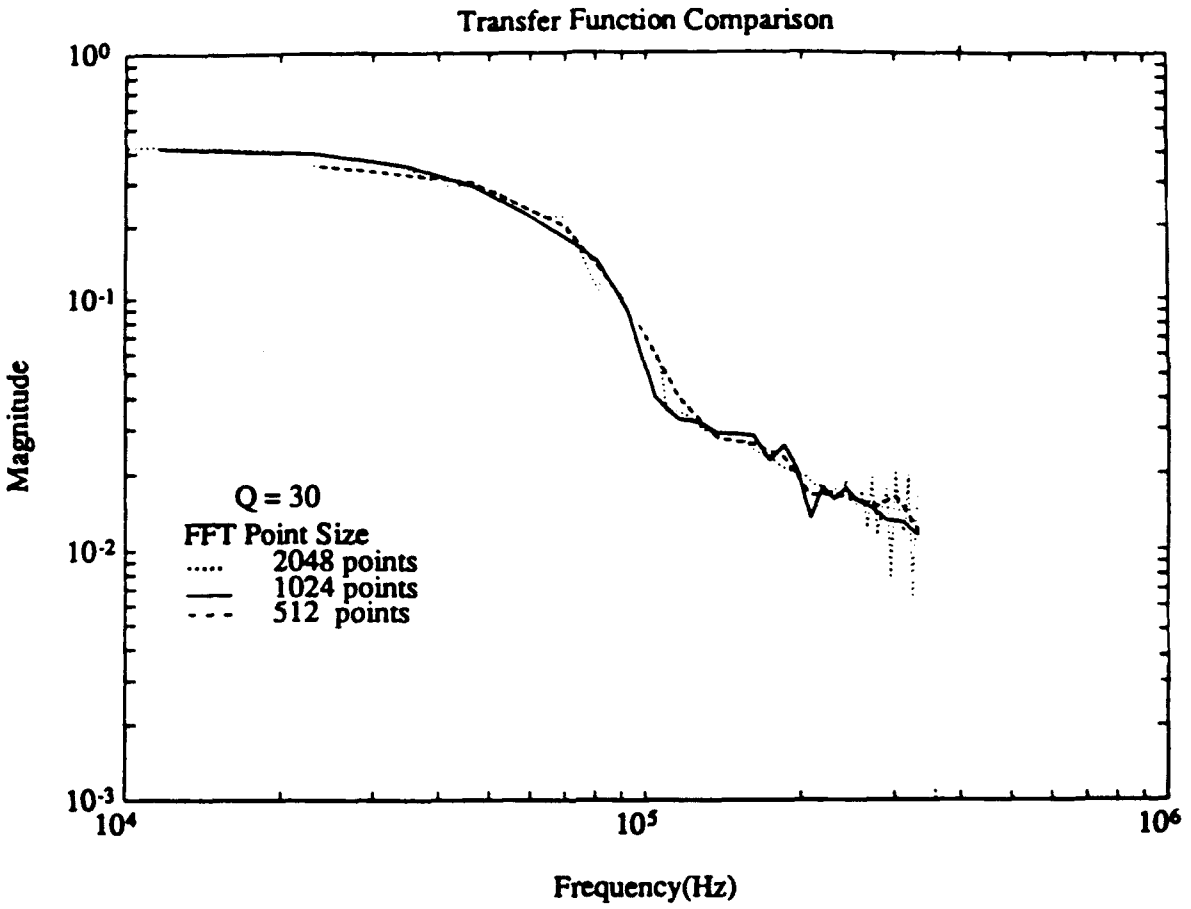

Figure 5-8. Transfer function comparison for low gain FEL. Each curve represents the result obtained for a different FFT point size with all other variables held constant.

The bottom of Figure 5-7 shows the phase response of the continuous transfer function $H(f)$. Below $f < 10$ kHz, the phase response is relatively flat. Above this value, the phase response begins to drop. Then, a transition occurs at $f \approx 10^5$ Hz, and the phase begins begins to increase. The transition point corresponds to the region of maximum drop-off in the amplitude response curve above. Near $f \approx 5 \times 10^5$ Hz the phase becomes chaotic and actually experiences a complete shift from $\approx +150$ degrees to ≈ -150 degrees.

The input signal for initial electron energy phase velocity, generated by (5.8), provides a linear increase in modulation frequency. The length of the signal is determined by N_{FM}. The dependence of the output wavelength transfer function $H(f)$ on the length of the signal N_{FM} is shown in Figure 5-9. Three different frequency-modulated short pulse evolution simulations are performed for $N_{FM} = 20{,}000$, $N_{FM} = 30{,}000$, and $N_{FM} = 40{,}000$ passes. The maximum period is held constant at $N_{max} = 10{,}000$ passes per oscillation. Resonator losses are given by $Q = 30$. All other FEL input parameters remain the same.

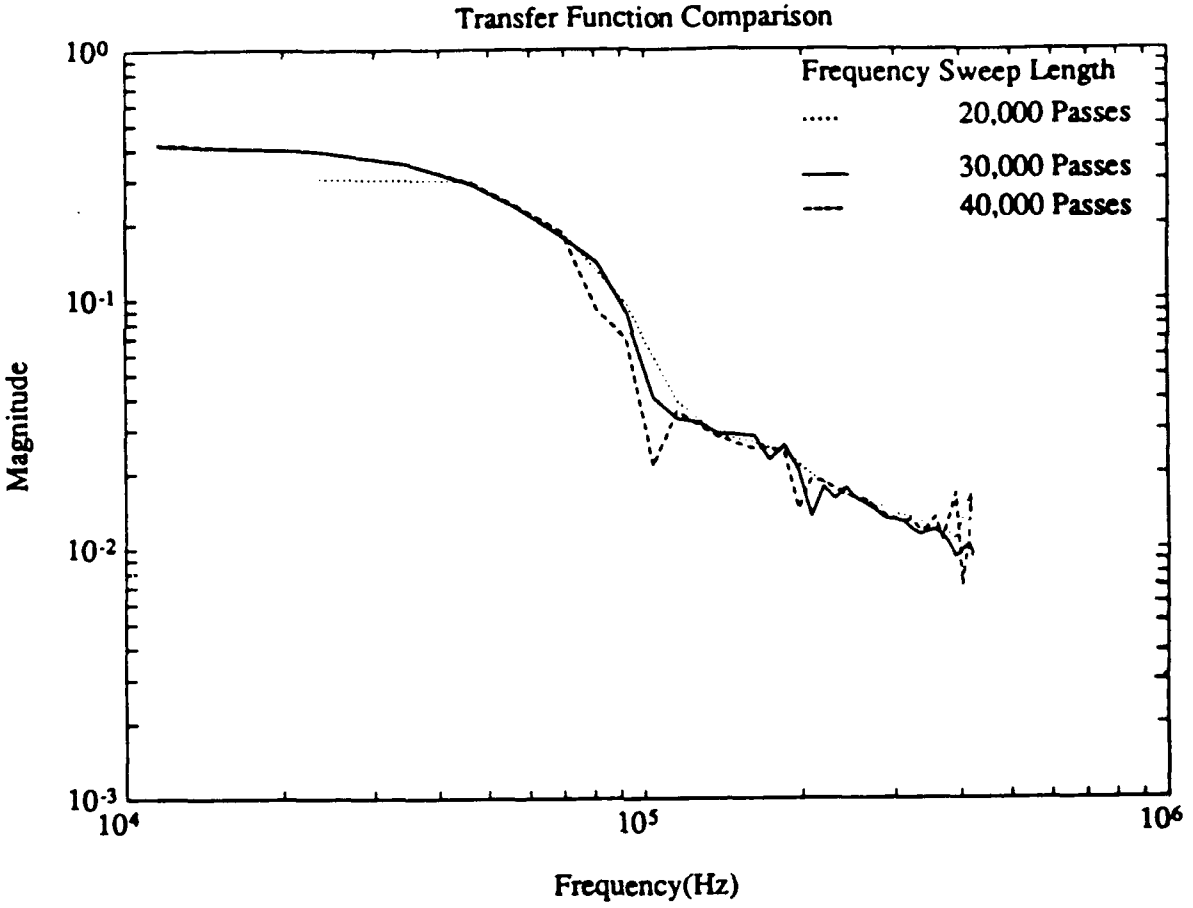

Figure 5-9. Continuous transfer function $H(f)$ comparison for low gain FEL with $Q = 30$ illustrating the effect of varying the modulation signal length N_{FM}.

As the modulation signal increases in length N_{FM}, more time is spent in passes n at each value of frequency f, so the resolution of the transfer function $H(f)$ should improve. However, lengthening the signal can cause the program to become costly in terms of time required to compute the result. As shown in Figure 5-9, all the transfer function curves display the same general behavior for frequencies of interest $f \leq 4 \times 10^5$ Hz. Therefore, the result is relatively insensitive to the choice of modulation signal length in this region. A modulation signal length $N_{FM} = 30{,}000$ passes provides a reasonable compromise between transfer function accuracy and length of computing time.

The benefit of using a frequency-modulated electron energy input is the relative ease in which the transfer function is obtained. The discrete transfer functions shown in Figure 5-4, require completion of many short-pulse evolution simulations. Each simulation provides response information for only one frequency. With the continuous transfer function method, a single short-pulse evolution is run with a frequency-modulated signal. This way, other FEL input parameters are easier to change in order to observe trends in the behavior of the transfer function.

For example, Figure 5-10 shows the input electron energy phase velocity and optical output phase velocity plots for an FEL with the quality factor increased to $Q = 100$. The amplitude of modulation is still $A_o = \pi$, and the input modulation frequency ramp is the same as before. Note at higher frequencies, i.e., at passes $n \geq 25{,}000$, the amplitude of the optical wavelength modulation decreases significantly more than for $Q = 30$ in Figure 5-6. The amplitude and phase response of the transfer function for this system is shown in Figure 5-11.

The amplitude response shown at the top has the same shape as the discrete transfer function for $Q = 100$ shown in Figure 5-4. The roll-off point occurs near the

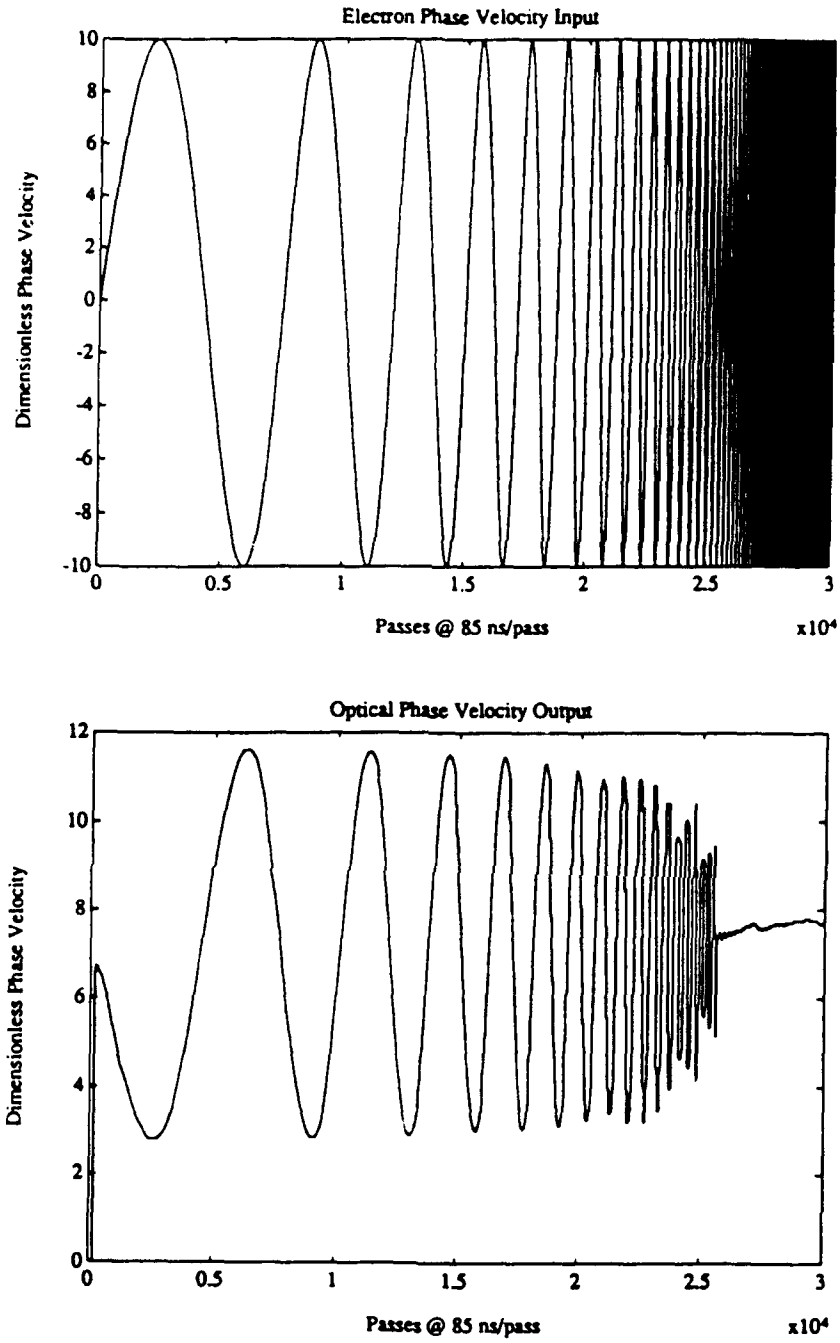

Figure 5-10. Resonant optical wavelength phase velocity and resonant electron energy phase velocity for frequency modulated input electron energy in a short pulse FEL with $Q = 100$.

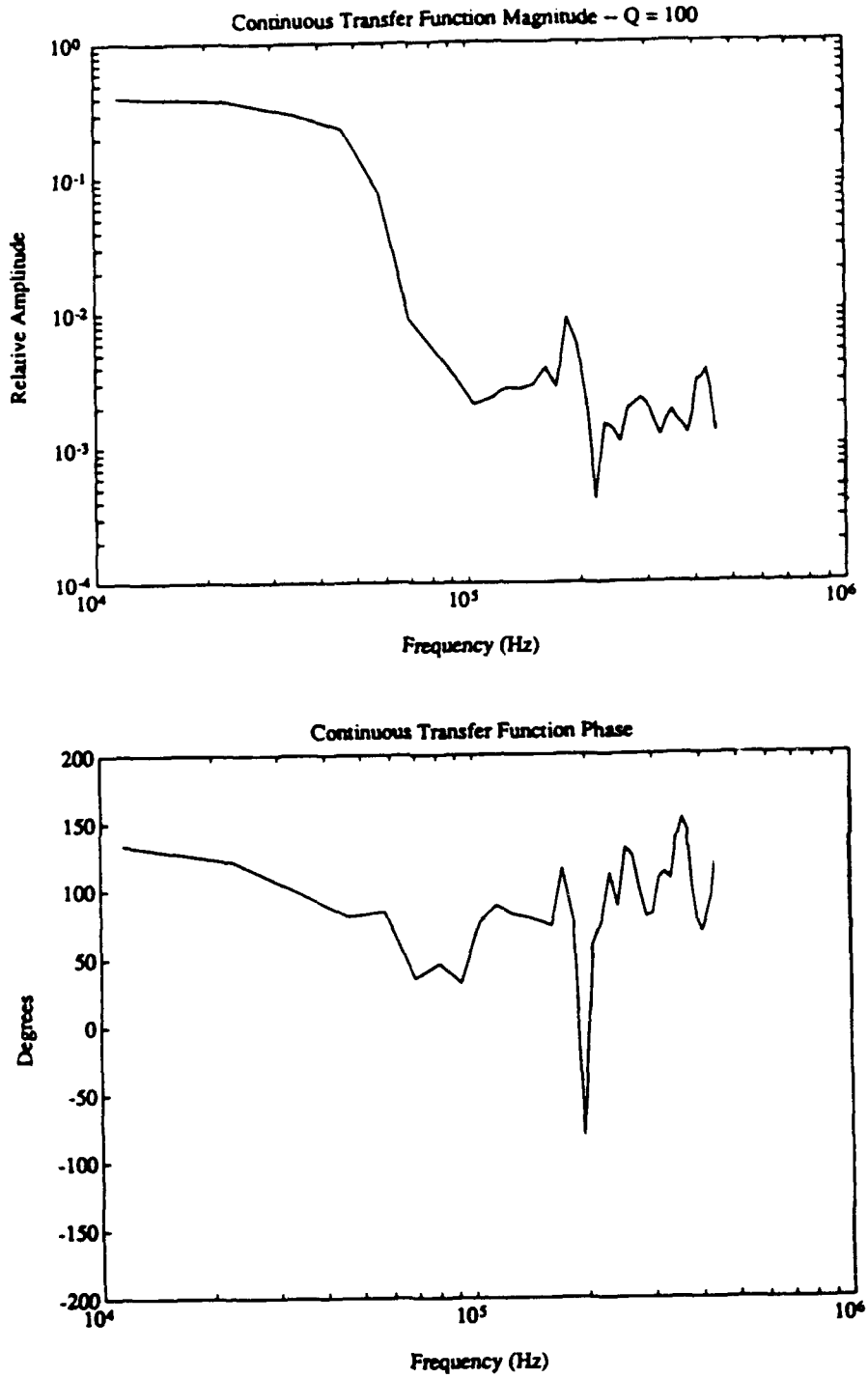

Figure 5-11. Amplitude and phase response of the continuous transfer function $H(f)$ for a low gain FEL with Q = 100.

same frequency at $f \approx 20$ kHz. Above $f \approx 10^5$ Hz the curve fluctuates randomly, but appears to level off near the relative amplitude 10^{-3}. The phase response of $H(f)$ is plotted at the bottom. The first increase in phase occurs near $f = 3 \times 10^4$ which also corresponds to the point of maximum roll-off in relative amplitude above. The complete phase-shift occurs at $f = 3 \times 10^5$, much sooner than that for $Q = 30$ in Figure 5-4.

F. DISCRETE VS. CONTINUOUS TRANSFER FUNCTION COMPARISON

Understanding the response of the FEL to a rapidly varying resonant wavelength is important in the design of a linear feedback system. The most stable optical output is achieved only when the feedback system is optimized to perform at same amplitude and phase as the FEL transfer function $H(f)$. Applying a numerical simulation as discussed in the previous section helps to increase knowledge of the FEL parameters that affect the transfer function response.

The discrete and continuous amplitude responses of the FEL transfer functions are compared directly in Figure 5-12. Recall that the discrete and continuous curves are obtained in two completely distinct ways. The first method plots each response point at a single frequency with a simulation that is run only at that frequency for a long period of time. It takes many simulations to obtain such a curve. The second method uses FFT analysis to obtain a transfer function from a single output wavelength signal and a single input electron energy frequency modulated signal. The preferred method is that used to obtain the continuous curves because it is less time consuming and uses only a single short-pulse evolution simulation. That the continuous and discrete curves compare so favorably in both cases attest to the accuracy of the continuous method for frequencies near the amplitude cut-off. Because the continuous method enables any FEL input parameter to be varied in a

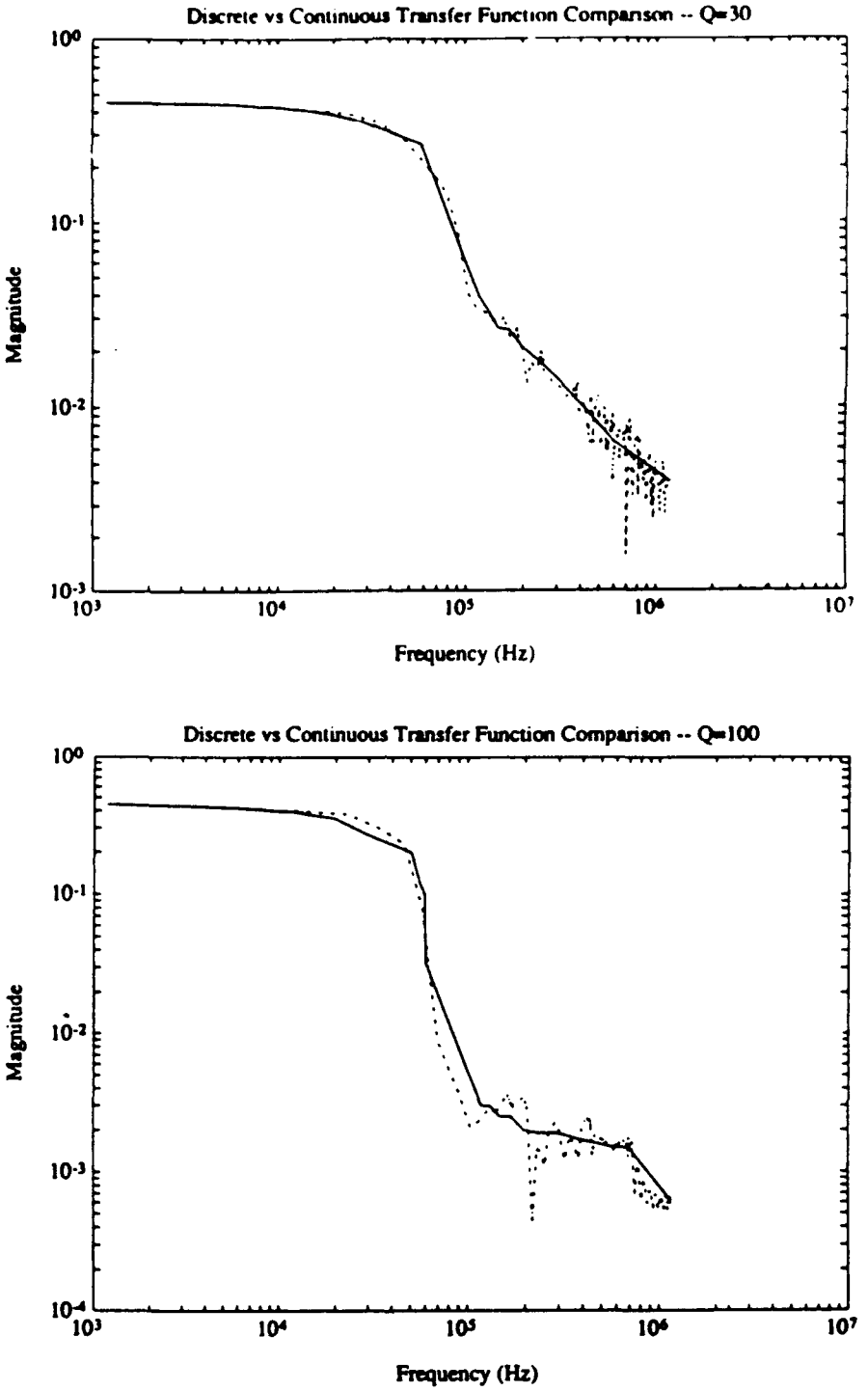

Figure 5-12. Comparison of the discrete and continuous amplitude response of the transfer function for a low gain FEL with Q = 30 and with Q = 100.

single short-pulse evolution simulation, the corresponding effect on the dynamic response of the FEL transfer function can be explored with relative ease.

VI. CONCLUSIONS

The current world political climate is extremely volatile, and the threat of wide proliferation of advanced weapons is high. With the technology of anti-ship missiles increasing every year, a time may come when the ordinary methods of ship defense will be obsolete. Directed energy may be the only means available with the capability to destroy anti-ship missiles on their path to the target. Two high energy laser systems seem feasible for shipboard use. Both are compatible in the design of a self-defense weapon system if modularity is considered. The FEL appears to have the best advantages for use at sea in the long run, but the technology needed to support its use is not complete. Meanwhile, a more mature chemical laser system, using deuterium fluoride as a fuel, has been designed by TRW. The power requirements, weight, and size of the system readily allow emplacement on existing ships, making it a logical choice for testing directed energy effectiveness at sea.

Design flexibility and continuous tunability are two of the principle advantages of the FEL over the conventional laser. The promise of high efficiency and high average power has made the FEL the subject of extensive research. Most of the present research is focused toward utilization of the FEL as a reliable source of stable, coherent light for user facilities. The Stanford University Superconducting Accelerator (SCA) Free Electron Laser (FEL) Facility, provides light for physics and medical research. The optical wavelength is observed to fluctuate randomly by a fraction of a percent over times less than a millisecond. Experiments conducted at the facility require at least ten times more stability.

In an FEL, the optical wavelength is proportional to the input electron energy through the resonance condition, $\lambda = \lambda_o / 2\gamma^2$, where γ is the Lorentz factor, m is the

electron mass, and c is the speed of light in vacuum. Researchers at the Stanford SCA/FEL have successfully accomplished optical wavelength stabilization by measuring wavelength drift and adjusting the input electron beam energy through negative feedback [4]. The effect is simulated by modifying a short pulse FEL numerical program to allow the resonant wavelength to vary over many passes.

Through simulation of various modulation parameters, the effects on the optical pulse, optical power, and the output wavelength are observed. Modulation at high frequencies and low amplitudes has little effect on the wavelength, but the optical power is observed to oscillate with significant magnitude. The trapped particle instability is also suppressed. As the period of oscillation increases, the optical wavelength begins to follow and the relative magnitude of optical power variation is reduced. However, the trapped particle sidebands are also able to follow the resonant wavelength modulation, and the accompanying side effects return. At high modulation amplitudes, the electrons and the optical wave cycle rapidly in and out of resonance, so that periodic optical power "giant pulses" occur.

Net gain and resonator loss both have significant effects on the behavior of the resonant wavelength during electron beam energy modulation. Higher gain and lower loss aid the resonant wavelength motion, but the high optical power that results tends to narrow the optical spectrum through mode competition. As the optical spectrum narrows, it resists wavelength changes because less optical power is available in neighboring modes.

Desynchronism also affects the ability of the FEL to follow resonant electron energy modulation. The maximum steady-state power and the maximum weak-field gain occur at different values of desynchronism. When the steady-state power is at a peak, gain is low, and the optical spectrum is more susceptible to narrowing through mode competition. Here, the FEL is more likely to resist resonant wavelength

modulation. When the gain is at a peak, steady-state power is relatively low, and the FEL is more likely to accept resonant wavelength shifts. For other values of desynchronism, the combination of both effects determines the amount of optical power available at the resonant wavelength during modulation.

The short pulse FEL is observed to preferentially follow shifts from longer to shorter wavelengths. During this type of shift, the dimensionless phase velocity of the electron beam increases. At the same time, the resonant wavelength moves toward values of decreasing phase velocity. But on an increase in optical power, the optical field strength increases, causing the gain spectrum to broaden in phase velocity. These effects combine to produce a favorable condition under which resonance is maintained for a longer period of time than would normally occur at steady-state. The FEL is thus able to follow the resonant wavelength in this direction with greater optical power.

As the frequency of electron energy modulation increases, the peak-to-peak amplitude of the resonant wavelength modulation decreases. The nature of this decrease is important to the design of a wavelength stabilization system. The ability of the optical pulse to follow resonance at higher frequencies allows the use of faster feedback to the electron beam source. Knowing the exact cut-off enables optimization of the feedback system. Simulations modified to allow a ramp of frequencies produce plots showing the amplitude and phase response of the FEL to a rapidly shifting resonant wavelength. The result is called the continuous FEL transfer function. A separate method is used to obtain a curve describing the discrete amplitude response for a short pulse FEL with two different values of the quality factor Q. Curves of the continuous and discrete transfer function compare favorably in both cases tested. The continuous method can now be used to effectively simulate the short pulse transfer function behavior for a variety of FEL input parameters.

LIST OF REFERENCES

[1] J.M.J. Madey, "Stimulated Emission of Radiation in Periodically Deflected Electron Beams," *Journal of Applied Physics*, v. 42, 1971.

[2] W.B. Colson, C. Pellegrini, A. Renieri and J.M.J Madey, "Introduction to Free Electron Lasers," Chapter 1 in *Free Electron Laser Handbook*, W.B. Colson, C. Pellegrini and A. Renieri (eds.), North-Holland Physics, Elsevier Science Publishing Co. Inc., The Netherlands, 1990.

[3] W.B. Colson, "Classical Free Electron Laser Theory", Chapter 5 in *Free Electron Laser Handbook*, W.B. Colson, C. Pellegrini and A. Renieri (eds.), North-Holland Physics, Elsevier Science Publishing Co. Inc., The Netherlands, 1990.

[4] A. Marziali and T.I. Smith, "Feedback Stabilization of the SCA/FEL Wavelength," *Nuclear Instruments and Methods in Physics Research*, North-Holland, XXX, xxx, 1993.

[5] Janne E. Nolan and Albert D. Wheelon, "Third World Ballistic Missiles", *Scientific American*, v.263, No.2, August 1990.

[6] Center for Naval Analysis, CNA Research Memorandum 91-81, *Assessment of a Modular High Energy Laser System* (U), by F.M. Bomse, SECRET, August 1990.

[7] Carl A. Bice, *Theory for the CEBAF and Shipboard FELs*, Master's Thesis, Naval Postgraduate School, Monterey, California, December 1991.

[8] N. Friedman, *The Naval Institute Guide to World Naval Weapon Systems*, Naval Institute Press, Annapolis, Maryland, pp.81-82, 1989.

[9] R.S. Bradford, TRW-Applied Technology Division, "High Energy Laser Weapon System (HELWEPS) for Anti-ship Missile Defense", Briefing presented to Naval Postgraduate School, August 1992.

[10] Marvin B. Schaffer and others, "A Tactical Directed Energy Weapon Research Strategy (U)", RAND Corporation, Santa Monica, CA, SECRET, August 1990.

[11] Naval Sea Systems Command (511), "Modularity for Surface Combatants", Briefing for Capt. Utegaard and Cdr. Abbott, 24 April 1991.

[12] Center for Naval Analysis, *Ship Installation of Laser Weapon System: Feasibility and Cost* (U), by Charles Chambers and others, SECRET, August 1990.

[13] Jon Grossman, "Military Laser Systems", **P-7704**, RAND Corporation, Santa Monica, CA, January 1991.

[14] "The Airborne Laser Laboratory (ALL) Completes Successful Tests", *International Defense Review*, v.116, p. 1702, December 1983.

[15] N. Bloembergen, and others, "Report to the American Physical Society of the Study Group on Science and Technology of Directed Energy Weapons", *Reviews of Modern Physics*, v.59, No.3, Part II, July 1987.

[16] E.T. Scharlemann, W.M. Fawley, B.R. Anderson, and T.J. Orzechowski, *Nuclear Instruments and Methods in Physics Research*, North-Holland, **A250**, p. 150, 1986.

[17] Kwang-Je Kim and Andrew Sessler, "Free Electron Lasers: Present Status and Future Prospects", *Science*, v.250, 5 October 1990.

[18] Henry P. Freund and Robert K. Parker, "Free Electron Lasers", *Scientific American*, pp. 84-89, April 1989.

[19] W.B. Colson and A.M. Sessler, "Free Electron Lasers", *Annual Reviews of Nuclear and Particle Science*, v.35, pp. 25-54, 1985.

[20] W.B. Colson, "Free Electron Laser Theory", Ph.D. Dissertation, Stanford University, September 1977.

[21] W.B. Colson and D. Prosnitz, "Free Electron Lasers", Chapter 4.1 in *Handbook of Laser Science and Technology, Supplement 1: Lasers*, CRC Press, Inc., 1991.

[22] S.V. Benson, "A Compact Free-Electron Laser Design for Extremely Broadband Harmonic Operation in the Infrared", *Nuclear Instruments and Methods in Physics Research*, North-Holland, **A318**, pp. 221-224, 1992.

[23] W.B. Colson, "Fundamental Free Electron Laser Theory and New Principles for Advanced Devices", *Free Electron Lasers: Critical Review of Technology*, B.E. Newman (ed), Proceedings of SPIE, **738**, pp. 2-27, 1988.

[24] W.B. Colson, "Tutorial on Classical Free Electron Laser Theory", *Nuclear Instruments and Methods in Physics Research*, North-Holland, **A237**, pp. 1-9, 1985.

[25] J.D. Jackson, *Classical Electrodynamics*, 2nd edition, John Wiley and Sons, Inc., 1975.

[26] W.B. Colson and J. Blau, "Parameterizing Physical Effects in Free Electron Lasers", *Nuclear Instruments and Methods in Physics Research*, North-Holland, **A272**, pp. 386-391, 1988.

[27] W.B. Colson, "Free Electron Laser Wave and Particle Dynamics", Invited Chapter at the International Summer School of Quantum Electronics, Erice (Sicily), S. Martellucci and A.N. Chester (eds), Plenum Press, pp. 189-209, 1983.

[28] W.B. Colson and R.A. Freedman, "Oscillator Evolution in Free Electron Laser Oscillators", *Physical Review Letters*, **A27**, No. 3, pp. 1399-1413, March 1983.

[29] W.B Colson, J.C. Gallardo, and P.M. Bosco, "Free-Electron-Laser Gain Degradation and Electron-Beam Quality", *Physical Review Letters*, **A34**, No. 6, pp. 4875-4881, December 1986.

[30] W.B. Colson and J. Blau, "Free Electron Laser Theory in Weak Optical Fields", *Nuclear Instruments and Methods in Physics Research*, North-Holland, **A259**, pp. 198-202, 1987.

[31] W.B. Colson, "The Trapped Particle Instability in Free Electron Laser Oscillators and Amplifiers", *Nuclear Instruments and Methods in Physics Research*, North-Holland, **A250**, pp. 168-175, 1986.

[32] Anthony E. Siegman, *Lasers*, pp. 1004-1040, University Science Books, 1986.

[33] T.I. Smith and H.A. Schwettman, "Facilities for Using the FEL as a Research Tool", *Nuclear Instruments and Methods in Physics Research*, North-Holland, **A304**, pp. 812-821, 1991.

[34] G.A. Cord, W.B. Colson, and J. Frisch, "Comparing Simulations and Experimental Observations of the Trapped-Particle Instability in the Stanford FEL", *Nuclear Instruments and Methods in Physics Research*, North-Holland, **A304**, pp. 601-606, 1991.

[35] A. Marziali and T.I. Smith, "Demonstration of Wavelength Stabilization in a Free Electron Laser", W.W. Hansen Experimental Physics Laboratory, Stanford University, Stanford, California, 1993.

[36] P.M. Embree and B. Kimble, *C Language Algorithms for Signal Processing*, Prentice Hall, Inc., Englewood Cliffs, New Jersey, 1991.

[37] A.V. Oppenheim and R.W. Schafer, *Digital Signal Processing*, Prentice-Hall, pp. 556, 1975.

[38] J.N. Little and L. Shure, *Signal Processing Toolbox for Use with MATLAB®*, The MathWorks, Inc., South Natick, Massachusetts, pp. 92-99, 1988.

INITIAL DISTRIBUTION LIST

1.	Defense Technical Information Center Cameron Station Alexandria, Virginia 22304-6145	2
2.	Library, Code 52 Naval Postgraduate School Monterey, California 93943-5002	2
3.	Professor William B. Colson, Code PH/Cw Department of Physics Naval Postgraduate School Monterey, California 93943-5000	8
4.	Professor Robert L. Armstead, Code PH/Ar Department of Physics Naval Postgraduate School Monterey, California 93943-5000	1
5.	Professor K. E. Woehler, Code PH/Wh Chairman, Department of Physics Naval Postgraduate School Monterey, California 93943-5000	1
5.	Professor Todd I. Smith W.W. Hansen Experimental Physics Laboratory Stanford University Stanford, California 94305-4085	1